# Advanced MEMS Microprobes for Neural Stimulation and Recording

by

Arash Akhavan Fomani

A thesis
presented to the University of Waterloo
in fulfillment of the
thesis requirement for the degree of
Doctor of Philosophy
in
Electrical and Computer Engineering

Waterloo, Ontario, Canada, 2011

## Author's Declaration

I hereby declare that I am the sole author of this thesis. This is a true copy of the thesis, including any required final revisions, as accepted by my examiners.

I understand that my thesis may be made electronically available to the public.

**Abstract**

The in-vivo observation of the neural activities generated by a large number of closely located neurons is believed to be crucial for understanding the nervous system. Moreover, the functional electrical stimulation of the central nervous system is an effective method to restore physiological functions such as limb control, sound sensation, and light perception. The Deep Brain Stimulation (DBS) is being successfully used in the treatment of tremor and rigidity associated with advanced Parkinson's disease. Cochlear implants have also been employed as an effective treatment for sensorineural deafness by means of delivering the electrical stimulation directly to the auditory nerve. The most significant contribution of this PhD study is the development of next-generation microprobes for the simultaneous stimulation and recording of the cortex and deep brain structures.

For intracortical applications, millimetre length multisite microprobes that are rigid enough to penetrate into the cortex while integrated with flexible interconnection cables are demanded. In chronic applications, the flexibility of the cable minimizes the tissue damage caused by the relative micro-motion between the brain and the microprobe. Although hybrid approaches have been reported to construct such neural microprobes, these devices are brittle and may impose severe complications if they break inside the tissue. In this project, MEMS fabrication processes were employed to produce non-breakable intracortical microprobes with an improved structural design. These 32 channel devices are integrated with flexible interconnection cables and provide enough mechanical strength for penetration into the tissue. Polyimide-based flexible implants were successfully fabricated and locally reinforced at the tip with embedded 15 $\mu$m-thick gold micro-needles.

In DBS applications, centimetre long microprobes capable of stimulating and recording the neural activity are required. The currently available DBS probes, manufactured by Medtronic, provide only four cylindrical shaped electrode sites, each 1.5 mm in height and 1.27 mm in diameter. Although suitable for the stimulation of a large brain volume, to

measure the activity of a single neuron but to avoid measuring the average response of adjacent cells, recording sites with dimensions in the range of 10 – 20 $\mu$m are required. In this work, novel Three Dimensional (3D) multi channel microprobes were fabricated offering 32 independent stimulation and recording electrodes around the shaft of the implant. These microprobes can control the spatial distribution of the charge injected into the tissue to enhance the efficacy and minimize the adverse effects of the DBS treatment. Furthermore, the device volume has been reduced to one third the volume of a conventional Medtronic DBS lead to significantly decrease the tissue damage induced by implantation of the microprobe.

For both DBS and intracortical microprobes, the impedance characteristics of the electrodes were studied in acidic and saline solutions. To reduce the channel impedance and enhance the signal to noise ratio, iridium (Ir) was electroplated on gold electrode sites. Stable electrical characteristics were demonstrated for the Ir and gold electrodes over the course of a prolonged pulse stress test for 100 million cycles. The functionality and application potential of the fabricated microprobes were confirmed by the in-vitro measurements of the neural activity in the mouse hippocampus.

In order to reduce the number of channels and simplify the signal processing circuitry, multiport electrostatic-actuated switch matrices were successfully developed, fabricated, and characterized for possible integration with neural microprobes to construct a site selection matrix. Magnetic-actuated switches have been also investigated to improve the operation reliability of the MEMS switching devices.

**Acknowledgements**

First and foremost I would like to express my sincere gratitude to Professor Raafat R. Mansour. It is my honour to be his student and I greatly appreciate his constant guidance and support throughout my PhD studies. His patience and enthusiasm have always motivated me to work hard and seek perfection in my doctoral research.

I would like to thank Natural Sciences and Engineering Research Council of Canada (NSERC), Ontario Centres of Excellence (OCE), and Waterloo Institute for Nanotechnology (WIN). This work would not have been possible without their financial supports. I also appreciate our productive collaborations with Dr. Souhile Assaf (Medtrode, Inc.), Professor Mandar Jog (London Health Sciences Centre), and Professor Peter L. Carlen (Toronto Western Research Institute, University of Toronto).

I am grateful to Professor Ash Parameswaran from Simon Fraser University who served as the external examiner of this thesis and provided constructive feedback. I am also grateful to the members of my PhD examination committee, Professor Eihab Abdel-Rahman, Professor Magdi Salama, and Professor Dayan Ban for their time and effort to improve the quality of this thesis.

I am thankful to all members of the Centre for Integrated RF Engineering (CIRFE) research group not only for their invaluable technical assistance but also for creating a warm, friendly, and welcoming environment. In particular, Mr. Bill Jolley, Mr. Roger Grant, and Dr. Siamak Fouladi have significantly contributed to the outcome of this research through many stimulating discussions.

I am indebted to many wonderful friends who have supported me even in the cold rainy days of my PhD studies. They have been always there to lend me a helping hand and made my time at Waterloo an enjoyable experience full of unforgettable memories.

I have the utmost gratitude to my parents who unconditionally love me and patiently

guide me. They constantly supported me and I cannot be thankful enough for their sacrifices. I would also like to express my appreciation to my dear parents-in-law for all their encouragements and supports. I am thankful to my caring brother Armin for always coming to my aid at the time of need.

Finally, I am forever grateful to my dearest friend and the love of my life, Maryam, who stood behind me throughout this journey. She has always inspired me, believed in me, and pushed me forward whenever I was unable to move.

# Table of Contents

# List of Tables

# List of Figures

# Chapter 1

# Introduction

Neural prostheses or neuroprosthetics provide irreplaceable therapies for many medical conditions that other methods such as surgery or chemical therapy have failed to treat. A comprehensive understanding of the Central Nervous System (CNS) is essential to successfully develop these systems and enhance their functionality. In initial studies, the activities of a single neuron were recorded to investigate the mechanisms of signal transmission in nerve cells [1, 2]. Although these early studies made significant contributions to the understanding of the central nervous system, they were unable to decipher the complex interactions between the vastly interconnected networks of neurons. The recording of multiple neurons activities attracted the attention of researchers in the early 1970s due to the observation of inhibitory and excitatory actions of one neuron on another cell [3]. In some cases the firing of one neuron silenced or initiated the firing of another neuron. Furthermore, it was demonstrated that by monitoring the activities of a small set of neurons in the motor cortex of a unanesthetized monkey, it is possible to predict the arm movements of the animal in real time [4–6].

Presently, the electrical stimulation of the CNS is employed for the treatment of abnormalities or even restoration of various types of sensory, motor, and cognitive functions [7]. Cochlear implants have been employed as an effective treatment for sensorineural deafness

by means of delivering the electrical stimulation directly to the auditory nerves [8]. Also, electrical stimulations of the retina [9] or the visual cortex [10] are intensively investigated and possible applications are considered to assist the blind. Furthermore, the stimulation of deep brain structures such as the Sub-Thalamic Nucleus (STN) and the internal segment of the Globus Pallidus (GPi) are effective treatments to alleviate tremor, rigidity, and dyskinesias associated with advanced Parkinson's disease [11]. Other possible applications of Deep Brain Stimulation (DBS) include the treatment of primary dystonia [12], hyperkinetic disorders [13], obsessive compulsive disorder [14], and treatment-resistant clinical depression [15].Many other attempts to construct brain-computer interfaces have been reported in literature [16–19].

The efficacy of neural stimulation therapies inevitably depends on the design and functionality of the implanted microelectrodes. In general, neuroprosthetics systems demand implantable microelectrode arrays capable of stimulating a large number of closely located neurons and at the same time monitoring their activities. The dimensions of these microprobes must be as small as possible to induce minimal tissue damage, while the implant must possess sufficient mechanical strength to withstand the manipulation forces applied during the implantation process. Three Dimensional (3D) devices are needed to adjust the profile of the charge injected into the tissue and record the response of the neurons in the target tissue volume. The long-term biocompatibility of the probes is also important particularly for chronic applications such as DBS. Despite the great advances, many of these requirements are not satisfied, thus further research is needed to enhance the current state-of-the-art.

This research focuses on the design, fabrication, and characterization of neural microprobes for intracortical and DBS applications. New generations of multichannel devices with advanced functionalities are constructed employing novel fabrication processes. The electrical characteristics of the neural implants are presented in detail and the character-

istics stability of the devices is discussed. Furthermore, the application potential of the fabricated microprobes for simultaneous neural stimulation and recording are demonstrated in saline solutions and in-vitro experiments.

## 1.1 Neural Microprobes

A Variety of electrodes is employed in the neurophysiological research for stimulating and recording the neural activities. Based on the application and location of the target, the arrays of electrodes are fabricated on flat substrates or needle-shape structures. The planar devices include retina implants [20, 21] and the microprobes for epicranial, epidural, and epipial recordings [22]. For intracortical and DBS applications, the electrode sites must be located on penetrating shanks with lengths ranging from a fraction of a millimetre to a few centimetres.

The earliest and simplest type of electrodes are encapsulated metallic microwires [23–25] or glass micropipettes filled with an electrolyte solution [26]. These microelectrodes are 25 to 100 $\mu$m in diameter at the base and sharpened to a few micrometres at the tip by an electrolytical etching process [7, 27]. Although Pt/Ir wires exhibit the best performance in terms of their capability for charge delivery, other materials such as stainless steel and tungsten have also been utilized [27, 28]. Typically, the microwires are coated with parylene-C, epoxy, or glass except at the sites where the electrodes are exposed to the tissue [23, 27–29].

The glass or microwire electrodes are extensively used in neural studies due to the simplicity of their construction method. However, the fabrication of these devices with uniform geometries and identical characteristics is difficult [30]. More importantly, these electrodes are not suitable for recording and stimulating a large number of neurons, located in a small volume of the tissue [31]. To realize multichannel devices based on microwire

electrodes, several insulated microwires are manually bundled together [27,32]. Therefore, the volume of the probe and consequently the induced tissue damage imposed by the device implantation are linearly increased with electrode count. Furthermore, the position of the microwires inside the bundle cannot be precisely controlled, the process is extremely time-consuming, and the associated yield is low.

The photolithography, micromachining, and thin-film processing techniques were later employed to advance the state-of-the-art in the fabrication of neural microprobes [30, 33–44]. These electrodes can be constructed with multiple recording channels without a significant increase in the overall size of the structure. Reproducible production, integration of electronic circuitry, precise control over the spatial distribution of the electrode sites, and a high density of electrodes are some advantages of these probes compared to conventional microwire electrodes. Despite these superior properties, the electrical characteristics of the channels are not stable in long-term experiments and the number of operational recording sites is reduced over time [43]. In addition, most of the presented approaches are only capable of producing intracortical microprobes with millimetre-range lengths. Indeed, based on the thin film processing methods, the fabrication of the DBS microprobes with a sufficient mechanical stiffness for targeting a few centimetres deep beneath the skull is extremely challenging [33].

The next section outlines the motivation and overall objectives of this doctoral study. A comprehensive review of the microprobe fabrication methods for both the DBS and intracortical microprobes will be provided in chapter 2.

## 1.2 Motivations and Objectives

The in-vivo observation of the neural activities from a large number of closely located neurons is believed to be crucial for understanding the central nervous system. The neu-

roprosthetics also require high-density multisite microprobes to enhance the efficacy of neurostimulation therapies and reduce the associated side effects. Following the earlier discussions, it is clearly evident that microwire bundles introduce extensive damage to the neural tissue while the 3D distribution of electrode sites and the number of channels is severely limited. This project aims to utilize Micro-Electro-Mechanical System (MEMS) fabrication technologies to produce a new generation of intracortical and DBS microprobes. However, there are several issues that need to be resolved before the widespread application of these microprobes in neurological research and treatment.

For intracortical applications, the microprobes must be as thin as possible to appear invisible to the tissue while possessing enough mechanical strength for penetration. Multichannel high-density microprobes have been reported over the past three decades offering advanced capabilities such as integrated electronics and embedded micro-fluidic channels [37, 39, 45, 46]. In most devices, substrates such as silicon, metals, sapphire, and glass have been utilized to provide the microprobe with sufficient rigidity for implantation. These rigid devices are not suitable for chronic studies since the neural tissue is damaged over time as a result of the relative micro-motion between the brain and the microprobe [47]. To alleviate this issue and improve the biocompatibility of the implants, multisite microprobes made of flexible polymers have been proposed [34,35]. The polymer-based microprobes are integrated with an extremely flexible interconnection cable which facilitates the connection of the implant to the external circuitry. Although such devices are favoured for long-term applications, the flexible microprobes cannot penetrate the tissue and must be implanted by a microsurgical tool.

Despite the great advances, only a few hybrid integration approaches has been reported to construct rigid microprobes connected to flexible interconnection cables [48, 49]. These microprobes are brittle and may impose severe complications if the device breaks inside the tissue during the implantation. Non-breakable multisite microprobes with a modified

structural design are presented offering sufficient mechanical strength for penetration into the tissue. The flexibility of the cable allows the microprobe to move with the surrounding tissue consequently reducing the post implantation damage. Metallic micro-needles are embedded at the tip of the polyimide-based implants to reinforce the microprobes locally at the tip while the device is integrated with a flexible cable. Surface micro-machining techniques with only 3 lithography steps are employed to fabricate these devices. The details of the fabrication process as well as the characteristics of the microprobes are discussed in chapter 3.

For DBS applications, to enhance the benefits of the therapy, multisite microprobes must be capable of both stimulation and recording. The currently available DBS probes, manufactured by Medtronic [50], provide only four cylindrical shaped electrode sites, each 1.5 mm in height and 1.27 mm in diameter. The dimensions of Medtronic electrodes are suitable for the stimulation of a large volume of the brain and not preferred for the recording or stimulation of individual neurons. If the area of the electrode is large, the average response of many neurons is collectively recorded. Therefore, to measure the activity of a single neuron, recording sites with dimensions in the range of 10-20 $\mu$m are favoured [7]. Although the advanced thin film microprobes present electrodes with miniature dimensions, these devices are only suited for intracortical applications where the length of the microprobes is limited to a few millimetres.

In DBS, the target region is typically located a few centimetres deep inside the brain. This dimensional constraint severely complicates the fabrication of the DBS microprobes. Indeed, only a few processes have been reported capable of producing sufficiently long microprobes for DBS applications [23, 27, 33, 51, 52]. The encapsulated metal wires introduced for the single site recording are the simplest and earliest type of devices that can be constructed with lengths in excess of several centimetres [23]. One possible method of fabricating the DBS microprobes with multisite recording / stimulation capabilities is to

bundle several micro-wires into one ensemble [27, 51, 52]. Although this is practical, the volume of the implants and the tissue damage induced by the insertion of the microprobe linearly increases with the channel count. Furthermore, the rigidity of the device, the electrode sites dimensions, and the position of microwires inside the bundle cannot be easily controlled. To resolve such adversities, a method based on micro-fabrication techniques has been proposed in [33] to construct miniature multisite DBS microprobes. Thick electroplated micro-needles are utilized as the structural layer supporting the thin-film electrode traces. Even though a significant enhancement in the number and density of electrode sites are achieved, the fabricated microprobes are not integrated with flexible interconnection cables and the electrode sites can only be placed on a planar surface.

To enhance the efficacy and minimize the adverse effects of the DBS treatment, it is crucial to control the spatial distribution of the charge injected into the tissue. For this purpose, 3D microprobes with many independent electrode sites around the probe shaft are demanded. To produce such devices using conventional fabrication methods, the deposition, lithography, and etching must be performed over the 3D surface of a support structure. Although lithography and laser micromachining over non-planar surfaces have been demonstrated, the resolution and associated yields of such processes are limited. In most cases the structure must be rotated around its axis or the deposition / lithography equipment must rotate around the probe. Considering the small dimensions of the device, such approaches appear to be extremely difficult if not impossible.

In this thesis, novel 3D microprobes are presented offering both stimulation and recording capabilities. Independent stimulation sites are placed around the probe shaft providing the implant with an enhanced capability to control the profile of the injected charge into the tissue. In this method, thin-film planar devices are assembled on a flexible support structure to construct the implants. Surface micromachining technologies are used to fabricate the thin film planar devices. Consequently, the dimensions and spatial distribution of

the electrode sites are precisely controlled by the sub-micrometre resolution of the lithography process. The microprobes also provide flexible interconnection cable to facilitate their connection to external circuitry. The fabrication process and characteristics of the implants are described in chapter 4.

Integration of a site selection matrix with the signal processing circuitry of a neuroprosthetic system or non-implanting section of the neural microprobe is a possible solution to reduce the complexity and power consumption of the system. A switch matrix can be used to connect several electrode sites of the implanted neural microprobe to a single stimulation or recording channel of the micro-controller. Therefore, a micro-controller with a few number of channels can be effectively used for multichannel stimulation and recording. Micro-Electro-Mechanical Systems (MEMS) technology is considered for the fabrication of the switching matrices on the same substrate of the microprobes where the bonding pads are located. MEMS switches provide a low On-state resistance, high Off-state isolation, and acceptable switching speeds (2 - 40 $\mu$s) while consuming negligible powers for operation [53]. Chapter 5 presents the fabrication processes and characteristics of multiport electrostatic-actuated switch matrices and magnetic-actuated switches. The proposed methods are compatible with the fabrication of flexible neural microprobes and can be employed for system integration.

The major objectives of this PhD study are summarized as follows:

- The development of intracortical microprobes offering flexible interconnection cables and adequate mechanical strength for implantation.
- The development of 3D multisite microelectrodes for stimulation and recording with the capability to adjust the profile of the injected charge into the tissue.
- The development of MEMS switching elements and switch matrices for possible integration in neuroprosthetics systems.

## 1.3 Thesis Outline

The development and optimization of the MEMS fabrication methods to produce multisite neural microprobes for chronic applications is the main focus of this doctoral research. In chapter 1, a brief introduction of neural microprobes is presented to illustrate the demand for further research on the subject and to motivate the readers. Some of drawbacks of the existing microprobe technologies are also pointed out.

Chapter 2 provides a review of neural microprobes presented in literature for intracortical and DBS implants. In particular, the thin film microprobes fabricated by photolithography, micromachining, and thin film processing techniques are comprehensively discussed. The selection criteria and materials of choice as the structural layer, insulator, electrodes, and electrode sites are addressed. In addition, the fabrication processes, benefits, and limitations of several types of microprobes are summarized.

Chapter 3 describes the structures, fabrication, and characteristics of proposed intracortical microprobes with an improved structural design. These devices are integrated with long flexible interconnection cables while providing enough mechanical strength for penetration. The in-vitro characteristics and impedance stability of the electrodes are also studied.

A novel generation of 3D microprobes for DBS applications is reported in chapter 4. Thin film microprobes are fabricated and assembled on flexible support structures to construct the proposed implants with independent stimulation and recording sites around the shaft. Chapter 4 elaborates on the fabrication issues and challenges, performance, and characteristics stability of the microprobes. The possibility of simultaneous stimulation and recording is demonstrated by in-vitro experiments in mouse hippocampus.

The MEMS switches and switching matrices for the possible integration with microprobes are then presented in chapter 5. The fabrication, configuration, and characteristics

of metallic and dielectric cantilever switches, actuated by electrostatic and electromagnetic forces are reported. Despite the reliability concerns, the excellent characteristics offered by fabricated MEMS switch matrices are a strong motivation for the integration of these circuitries. Finally, chapter 6 concludes the contributions of the doctoral research in the development of the neural microprobes and addresses future works.

# Chapter 2

# Literature Survey
# Intracortical and DBS Microprobes

Neuroprosthetics employ implantable arrays of electrodes (neural microprobes) to deliver the electrical stimulation pulses and/or to monitor the neural activities. The intracortical microprobes target the surface of the brain and interface with various regions of the cortex such as the sensory or motor areas. The stimulation and recording of deep brain structures such as the thalamus and hippocampus is performed through the so-called DBS microprobes with lengths in the range of several centimetres. For years, the only available devices for neurological research were metal microwires or glass electrodes. Comprehensive reviews of these early devices have been provided in [25] and [26]. Despite their popularity for single neuron or field potential studies, the extensive tissue damage induced by microwire bundles prevents the further application of these implants in advanced neurological research and treatments.

The silicon technology and lithography technique were suggested by M. P. Lepselter in 1966 for the fabrication of a new generation of implants known as thin film microprobes [54]. The immediate benefit of such an approach is the production of multisite microprobes that were capable of recording and stimulating closely located neurons with sizes comparable to those of a single metal electrode. Therefore, the tissue damage introduced by the

implantation of these microprobes can be significantly less than the injury imposed by a bundle or array of metal electrodes.

The first reports on the fabrication of the thin film microprobes were published in the 1970s by K. D. Wise and his coworkers [55, 56]. At the time, the silicon etching processes were not mature and these early probes did not have uniform electrical and mechanical characteristics. Later advances in the microelectronic, sensor, and Micro-Electro-Mechanical Systems (MEMS) technologies have improved the reliability, reproducibility, and production yield of the microprobes.

Thin film probes consist of three main sections; namely, the support structure, the stimulating or recording sites (electrode sites), and the encapsulated interconnection lines. The support structure serves as the main body and determines the overall shape of the microprobe. The substrates employed for the fabrication of this section must be biocompatible and provide adequate mechanical strength for the penetration into the tissue. Apart from silicon [36–40], the microprobes have been fabricated on a variety of substrates such as metals [30, 33, 41–43], sapphire [57], glass [31], SU-8 [58], diamond [59], and polymers [34, 35].

Iridium (Ir) [37], iridium oxide ($IrO_x$) [60, 61], Pt [62], and Ta [57] have been used as the electrode sites of thin film microprobes. Since the neural activities are stimulated by charge, it is important to select a material with a high capability of charge delivery. The iridium oxide with a charge delivery capacity as high as 3000 $\mu C/cm^2$ [63] is, by far the best candidate compared to metals such as platinum that has a maximum charge delivery capacity of 400 $\mu C/cm^2$ [62]. However, it should be noted that the amount of charge delivered to the target must neither alter the local pH nor decompose the electrode or neural tissue (i. e., it must remain within the water window).

Polysilicon [37, 64], Au [36, 43], and Ta [37, 57] are popular conductors for the interconnection lines. The advantage of using polysilicon traces over the metal lines is the high interface quality of the polysilicon with the insulator layers deposited by Low Pressure

Chemical Vapor Deposition (LPCVD) technique. Consequently, the chance of insulator delamination from the conductor and ionic diffusion into the encapsulation layer of the interconnection lines will be eliminated. As a result, the electrical characteristics of the microprobe channel will remain stable over the courses of long-term experiments. However, the higher sheet resistance of the polysilicon compared to those of the metals becomes a limiting factor for microprobes with long interconnection cables and also the multichannel devices with large aspect ratio interconnection lines.

The insulating material encapsulates the interconnection lines to isolate them from each other and the surrounding biological environment. The stable electrical characteristics of microprobes in terms of the electrode's impedance mostly depend on the resistivity of the insulator against chemical erosion and ion migration. The commonly used dielectric materials are silicon nitride [33], nitride/oxide stacked layers [36,37,64], polyimide [34,43], hard-baked potoresist (PR) [41], and parylene-C [30].

The following sections concentrate on the fabrication methods of the intracortical and DBS microprobes. The multisite intracortical devices are mostly constructed based on thin film processing technologies while the DBS microprobes are produced mainly by conventional approaches.

## 2.1 Intracortical Microprobes

The cerebral cortex of the brain is a highly folded layer of neurons with a typical thickness of less than 5 mm in humans [65]. Based on MEMS and micro-fabrication technologies, many approaches has been proposed to produce microprobes that provide short penetrating shanks suitable for cortical stimulation and recording. Here, the silicon-based implants, metal electrode arrays, and microprobes constructed from polymers are discussed. The fabrication process, properties, and limitations of each type of microprobes are addressed.

### 2.1.1 Silicon-based Microprobes

Biocompatibility, mature processing technology, and the possibility for the integration of on-chip circuitry have been strong motivations for the application of silicon as the structural layer of thin-film microprobes. The silicon-based microprobes can be grouped into three main categories:

- Michigan Probes
- DRIE Probes
- Utah Probes

Boron diffusion and bulk etching of silicon is employed to construct the first category of microprobes. To fabricate the second type of implants, the microprobe shanks are defined in a Deep Reactive Ion Etching (DRIE) process. In the third category, an array of micro-needles is created by cutting deep trenches into the bulk of a silicon substrate using a dicing saw. The details of the fabrication process and shortcomings of each method are discussed in the following sections.

#### Michigan probes

In the early 1970s, K. D. Wise and his coworkers reported the first thin film microprobe [55, 56]. The fabrication of these devices is based on the deep boron diffusion of silicon, followed by the selective etching of the un-doped regions. It is known that a high concentration of boron diffusion dramatically decreases the etch rate of silicon in etchant solutions such as Ethylene-Diamine-Pyrocatechol (EDP) or potassium hydroxide (KOH). The etching of silicon in EDP is effectively stopped when the boron concentration exceeds the approximate values of $5 \times 10^{19}$ $cm^{-3}$ [66]. In the KOH etching process, the etch rate of boron-doped

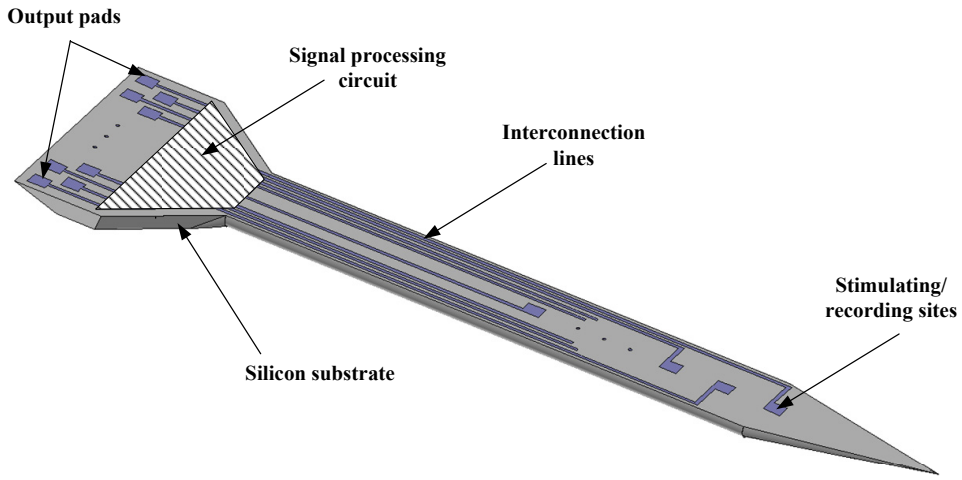


**Fig. 2.1: Schematic of a Michigan microprobe.**

silicon drops by three orders of magnitude for doping densities higher than $1.5 \times 10^{20}$ $cm^{-3}$ [67].

A typical schematic of a Michigan probe is shown in Fig. 2.1. The silicon substrate is micromachined to create the probe shank and the support base where the output pads and on-chip signal processing circuitry are located. The interconnection lines are formed on the probe shank and provide connection to the stimulation/recording sites. To facilitate the handling of the samples during the fabrication, the substrate underneath the output pads is kept thicker than the probe shank.

Fig. 2.2 illustrates the fabrication sequence of a Michigan probe [7, 36–40]. The fabrication starts with the growth and patterning of a silicon oxide layer as the mask that defines the shape of probe shanks by confining the profile of the subsequent boron doping in the substrate. After a deep boron implantation followed by a thermal diffusion process, the mask layer is removed and an insulator is deposited to isolate the electrodes from the highly conductive $p^+$ probe shanks. The chemical vapour deposited (CVD) or plasma enhanced chemical vapour deposited (PECVD) stacked layers of silicon nitride and silicon dioxide films are typically used as the insulator. This is to reduce the mechanical stress in

the insulator layer and to improve the resistivity of the material against the ionic fluids. Next, a conducting film such as gold, tantalum, or polysilicon is deposited and patterned to form the interconnection lines. The deposition of another insulator layer encapsulates the interconnection lines while the via holes are dry-etched exposing the electrode sites and the bonding pads. To enhance the electrical characteristics of the microprobes, Ir or $IrO_x$ is deposited as the electrode sites and patterned in a lift-off process. The bottom and top insulators are then removed from the surface of the substrate except over the microprobes. Finally, the silicon substrate is thinned in an isotropic silicon etchant followed by releasing the device in EDP or KOH solution. The etchant solution dissolves the n-type, undoped,

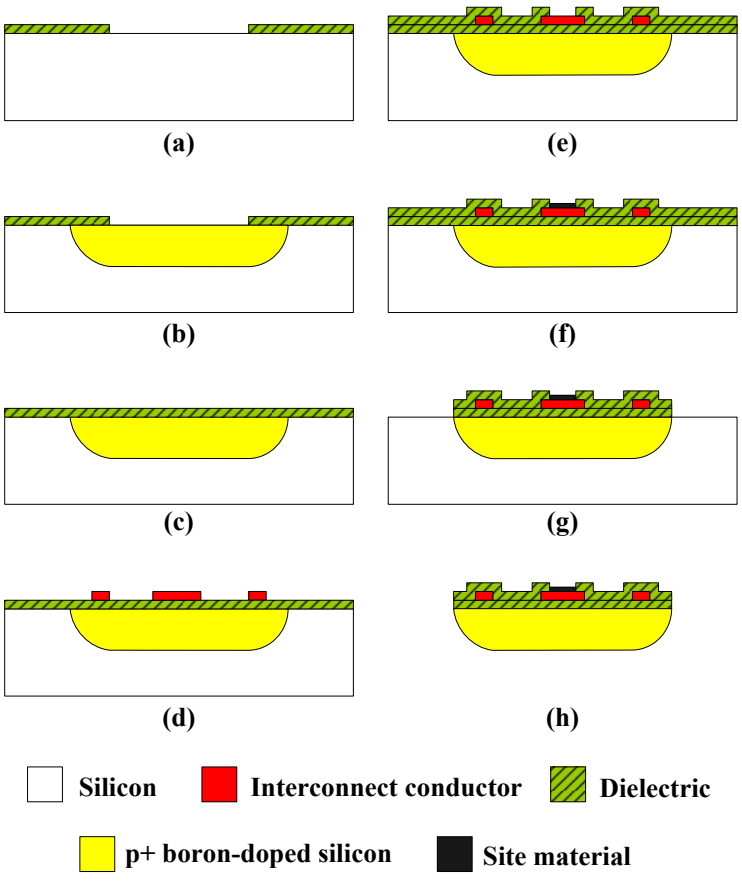


**Fig. 2.2: The fabrication process of Michigan microprobes.**

and lightly p-type doped silicon, but does not attack the $p^+$ layer of the microprobe. The backside processing has also been used to leave a thicker silicon layer under the output pads to facilitate the microprobe handling. An important benefit of this method is the possibility to adopt standard CMOS processes for the integration of an on-chip signal processing unit with microprobes.

Fig. 2.3(a) shows an optical micrograph of a fabricated Michigan microprobe [7]. The holes on the probe shanks might help in chronic applications by stabilizing the probe's position inside the tissue. To increase the number of stimulation/recording sites, several multi-site probe shanks can be bundled together as in Fig. 2.3(a). A shallow boron-diffusion has been carried out to form the tapered shape of the probe tip, as illustrated

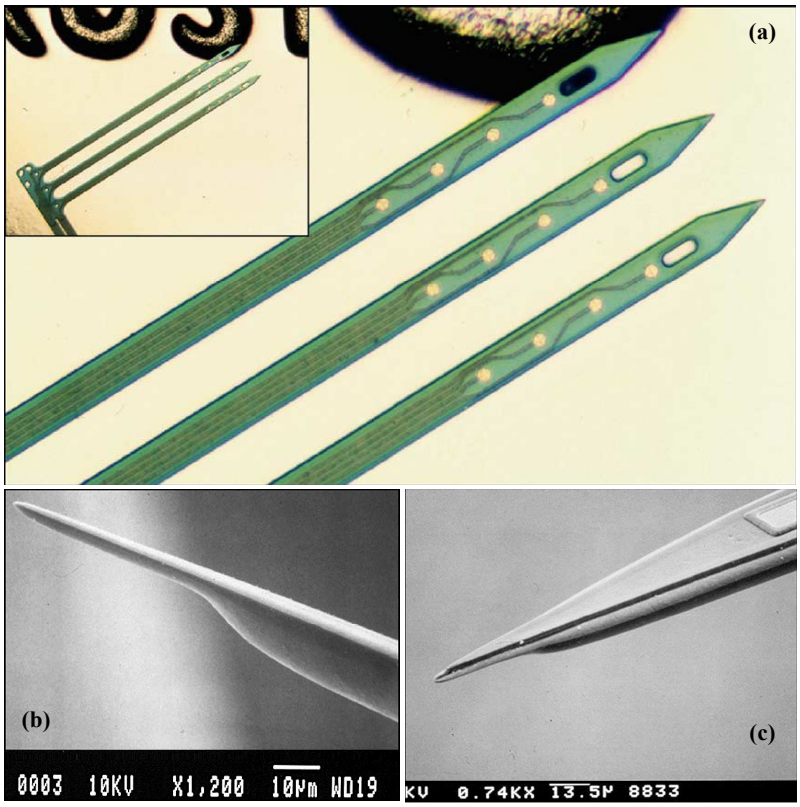


**Fig. 2.3: (a) Photograph of a three-shank microprobe with 12 electrode sites. (b) and (c) The SEM images of a probe tip shaped by shallow and deep boron diffusions [7].**

in the side view SEM images of Fig. 2.3(b) and 2.3(c) [7]. Although the second diffusion step increases the complexity of the fabrication process, it helps to reduce the amount of pressure needed for the penetration of the probe into the tissue. The probe thickness can be adjusted in the range of a few hundred nanometres [68] to 15 $\mu$m or more [37] by controlling the diffusion process. In this technique, the width of the probe shank is defined by the implantation mask and the lateral diffusion occurring at the annealing step. To further reduce the width of the probe, a Deep Reactive Ion Etching (DRIE) process can be conducted to eliminate the effect of lateral diffusion.

The fabrication of 3D electrode arrays was later reported by the Michigan group [7,69]. Several multi-shank Michigan microprobes are assembled on an orthogonal platform using spacers to hold the planar devices parallel to each other. The electrical connection between the microprobes and the platform is produced by thick gold-plated tabs bonded to the contact pads of the platform. A photograph of a 3-D microprobe array with 128 shanks and 1024 electrode sites is presented in Fig. 2.4.

The Michigan probes have also been modified to offer micro-fluidic channels for drug delivery at cellular levels [64]. A few steps must be added to the fabrication sequence for

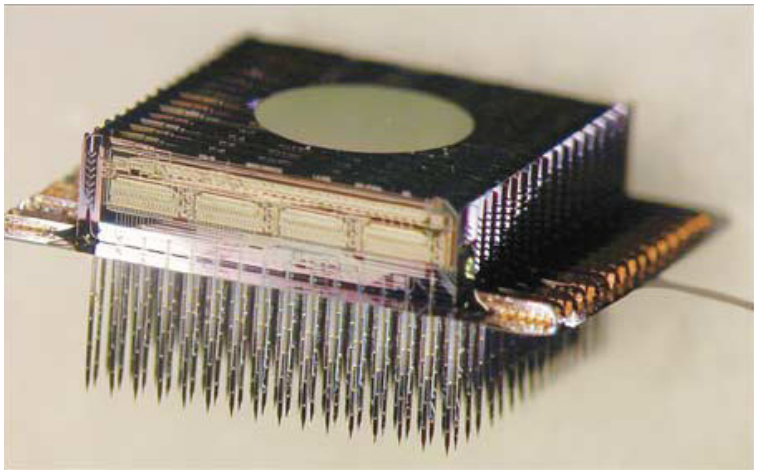

**Fig. 2.4: Optical image of a 3D Michigan microprobe array with 1024 electrode sites [7].**

creating the micro-channels (Fig. 2.5(a)). After the patterning of the thermal oxide layer (the mask for the $p^+$-doping step), a shallow boron diffusion is carried out, and narrow trenches (1 $\mu$m wide) are cut through the thin $p^+$ layer. Then, the anisotropic etching of the silicon substrate in the EDP solution forms the fluidic channels as seen in Fig. 2.5(b). The sidewalls of the channel are along the <111> crystallographic planes if the channel is aligned with the (110) direction. Next, the deep boron diffusion defines the probe thickness,

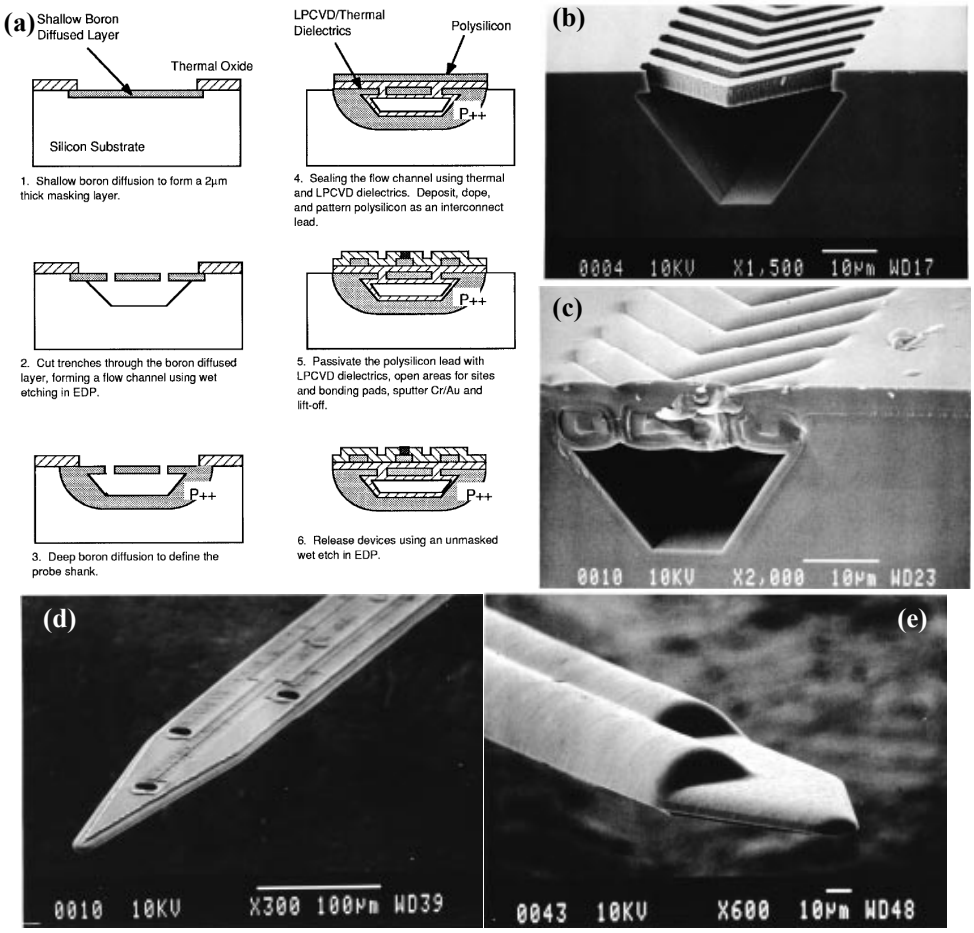


**Fig. 2.5: (a) The summary of the process flow for the fabrication of a Michigan microprobe with embedded micro-fluidic channels. Cross-section SEM images of a fluidic channel after (b) EDP etch and (c) sealing the top dielectric. (d) Top-side and (e) back-side SEM images of a microprobe. (compiled from [64])**

and the micro-channels are sealed by a 0.5 $\mu$m thermally grown oxide layer stacked with a 0.6 $\mu$m LPCVD oxide film (Fig 2.5(c)). To planarize the oxide surface, the wafer is coated by PR and a dry etching process is performed with the same etching rate for both the oxide and PR. The SEM images of the microprobe with three embedded micro-fluidic channels are presented in Fig. 2.5(d) and (e). The micro-fluidic channels are extended from the back of the device and form pipe-like structures for easy attachment to flexible micro-pipettes. It has been demonstrated that a 4 mm long channel with an effective diameter of 10 $\mu$m can flow 87 pl of fluorescent dye into water with a drive pressure of 10 psi applied for 100 ms [64].

The electrical and mechanical characteristics of the interconnection cable connecting the microprobe to the external circuitry is crucial particularly in chronic applications. The cables must be biocompatible and mechanically robust to withstand the manipulation forces experienced by the device during the implantation process. Moreover, a flexible cable is demanded to reduce the damage resulted from the relative micro-motion between the tissue and the microprobe.

The silicon-based ribbon cable, fabricated with a process similar to the Michigan probes, has been proposed to fulfill some of the requirements [70]. A shallow high-dose boron diffusion, followed by an EDP etching process is used to define a thin ribbon-shaped substrate hosting the interconnection lines. The silicon cables and Michigan probes can be integrated in a single fabrication run conveniently providing the connection between the microprobe and the cable. The silicon cables exhibit an out-of-plain flexibility and very low leakage currents in the subpicoamp range even after four years of in-vitro experiments [70]. However, the silicon cables break when subjected to in-plane bending, stretching, and twisting. Moreover, the production of centimetre-long cables is not practical and the associated fabrication yield is low due to the high aspect ratio of the structure.

In summary, Michigan probes with multiple stimulating/recording electrodes and em-

bedded micro-fluidic channels have been successfully produced and integrated with flexible interconnection cables and on-chip electronic circuitry. Nevertheless, the breakable structure and rigidity of the device limit many applications particularly for long-term research and treatments. Furthermore, the Michigan method is only capable of fabricating devices with electrode sites placed on a single side, i.e. the top surface, of the microprobe.

### DRIE probes

Deep Reactive Ion Etching (DRIE) has been alternatively employed to construct the Si penetrating shanks of the intracortical microprobes [71–75]. In one approach, the implants are fabricated on Silicon-On-Insulator (SOI) wafers where the buried oxide layer of the substrate serves as the etch stop of the DRIE process. Consequently, the microprobe thickness is defined by the thickness of the top silicon layer of the SOI wafer. The multisite microprobes with embedded micro-fluidic channels have been successfully produced based on this method. The fabrication process, shown in Fig. 2.6, starts with the deposition of a dielectric film and the RIE etching of via holes in this layer. Through these openings, the silicon is etched in an isotropic etching solution to undercut the dielectric layer. Next, the sample is immersed in a KOH anisotropic etchant to create micro-channels with a trapezoidal cross-section [72]. The second dielectric deposition covers the dielectric holes and completes the fabrication of the micro-fluidic channels. Similar to the Michigan probes, the microelectrode arrays are formed on top of the channels. Finally, the shape of the microprobe is defined by DRIE, and the shanks are thinned by another DRIE process from the backside of the wafer. The buried oxide layer acting as the etch stop of the backside DRIE process is then removed in a dry-etch step to release the device.

The SEM images of a DRIE SOI-based microprobe and a 10 $\mu$m $\times$ 10 $\mu$m Ir electrode site are illustrated in Fig. 2.7. The fabricated probes offer 8 shanks each including 4 electrode sites. The microprobes are 20 $\mu$m thick, and the length of the shank can be

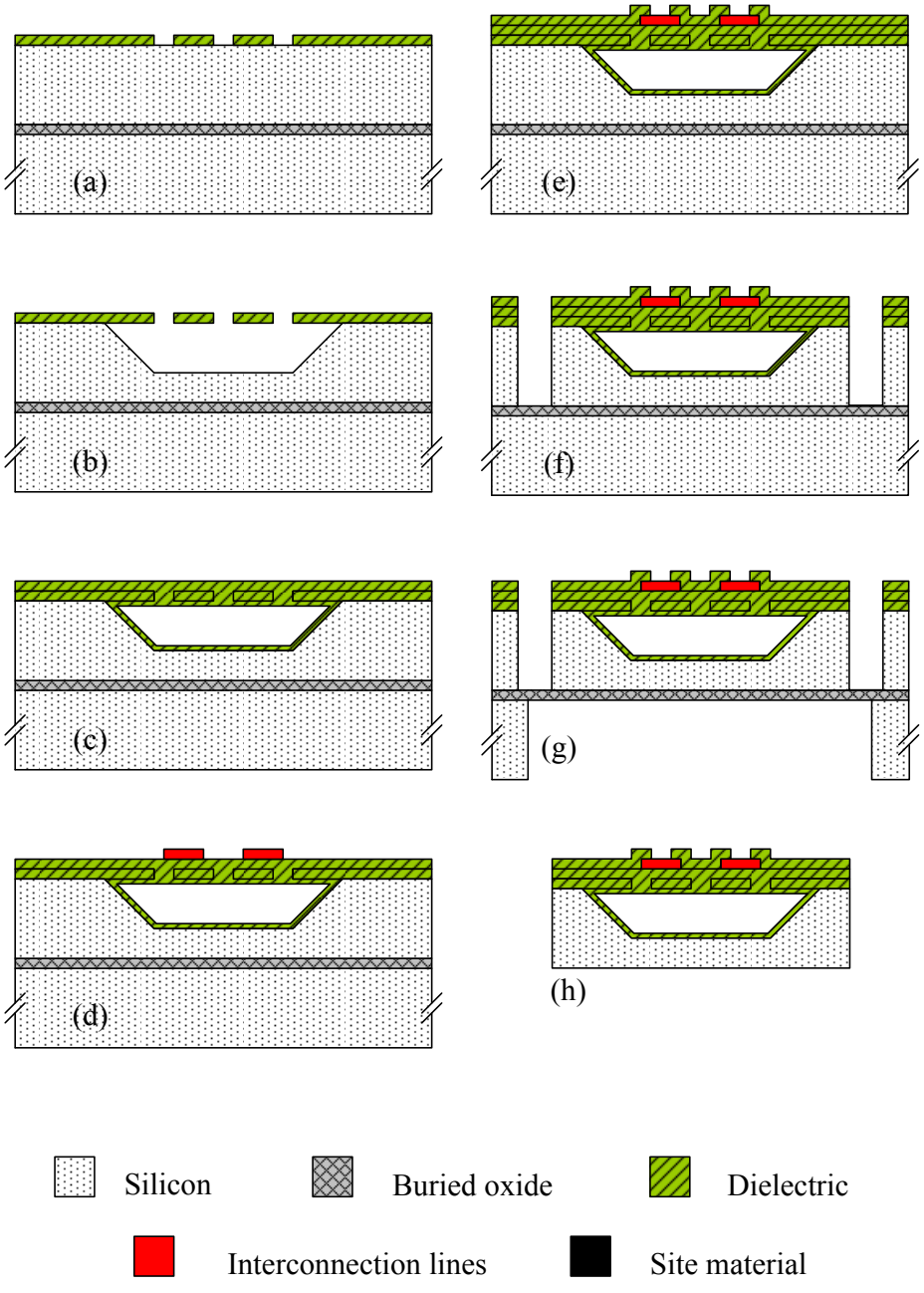


**Fig. 2.6: Fabrication sequence of the DRIE SOI-based microprobes.**

as long as 7 mm [71]. The fabrication of the microprobes with longer shanks is possible by increasing the thickness of the substrate to provide sufficient mechanical strength for implantation. Since the thickness of a DRIE SOI-based microprobe can be easily adjusted

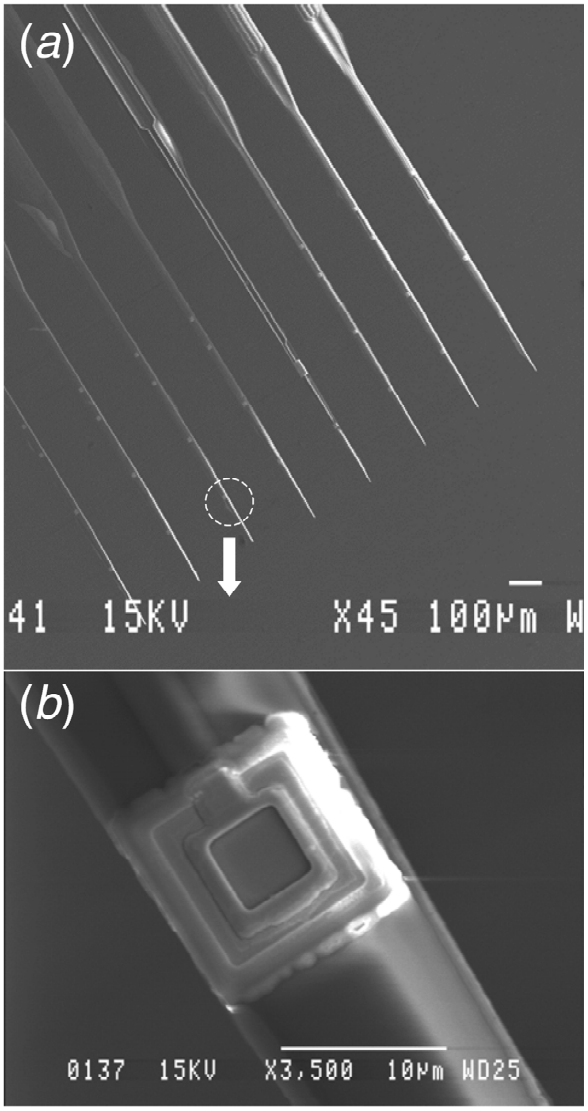


**Fig. 2.7: SEM images of (a) a SOI-based microprobe and (b) an Ir electrode site [71].**

by selecting a wafer with the desirable top silicon layer thickness, this method is preferred for the production of longer microprobes than those produced by the Michigan process. Furthermore, the application of DRIE for defining the shape of the structure provides an excellent control over the device geometry such as the probe width and the tip angle.

The DRIE etching of the regular Si wafers has also been employed for the construction of

intracortical microprobes [74,75]. This method relies on the time etching of the Si substrate in the DRIE step; thus there is no precise control over the thickness of the shanks unlike the SOI-based devices. Other fabrication complexities include non-uniform etching across the wafer and an increased surface roughness of theses devices. Despite such difficulties, advanced 3D probes with embedded micro-fluidic channels similar to the Michigan arrays have been recently reported.

To finalize this section, a few issues associated with operation and reliability of the DRIE microprobes are mentioned. Similar to Michigan probes, these implants are rigid and breakable. The DRIE microporbes also have a single-sided configuration in which the electrodes are placed only on the top surface of the device. Moreover, these devices are not integrated with flexible interconnection cables, although it is possible to adopt the Michigan approach or other post processing methods to produce an integrated flexible cable.

### Utah probes

Arrays of Si micro-needles for cortical stimulation and recording were developed by P. K. Campbell and his coworkers from the University of Utah in the early 1990s [76]. The micro-needles are constructed from a thick monocrystalline Si wafer. In the early devices, $p^+$ Si pillars were produced in an n-type silicon substrate in an aluminum thermomigration process across the wafer. These $p^+$ regions are electrically isolated from each other by the back to back pn-diodes formed between the n-doped substrate and $p^+$ regions. Although functional microprobes were produced based on this method, the fabrication yield was low and the electrical characteristics of the electrodes were non-uniform and sensitive to the surface conditions [77]. Later, the Utah group used highly doped Si wafers for the construction of the array and employed glass barrier regions to isolate the electrode needles [77].

The schematics of the sample at different stages of the Utah process for the fabrication of an intracortical microprobe are depicted in Fig. 2.8. First, 300 $\mu$m deep orthogonal grooves are made in the substrate using an abrasion type diamond blade dicing saw. The substrate is then coated by a glass slurry and the sample is annealed at 1200 °C to melt the

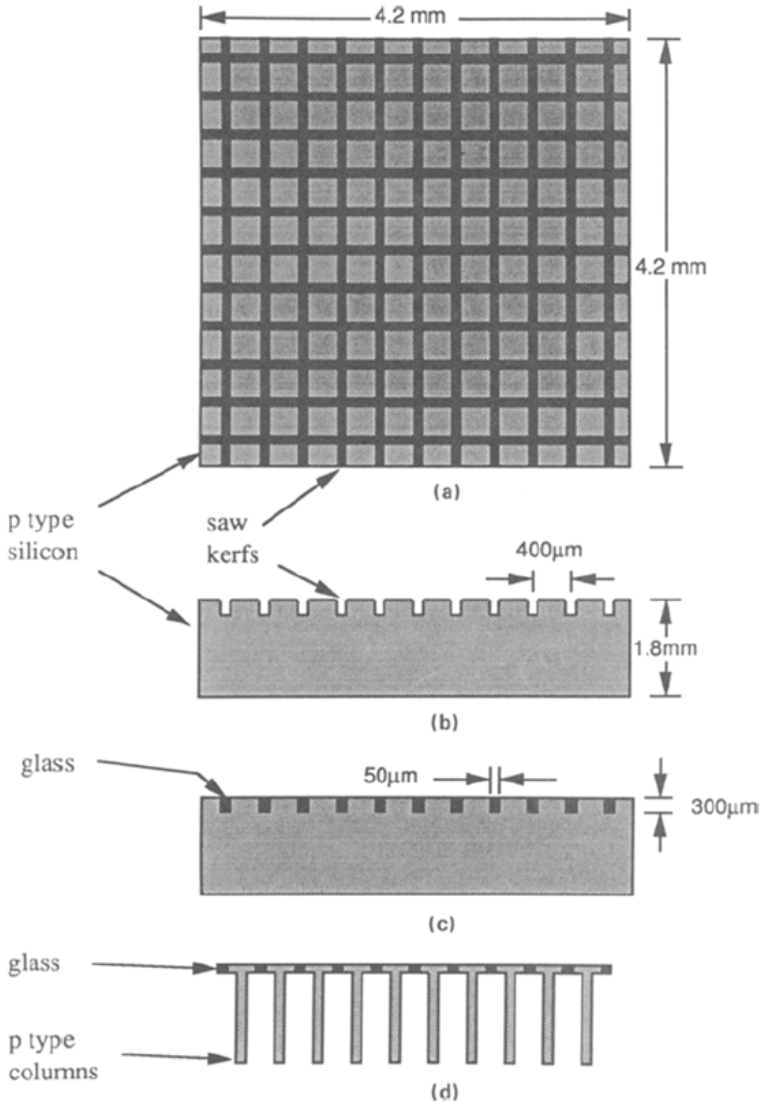


**Fig. 2.8: The sample schematics at different stages of the Utah fabrication process: (a) and (b) after the formation of backside isolator grooves, (c) after glass reflow, and (d) after Si dicing for construction of the micro-needles [77].**

glass. The glass fills inside the grooves and forms the isolating barriers. Next, the sample is planarized and Al pads are formed over silicon islands. From the backside of the wafer, perpendicular trenches are cut directly on top of the glass filled grooves with depth enough to barely penetrate the glass. To sharpen the Si needles and remove the dicing damage, a two step etching process was developed in [76]. Subsequently, gold, platinum, or Ir is deposited at the needles' tips as the electrode sites. Finally, the needles are encapsulated by polyimide and the electrode sites are exposed at the tip in an oxygen plasma etching step. To selectively mask the body of the Si needles during the metal deposition and polyimide etching processes, the array is pushed into a thin metal foil with needle tips extruding 400 to 500 $\mu$m from the surface of the foil. For successful implementation of this procedure, a thin metal foil is stretched over a template including grooves with the same pattern as the needles.

Fig. 2.9 shows an SEM image of a Utah probe consists of a 10 $\times$ 10 array of needle-shaped electrodes [78]. The needles are 1.5 mm in length and 80 $\mu$m in diameter at the

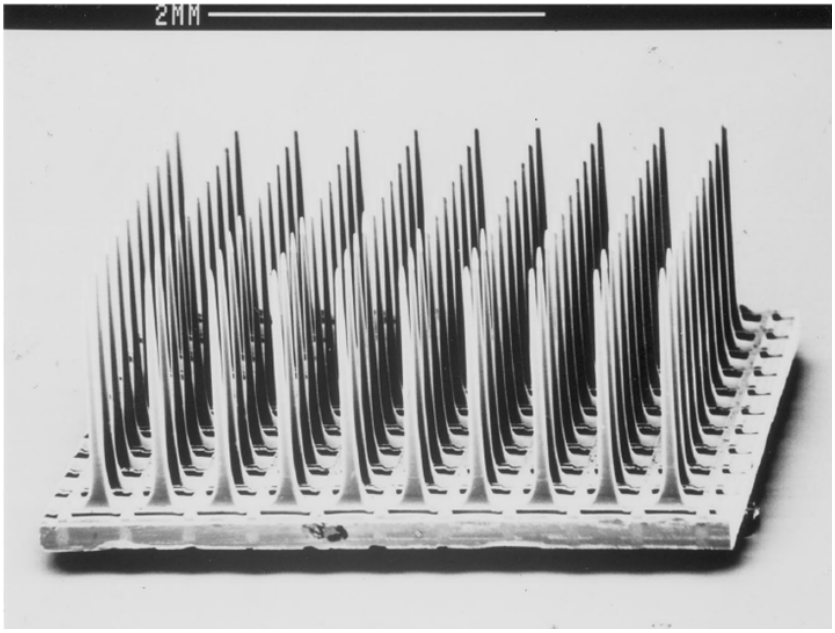


**Fig. 2.9: SEM image of a Utah microprobe [78].**

base. The parasitic impedance between the adjacent electrodes is higher than $10^{13}$ $\Omega$ with less than a 50 fF inter-electrode capacitance. Chronic intracortical recording has been demonstrated with Utah microprobes [77].

Despite the mature fabrication process and stable characteristics of the Utah probes, several issues limit the application of these implantable devices. Although the microprobe has a 3D structure, the electrode sites located at the tip of the needles on a 2D planar array. Each needle provides a single electrode with lengths limited to a few millilitres. The configuration of the probe is similar to a bundle of microwires and as a result the volume of displaced tissue is large and the implantation damage is extensive. Finally, there is no possibility for the construction of microprobes with a 3D matrix of electrode sites.

### 2.1.2 Metallic Microprobes

Metallic beams fabricated by photolithography process have been alternatively used as the mechanical support structure of the microprobes. In general, there are two different types of metallic microprobes presented in literature. In the first category, the interconnection lines and electrode sites are constructed on an encapsulated metallic beam serving as the support structure [41, 43]. In the second group, a metallic beam is utilized both as the mechanical support layer and as the recording electrode [30, 42]. The former category will be referred to as the metallic shank microprobes and the later category as the metal microelectrode arrays.

M. Kuperstein and D. A. Whittington reported one of the first metallic shank multisite microprobes in 1981 [41]. The microprobe was named Parallel Recording Of Neural Groups (PRONG) by the authors and later was referred to as the MIT probe. The electrodes were fabricated on a 17.5 $\mu$m thick molybdenum (Mo) foil sandwiched between two layers of dielectric. PR was employed as the insulating material, while gold was used to form the

interconnection lines, bonding pads, and electrode sites. The microprobes provided 24 rectangular electrode sites that were placed in 2 columns and 12 rows. The length of the microprobe was 2 mm and the area of recording sites was 120 $\mu m^2$.

In another attempt, Blum et al. employed 15 $\mu$m thick Mo substrates to produce metallic shank microprobes [43]. In this method, gold was deposited on both sides of the substrate to protect the Mo probe shank against the etching process. Instead of PR, standard or photo-definable polyimide was used to insulate the interconnection lines. The fabricated microprobes offered four or six square gold electrodes each 30 $\mu$m $\times$ 30 $\mu$m in dimensions.

For the fabrication of the metal microelectrode arrays, the second category of metallic microprobes, electroplating has been employed to produce arrays of metallic beams that serve at the same time as the mechanical support layer, interconnection line, and the electrode [30, 42]. The electroplating process provides excellent control over the physical and electrical properties of the individual electrodes. Furthermore, the distance between the two adjacent electrodes and the position of the electrode sites, can be precisely defined by photolithography technique. To confine the electroplating metal in the lateral direction, a plating mold is formed on top of the seed layer. Xu et al. have employed a double electroplating process to fabricate nickel (Ni) plated microelectrode arrays on Si wafers [30]. The microprobes consist of an array of seven microelectrodes, spaced 50 $\mu$m apart. The SEM images of the microelectrode array and an electrode tip are illustrated in Fig. 2.10 [30].

To fabricate the microelectrodes shown in Fig. 2.10, the first electroplating process was employed to form the electrode tips, and the second process to create the probe shanks. The tip section was 250 $\mu$m long and had a cross section of 15 $\mu$m $\times$ 6 $\mu$m. The thickness of the probe shank was 30 $\mu$m providing sufficient mechanical strength for the 6 mm-long microelectrodes. PR was used to create the plating mold on top of the Cr/Cu seed layer and

Ni was selected as the plating material. After the electroplating, the silicon substrate was etched in a KOH solution to release the electrodes. Since Ni is toxic, the microelectrodes were then coated with a biocompatible metal such as Au or Pt. Next, microelectrodes were encapsulated by a 3 $\mu$m thick layer of parylene-C using a vapour-phase deposition process at room temperature. Finally, the oxygen plasma etching of the insulator at the tip of the electrodes exposed the stimulation sites as observed in Fig. 2.10(b).

Despite the uniform characteristics and good mechanical properties, the metal microelectrode arrays that are fabricated with the electroplating processes are very similar to a bundle of microwires. As a result, compared to the single shank microprobes, the tissue

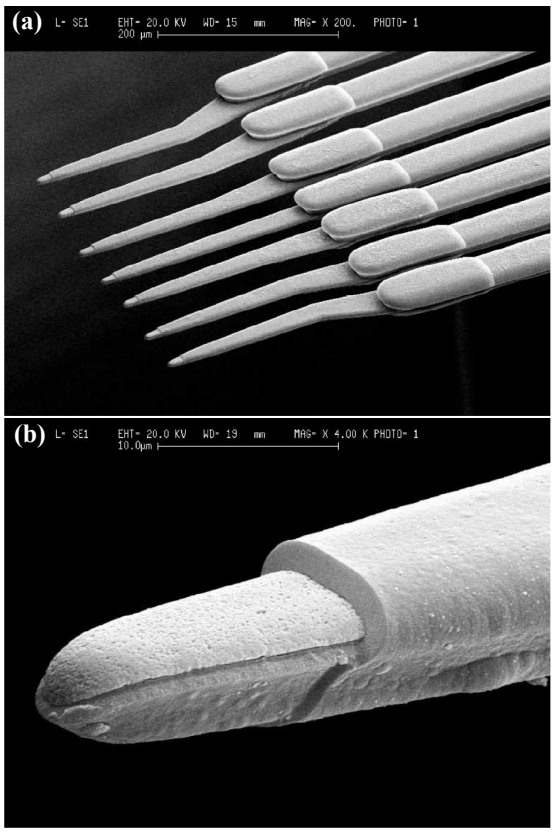


**Fig. 2.10: SEM images of (a) a metal microelectrode array and (b) the electrode site at the tip of an encapsulated metallic beam [30].**

damage introduced during the insertion of the probe is extensive. Since every electrode site requires an additional probe shank, the volume of the microprobe is linearly proportional to the number of sites. Therefore, it is not practical to study a large number or closely located neurons with this type of microprobes. The application of both families of metallic microprobes is also hindered by the structural rigidity and unavailability of integrated flexible cables. Furthermore, the integration of on-chip signal processing units with the microprobes might not be practical. Although long-term operation is expected, limited studies have been carried out on the stability of metallic microprobes in chronic studies.

### 2.1.3 Flexible Microprobes

The relative micro-motion between the neural tissue and a rigid microprobe can gradually damage the neurons located in close proximity of the implant in long-term experiments [47]. More importantly, if the position of the microprobe is displaced from the target location, the functionality of the implanted device is affected [79, 80]. The application of flexible materials as the structural layer of a microprobe can alleviate some of the issues imposed by the device rigidity. Flexible microprobes have been fabricated with shanks made of polyimide [34, 35, 81–83] or Liquid Crystal Polymers (LCP) [84]. Fig. 2.11(a) presents an optical micrograph of a polyimide-based implantable microprobe that consists of 2 arrays of electrodes. Each array has three shanks and utilizes gold as the interconnection lines and the electrode sites. The arrays are connected by a polyimide bridge that can be bent to form a 3D structure as shown in Fig. 2.11(b) before the implantation. The thickness and width of the microprobe shanks are $\sim$ 20 $\mu$m and 160 $\mu$m, respectively.

The fabrication of a polyimide-based microprobe starts with the deposition or growth of a thin sacrificial layer on a rigid substrate such as silicon or glass. Then, polyimide with a typical thickness of 10 - 20 $\mu$m is spin-coated and cured. Next, a metal layer is

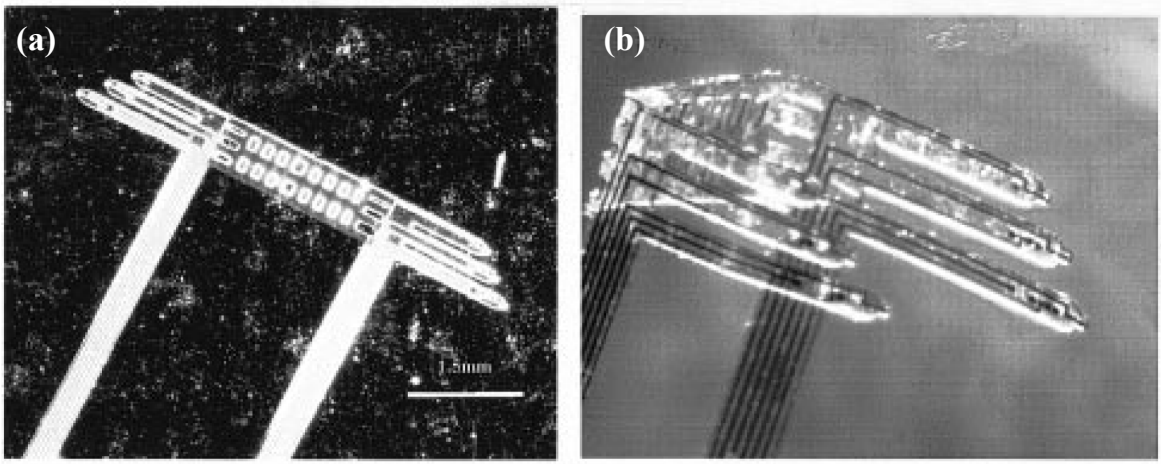


**Fig. 2.11: Photograph of (a) a polyimide-based microprobe and (b) the planar device bent into a 3D structure [34].**

deposited and patterned to form the electrodes and interconnection lines. The second layer of polyimide encapsulates the electrodes. In an RIE dry etching step, opening vias to electrode sites and the bonding pads are created and the polyimide layers are etched to define the probe shanks and interconnection cables. Finally, the sacrificial layer is removed in a wet etching process to release the microprobe. Additional processing steps can be added to deposit Pt or Ir over the electrode sites.

One of the key advantages of flexible microprobes is the integration of an extremely flexible interconnection cable with the implant. Stable electrical characteristics of polyimide-based microprobes have been also reported in long term experiments [85]. Despite such superior properties, the flexible microprobes cannot penetrate the tissue and must be implanted by a microsurgical tool. In [86] flexible probes have been fabricated on a 5 - 10 $\mu$m thick Si layer to enhance the mechanical strength of the device. Although this method provides a flexible joint, fabrication of a multisite microprobe integrated with a centimetre long flexible cable has not been reported yet.

## 2.2 DBS Microprobes

A microprobe with a few centimetre-long penetrating shank is demanded to interact with the deep structures of the brain such as the thalamus and hippocampus. Furthermore, the cross section area of the device must be as small as possible to minimize the tissue damage. These dimensional constraints complicate the production of DBS probes to such an extent that most MEMS and micro-fabrication technologies cannot be practically employed. By far, fewer reports exist in literature on DBS devices and the majority of the implants are constructed by conventional approaches. In this section, the structure, design, and fabrication of DBS microwire bundles, Medtronic DBS leads, and 3D electroplated metal microprobes are reviewed.

### 2.2.1 Microwire Bundles

The insulated metal microwires have a broad application in neurophysiological studies thanks to their robust mechanical properties, stable electrical characteristics, and easy production. The bundles of metal electrodes are among the rarely reported devices for deep brain micro-stimulation and recording [27, 52]. In one approach, 8 microwires were twisted around an Ir / Pt core and cut at one end to expose the electrode sites [52]. The overall diameter of these so called Niotrodes can be as small as 100 $\mu$m. Alternatively, Ir wires with diameters of 75 $\mu$m were assembled to create a multisite probe with 16 electrode sites [27]. Each wire was electrolytically sharpened into a cone shaped tip and encapsulated with parylene-C. Next, the insulator at the tip of the electrodes was ablated using an excimer laser and the wires were assembled in a custom fixture. The fixture aligns the wires and serves as a mold to construct the epoxy cap that holds the electrodes. Fig. 2.12 illustrates the images of a fabricated DBS microprobe and the tip of an electrode. This device measures 16 mm in length and 2 mm in diameter.

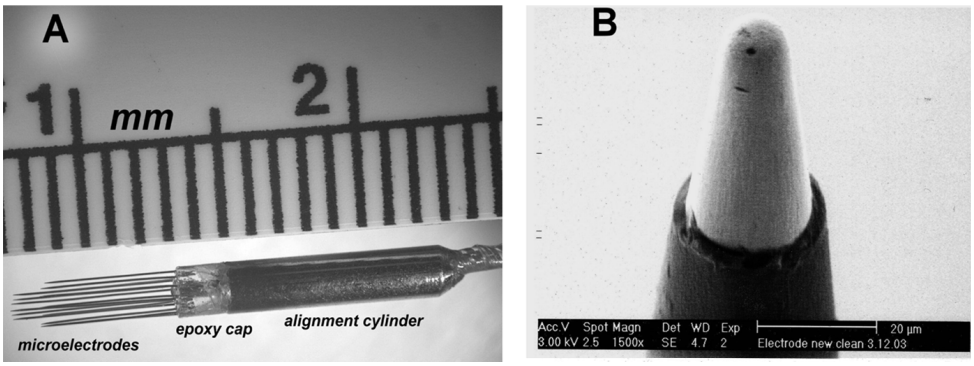


**Fig. 2.12: (a) Optical image of a DBS microwire bundle and (b) SEM micrograph of an electrode tip [27].**

There are several issues associated with the functionality and design of DBS microwire bundles. Although it is possible to employ these devices in short-term studies, the chronic application is limited by the large volume and rigidity of the microprobe. In addition, for most treatments, the offered electrode sites with micrometre-scale dimensions are too small for stimulating an adequate section of the tissue. Moreover, the position of microwires inside the bundle cannot be precisely controlled, the process is extremely time-consuming, and the fabrication yield is low.

### 2.2.2 Medtronic DBS Lead

The DBS for treatment of movement disorders such as advanced Parkinson's disease and essential tremor is currently performed by Medtronic DBS leads. These chronically implantable probes are 1.27 mm in diameter and 10 - 50 cm in length offering 4 cylindrical electrodes each 1.5 mm in height. As shown in Fig. 2.13, two versions of the Medtronic leads are available with 0.5 mm and 1.5 mm inter-electrode spacings. The outer jacket of these implants is made of urethane A80, and Ir / Pt alloy is used as the electrode sites and conductor wires [50].

**Fig. 2.13: Medtronic DBS lead.**

Although Medtronic lead is commercially available, limited information has been published on the fabrication of this device. A possible method of construction has been presented in [87] and schematically illustrated in Fig. 2.14. Pt / Ir wires are wound around a tungsten core and placed inside the mold used to shape the polyurethane outer jacket of the implant. The structure is then released from the mold and the extruding metal wires and polyurethane parts are cut. Next, the electrode sites are formed, the tungsten core is

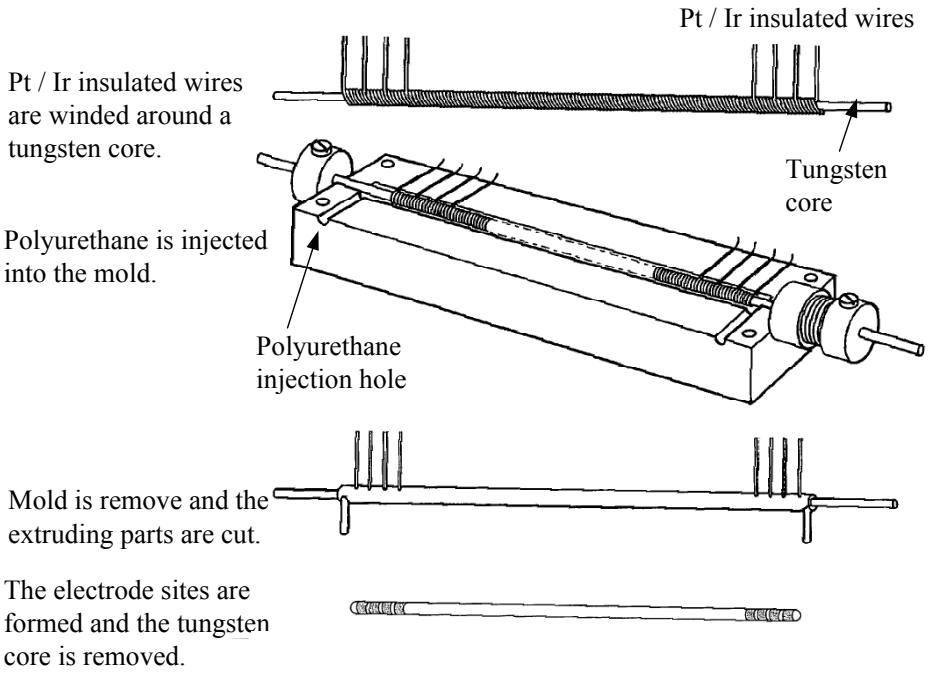


**Fig. 2.14: A possible method of fabrication for Medtronic leads compiled from [87].**

removed, and the penetrating end of the probe is capped. For implantation, a rigid stylus can be inserted into the hollow section of the probe to guide the device into the brain.

The Medtronic DBS lead satisfies many requirements for a stimulating microprobe such as a flexible structure and large electrode sites. Despite such desirable characteristics, it is not possible to adjust the profile of injected charge into the tissue. Indeed, the cylindrical shape of the electrodes can only generate symmetric electric fields and currents around the implant. Furthermore, no recording channel is offered by the Medtronic leads thus the DBS treatments are open loop and no feedback is collected from the response of the brain to the stimulating pulse. The dimensions of the device are also large resulting in extensive tissue damage.

### 2.2.3 3D Electroplated Metal Microprobes

P. S. Mota and J. W. Judy recently presented long microprobes for DBS based on microfabrication technologies [33]. An electroplating process was developed to produce customizable 3D structures in [88]. In this process, the electroplating is performed on a patterned seed layer without employing a confinement mold. Initially, the electroplating starts on the regions of the seed layer that are electrically connected to the power supply, and no metal growth happens on the isolated regions. In the absence of a plating mold, the metal growth proceeds in both vertical and lateral directions. If the plated film contacts to an isolated seed layer, the plating also takes place on the newly connected seed layer. To employ this method for the fabrication of the microprobe structural layer, the microelectrode array is initially constructed upside-down on a silicon wafer. On an oxide-covered silicon wafer, nitride is deposited and patterned to define the electrode sites openings. Then, the electrode sites, interconnection leads, and output pads are formed and encapsulated by the second layer of the silicon nitride. Next, the electroplating process on a patterned seed

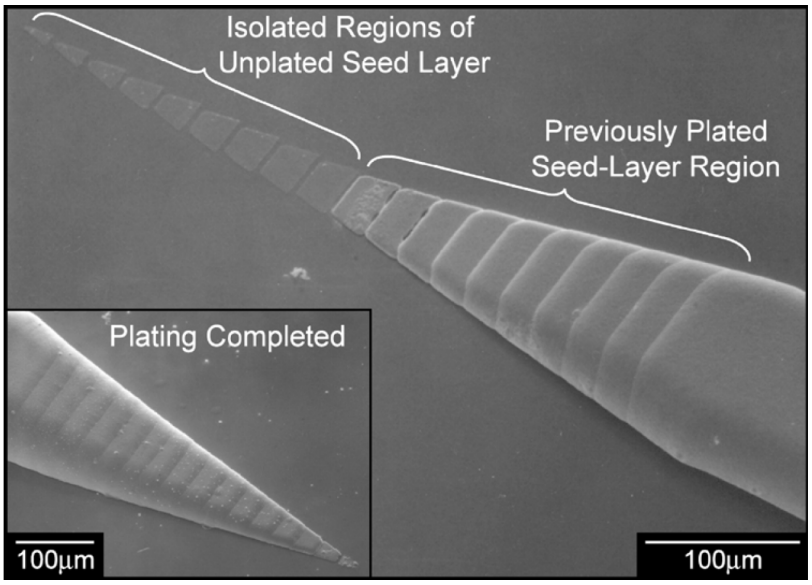


**Fig. 2.15: SEM image of a probe shank in the middle of the electroplating step. The completed structure is shown in the inset [33].**

layer completes the microprobe structure. The final step is etching the silicon wafer in KOH and removing the oxide layer in a buffered HF solution. A SEM image of a probe shank during and after the completion of the electroplating process is displayed in Fig. 2.15 [33]. The patterns' dimensions and the distances between seed layer islands control the slope of the tapered probe tip. Fig. 2.16 illustrates the back-side image of the microprobe where the microelectrode array is located. Platinum was selected as the site material of the fabricated devices with penetrating shanks as long as 22 mm.

This fabrication method provides excellent control over the width, length, thickness, and 3D shape of the microprobe. Moreover, the electrode sites' dimensions and density are precisely defined by a high resolution lithography process, and the device volume can be substantially scaled. Yet again, these devices suffer from several issues commonly associated with most metallic microprobes. Although the fabrication of long DBS microprobes is possible by increasing the thickness of the shank, the device rigidity prevents their ap-

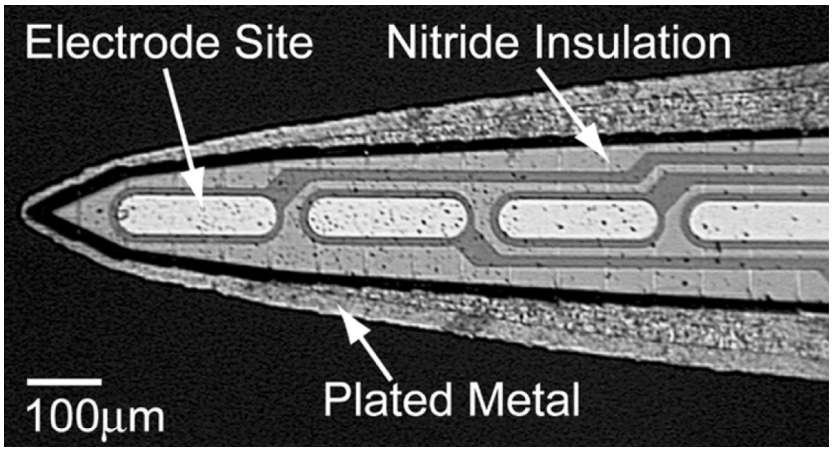


**Fig. 2.16: SEM image of the microelectrode array fabricated on the backside of the electroplated shanks [33].**

plication in long-term studies. A flexible interconnection cable is not integrated with the implant and the electrode array has a planar configuration. The single side planar configuration of the device is not preferred for the stimulation of a symmetric volume of the brain and the probe is not fully capable of steering the electric field in the tissue.

## 2.3 Electrical Characteristics

The sensitivity and Signal to Noise Ratio (SNR) of the recorded neural activities and the maximum charge that can be delivered to the tissue at a certain stimulation voltage are mainly determined by the impedance of the implanted electrode. Materials such as Ir and $IrO_x$ that have a high capacity of charge delivery and inert chemical properties are preferred for the application as the electrode sites of the neural microprobes [7, 33]. An equivalent circuit model for an electrode immersed in an electrolyte solution is depicted in Fig. 2.17 [41]. The circuit consists of several frequency-dependent resistances and capacitances. In this model, $Z_e$, $R_m$, $C_c$, and $C_{sh}$ are the impedance between the recording

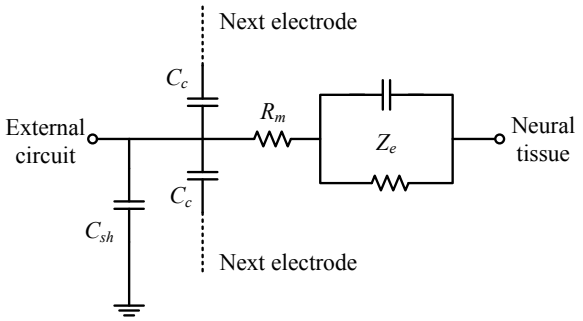


**Fig. 2.17: Equivalent circuit of a microelectrode.**

site and the tissue, the resistance of the interconnection line, the coupling capacitance to adjacent electrodes, and the shunt capacitance to ground, respectively. The impedances of the stimulating and recording electrodes as a function of frequency for gold and Ir electrodes are presented in chapters 3 and 4. In general, the impedances of the microelectrodes follow a similar trend in frequency, although the exact value of the impedance depends on the material used as the electrode site.

To determine the long term behavior of microelectrodes particularly in chronic neural stimulation experiments, changes in the impedance value of the electrode are monitored when the electrode is subjected to prolonged pulsed voltages [37]. In this study, stable characteristics were observed for Ir sites similar to prior reported results in [37]. To enhance the performance of the electrodes, it is possible to grow $IrO_x$ over the Ir surfaces in an electrochemical activation process using acidic or saline solutions [89, 90]. Although a significant reduction in the impedance magnitude has been demonstrated, the extended range of the activation voltages results in unstable impedance behaviour. That is, the impedance is low at the beginning and gradually increases and stabilizes at a value close to that of an unactivated Ir electrode [37]. The SEM study revealed that during the pulse test, the $IrO_x$ layer cracks and eventually delaminates from the underlying Ir metal. Therefore, in chronic applications, the Ir electrodes with higher characteristics stability are preferred over $IrO_x$. Indeed, the electrode sites of the Medtronic DBS leads are constructed from Ir / Pt alloy despite the lower charge injection capacity and higher impedance values.

## 2.4 Summary

Neuroprosthetics employ multisite microprobes to monitor and/or electrically stimulate the activity of the neurons in the central nervous system. Metal microwires, glass electrodes, and the bundle of microwires are the earliest devices used in neural studies and treatments. Micro-fabrication technologies were later employed to construct advanced implantable devices known as thin film microprobes. These devices provide an array of electrodes to interact with many closely located neurons. Intracortical and DBS microprobes are the main categories of invasive implants with penetrating shanks. The intracotrical devices target the cortex while the DBS microprobes interface with the deep structures of the brain.

Silicon substrates, metals, and flexible polymers have been employed as the structural layer of the intracortical devices. The design, structure, and fabrication process of the main types of implants were comprehensively reviewed. An advanced neural microprobe must offer integrated flexible interconnection cables, on-chip signal processing circuitry, and a high density 3D array of electrodes. A compact summary of the capabilities and limitations of the most mature fabrication methods is provided in Table 2.1.

Microprobes with several centimetres long penetrating shanks are demanded for DBS applications. Implantable devices with such lengths are mainly constructed with conventional methods such as micro-assembly and polyurethane casting. An electroplating method has also been reported to produce multisite microprobes with 3D structures. To improve the efficacy of the DBS treatments, multisite 3D probes are demanded for simultaneous stimulation and recording with the capability to adjust the distribution of the injected charge. Table 2.2 summarizes the features and shortcomings of several DBS devices.

At the end of the chapter, a simplified equivalent circuit was introduced to model the

**Table 2.1: Limitation and capabilities of intracortical microprobes**

| Microprobe | Capabilities | Limitations |
|---|---|---|
| Michigan probes [7,64] and DRIE probes [71, 74] | – Mature fabrication<br>– 3D electrode arrays<br>– Multisite shanks<br>– Integrated circuitry<br>– Small tissue damage | – Rigid and breakable<br>– Limited flexibility of the interconnection cable<br>– Electrodes placed on single side of the probe |
| Utah probes [76, 77] | – Mature fabrication<br>– Multisite<br>– Mechanically robust | – Not integrated with flexible interconnection cable<br>– Single site per shank<br>– Short penetrating shanks<br>– Extensive tissue damage<br>– No on-chip circuitry<br>– Rigid |
| Metal microelectrode arrays [30, 42] | – Simple fabrication<br>– Excellent impedance characteristics | – Single site per shank<br>– Not integrated with flexible interconnection cable<br>– Extensive tissue damage<br>– No on-chip circuitry<br>– Rigid |
| Metal shank microprobes [41, 43] | – Multisite shanks<br>– Small tissue damage | – Not integrated with flexible interconnection cable<br>– No on-chip circuitry<br>– Rigid |
| Polyimide-based microprobes [34, 81, 82] | – Multisite shanks<br>– Small tissue damage<br>– Flexible shanks<br>– Integrated with a flexible interconnection cable | – No on-chip circuitry<br>– Not strong for penetration into the tissue. The device must be implanted using microsurgical tools. |

frequency dependence of the microelectrode impedance. Ir and $IrO_x$ are typically selected as the electrode sites due to the high capacity of the material for charge injection. In long term studies, if a sufficient level of stimulation can be delivered, the stable microelectrode characteristics is of crucial importance rather than the low impedance of the electrode. Ir and Ir / Pt alloys are the most promising candidates and have been used in the commercially available Medtronic DBS lead.

**Table 2.2: Limitation and capabilities of DBS microprobes**

| Microprobe | Capabilities | Limitations |
|---|---|---|
| Microwire bundles [27, 52] | – Provide recording sites<br>– Multisite | – Rigid<br>– Extensive tissue damage<br>– Not suitable for stimulation of a large tissue volume |
| Medtronic DBS lead [50] | – Mature fabrication<br>– Large stimulation sites<br>– Flexible<br>– Stable characteristics | – No recording capability<br>– Only provide 4 channels<br>– Unable to adjust the field distribution inside the tissue<br>– Extensive tissue damage |
| 3D electroplated metal microprobes [33] | – Provide both recording and stimulation capability<br>– Multisite<br>– Excellent control over dimensions / density of the electrodes<br>– Small probe volume | – Rigid<br>– Not integrated with flexible interconnection cable<br>– Electrodes placed on single side of the probe |

# Chapter 3

# Flexible Intracortical Microprobes with Improved Structural Design

The desirable mechanical and electrical characteristics of the intracortical microprobes were pointed out in chapter 1 and the fabrication process, capabilities, and limitations of several microprobes were discussed in chapter 2. The successful development of neuroprostetics systems and brain-machine interfaces demands further progress in the technology and fabrication of implantable microprobes. At present, despite the great advances, non-breakable rigid microprobes integrated with flexible interconnection cables have not been reported and hybrid approaches are adopted to construct such devices.

This research aims to develop novel multisite microprobes for intra-cortical applications offering enhanced functionality and a high degree of biocompatibility. The proposed multisite microprobes provide sufficient mechanical strength at the tip section for penetration into the tissue while integrated with a flexible interconnection cable [91, 92]. The fabrication method is based on surface micro-machining techniques and employs only 3 lithography steps to fabricate the device. Here, the details of the fabrication process, design, and characteristics of the microprobes are presented.

## 3.1 Structure and Design

The proposed intracortical microprobes consist of three major components: the probe tip, the interconnection cable, and the wide substrate section where the bonding pads are located. Fig. 3.1 presents the Three Dimensional (3D) schematics of the microprobe and the probe tip. A flexible interconnection cable connects the electrode sites to the bonding

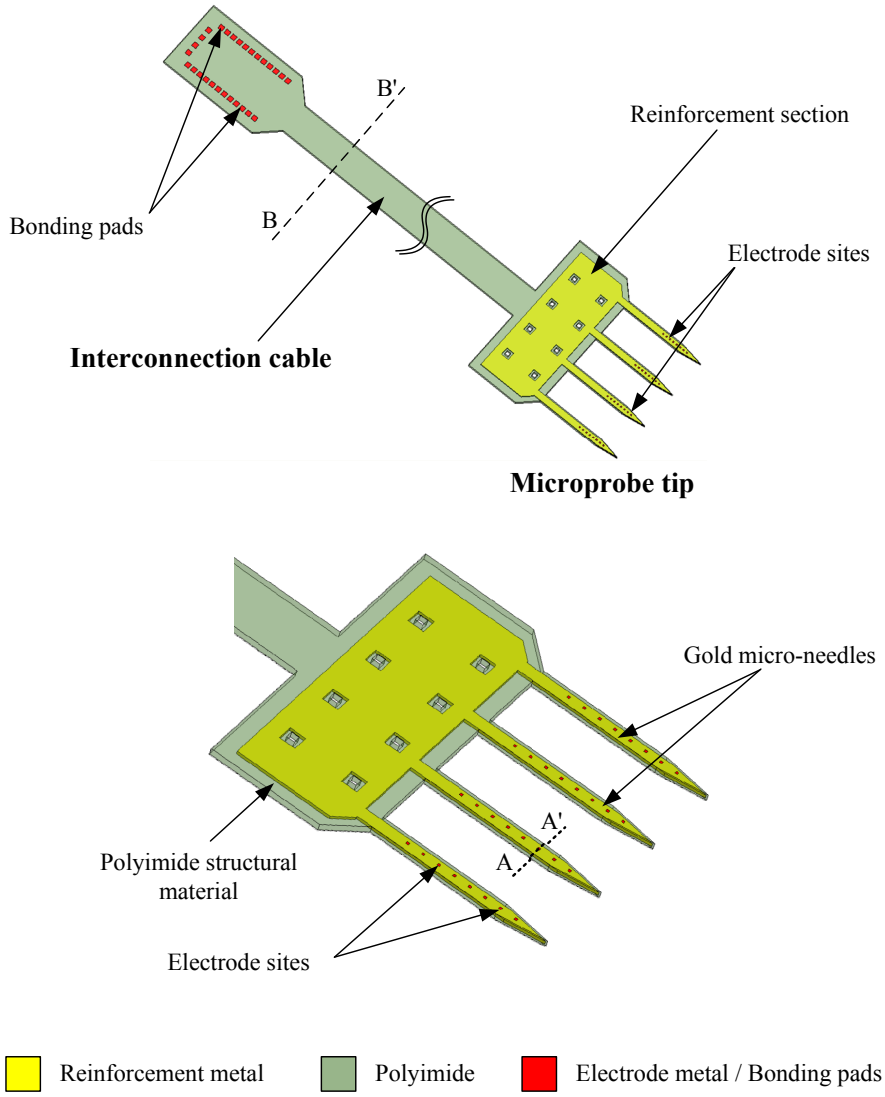


**Fig. 3.1: 3D schematics of the proposed intracortical microprobe.**

pads. Polyimide is employed as the structural layer of the implant to provide a flexible yet non-breakable interconnection cable. To enhance the rigidity of the microprobes at the tip, metallic micro-needles are embedded in the polyimide outer shell. The micro-needles are connected at the base to a rigid support section which facilitates the manipulation of the device during the implantation procedure.

The cross-section schematics of the interconnection cable and microprobe tips are shown in Fig. 3.2. At the tip, a rigid metallic section embedded in the polyimide outer shell locally enhances the rigidity and hence provides the tip with enough strength to penetrate the tissue. To offer the maximum possible flexibility, the interconnection cable only consists of polyimide and thin metal traces which are employed as the addressing lines.

In this work, microprobes with 2, 4, and 8 mm-long probe shanks were constructed to study the limitation and challenges of the proposed method of fabrication. The implants offer as many as 32 electrode sites located on 4 parallel shanks. Table 3.1 lists the design specifications such as the physical dimensions and the electrode count of different fabri-

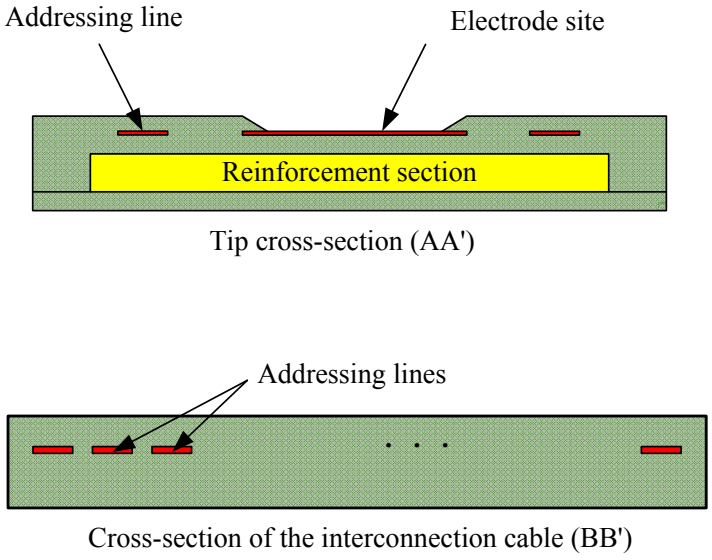


**Fig. 3.2: Cross-section schematics of the microprobe tip and interconnection cable; AA′ and BB′ marked in Fig.1, respectively.**

**Table 3.1: Design specifications of proposed intracortical microprobes**

| Device | Electrode counts | Number of shanks | Shanks width at base ($\mu$m) | Inter-electrode distance ($\mu$m) | Interconnect width ($\mu$m) |
|---|---|---|---|---|---|
| M32-8mm | 32 | 4 | 120 | 700 | 700 |
| M32-4mm | 32 | 4 | 120 | 450 | 700 |
| M32-2mm | 32 | 4 | 120 | 200 | 700 |
| M16-2mm | 16 | 4 | 100 | 400 | 700 |
| M8-8mm | 8 | 1 | 120 | 700 | 400 |
| M8-4mm | 8 | 1 | 120 | 450 | 400 |
| M8-2mm | 8 | 1 | 120 | 200 | 400 |

cated devices. The width and interspacing of the addressing lines in the interconnection cable of the 32-site microprobes is 10 $\mu$m and it is enlarged to 20 $\mu$m in devices with 16 and 8 electrode sites. The larger feature dimensions are typically accompanied by higher fabrication yields. To scale the cross section area at the penetrating sections of the probe shanks, the width and spacing of the addressing lines is reduced to 5 $\mu$m in these regions. The dimensions of the sites are 20 $\mu$m $\times$ 20 $\mu$m in most devices while electrode sites as small as 10 $\mu$m $\times$ 10 $\mu$m have been successfully defined.

One of the most important criteria in the mechanical design of intracortical microprobes is the buckling critical force $P_c$ of the probe shanks. If the applied force during the implantation process exceeds $P_c$, it can cause permanent deformation in a metallic microprobe. For a slender beam made of a material with the elastic modulus of $E$, the buckling critical force, $P_c$, due to an axial force can be approximated by:

$$P_c = \frac{\pi^2 E w t^3}{12 l^2}, \tag{3.1}$$

where $l$, $w$, and $t$ are the beam length, width, and thickness, respectively [93]. As expected, the critical force rapidly reduces for longer and thinner beams rendering them

**Table 3.2: Elastic modulus of metals and polymers**

| Material | Elastic modulus (GPa) |
|---|---|
| Iridium (Bulk) [94] | 528 |
| Platinum (Bulk) [94] | 168 |
| Gold (Bulk) [94] | 78 |
| Gold (Electroplated) [95] | 42–52 |
| Polyimide [96] | 2.45 |
| Urethane A80 [97] | 24 MPa |

more susceptible to buckling. The elastic modulus of several metal and polymer materials is given in Table 3.2.

Based on Table 3.2, materials such as iridium (Ir) and platinum (Pt) provide higher elastic modulus values compared to gold (Au) and seem attractive candidates for the metallic reinforcement sections of the probe. Despite better mechanical characteristics, electroplating thick layers of Pt or Ir is often expensive and cumbersome. On the other hand, Au can be easily electroplated at fast rates to produce low-stress thick films. This is particularly important in the construction of long beams that can be easily deformed even if a very low stress gradient exists across the thickness of the beam. Furthermore, it is possible to release the residual stress in gold films at fairly low temperatures of around 360 – 400 °C [98]. For such reasons, Au was selected as the material of choice for the reinforcement micro-needles. Table 3.3 presents the estimated $P_c$ for 2, 4, and 8 mm microprobe shanks with 5, 15, and 25 $\mu$m-thick embedded micro-needles. In calculation of $P_c$, an average elastic modulus of 50 GPa is used for the electroplated gold and a constant cross-section of 15 $\mu$m $\times$ 100 $\mu$m is assumed for the reinforcement sections. The contribution of the polyimide outer shell can simply be ignored since the elastic modulus of the polyimide is negligible compared to that of the electroplated gold. In this work, 15 $\mu$m gold micro-needles were embedded in the microprobe shanks to provide the approximate $P_c$ values of

**Table 3.3: Estimated buckling force of the electroplated gold micro-needles**

| Buckling critical force (mN) | | | |
|---|---|---|---|
| | Thickness of reinforcement micro-needle | | |
| Shank length | 5 $\mu$m | 15 $\mu$m | 25 $\mu$m |
| 2 mm | 0.129 | 3.47 | 16.1 |
| 4 mm | 0.032 | 0.87 | 4.0 |
| 8 mm | 0.008 | 0.22 | 1.0 |

3.5, 0.9, and 0.2 mN for the 2, 4, and 8 mm long implants. These values are sufficient for the penetration into the mouse cerebral cortex if dura and pia matters are removed [99]. However, it is possible to increase the strength of micro-needles or reduce the thickness of the shanks by electroplating low stress Pt or Ir layers as the reinforcement metal.

## 3.2 Fabrication

Fig. 3.3 shows the sequence of a 3-mask fabrication process developed to produce the intracortical devices. The details of the fabrication steps and the processing conditions are presented in Appendix A.1. The microprobes were fabricated on a rigid substrate for easy handling of the devices during the fabrication period. After cleaning the substrate, a 500 nm thick molybdenum (Mo) or chromium (Cr) was deposited as the sacrificial layer and the first polyimide (PI) structural material (PI 2611, HD Microsystems) was spin-coated. Both Si and glass wafers were used as the substrate and both Mo and Cr were deposited as the sacrificial layer in different runs of the fabrication. Subsequently, the sample was annealed for 1 hr at 350 °C to cure the PI film, and then a 100 nm thin layer of gold was deposited as the electroplating seed layer.

To define the reinforcement micro-needles, an electroplating mold was created from

polyimide. After coating the seed layer with an 18 $\mu$m thick PI layer, aluminum (Al) is deposited (300 nm) and patterned in the first lithography step to create the mask layer. The PI was then etched in an RIE etching step using mixtures of $O_2$ and $CF_4$ gasses. The polymeric residues were then removed in an EKC 265 post etch residue remover and a low pressure Ar sputtering process. The clean surface of the mold is essential for the

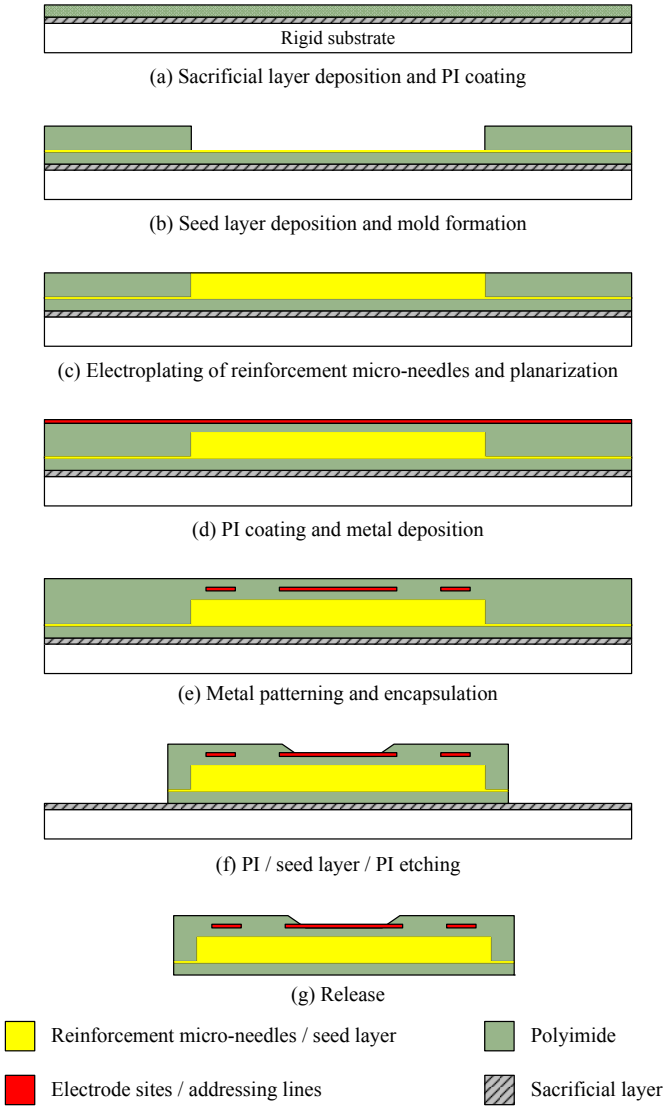


**Fig. 3.3: The fabrication sequence of the intracortical microprobes viewed at the cross-section of the device tip.**

success of the electroplating step since the polymeric residues prevent the gold from being electroplated or properly stick to the seed layer. Next, gold was electroplated inside the mold and the surface of sample was planarized to a final surface roughness of 500 nm. Fig. 3.4 shows the optical images of the electroplating mold and the planarized gold layer of a 4 mm-long microprobe. Further polishing is possible to smooth the surface of metal layer, but not necessary since the subsequent PI coating will planarize the surface filling the scratches imposed by the planarization procedure. The thickness of the reinforcement micro-needles was determined to be 15 $\mu$m.

The micro-needles were isolated from the electrodes using a third layer of PI coating. Ti (20 nm) / Au (300 nm) / Ti (20 nm) were then deposited and patterned to define the addressing lines, the electrode sites, and the bonding pads. The recording channels were

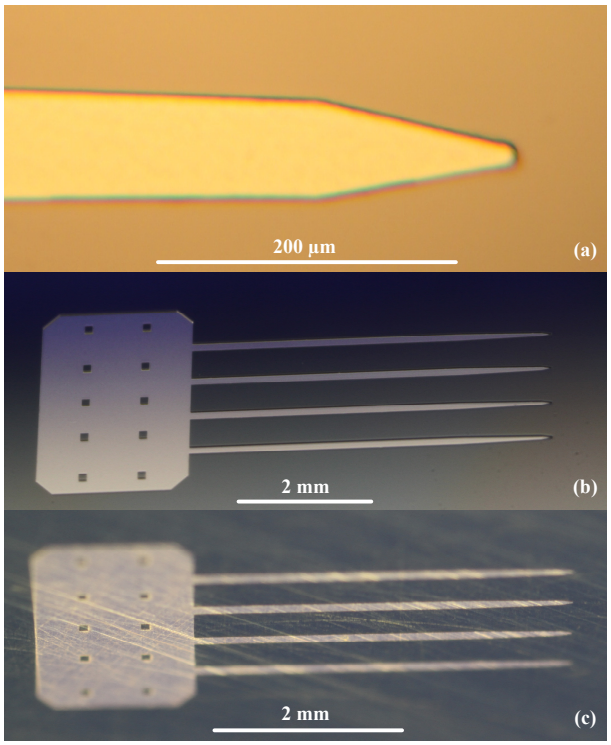


**Fig. 3.4: Optical images of (a) the electroplating mold at the tip of a micro-needle, (b) the mold of a microprobe with 4 mm long penetrating shanks, and (c) the electroplated and planarized micro-needles.**

encapsulated using a fourth layer of polyimide. Finally, the polyimide layers and the seed layer were patterned to define the shape of microprobe and to expose the electrode sites and bonding pads. The top Ti layer protects the electrode metal during the etching of the seed layer. The Ti layer covering the bonding pads and the electrode sites was later sputtered away using an Ar glow discharge. After removing the polymeric residues in EKC 265, the sacrificial layer is dissolved in the wet etchant solution (Mo: PAN at 40 °C for 24 to 48 hrs or Cr:CRE-473 Chromium Etch, Transene Company Inc., at 40 °C for 48 to 72 hrs) to release the microprobes. The fabricated devices on Si or glass wafers demonstrate identical characteristics. The material of choice employed as the sacrificial layer (Mo or Cr) also does not affect the properties of the microprobes.

Fig. 3.5 illustrates the optical images of the fabricated microprobes with 2, 4, and 8 mm-long probe shanks. The devices offer integrated flexible interconnection cables with

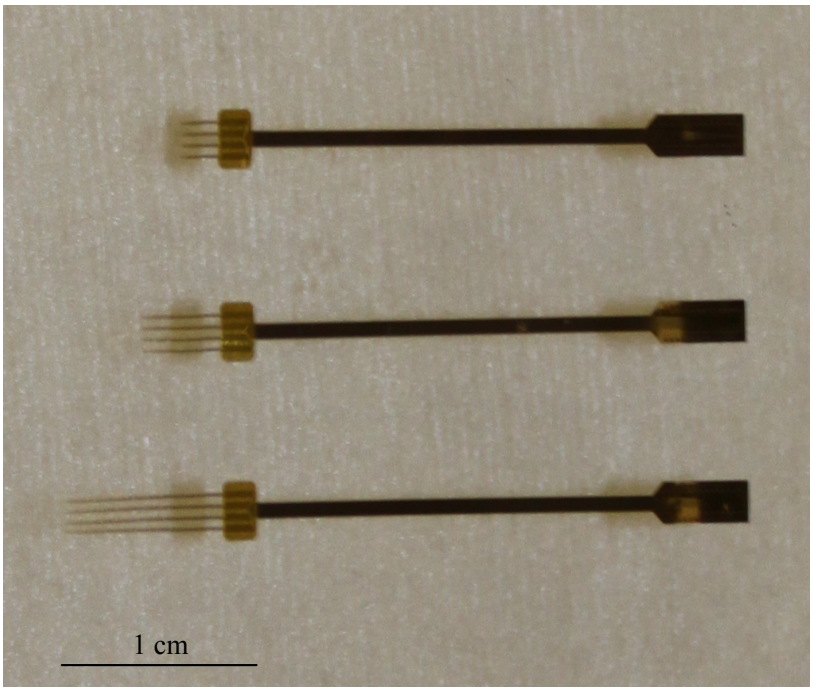


**Fig. 3.5: Optical images of released 32-site intracortical microprobes with 2, 4, and 8 mm-long shanks.**

lengths exceeding 2 cm and large bonding pads. Fig. 3.6 presents the magnified images of the probe tip, the shanks, and a recording site. As shown in Fig 3.6(b), the centre to centre distance of the electrode sites in a 4 mm-long design is 450 $\mu$m, although it can be easily tailored in the second and third lithography steps. The surface roughness of the electrode sites is below 2 nm as confirmed by the Veeco WYKO NT1100 optical profiler. Indeed,

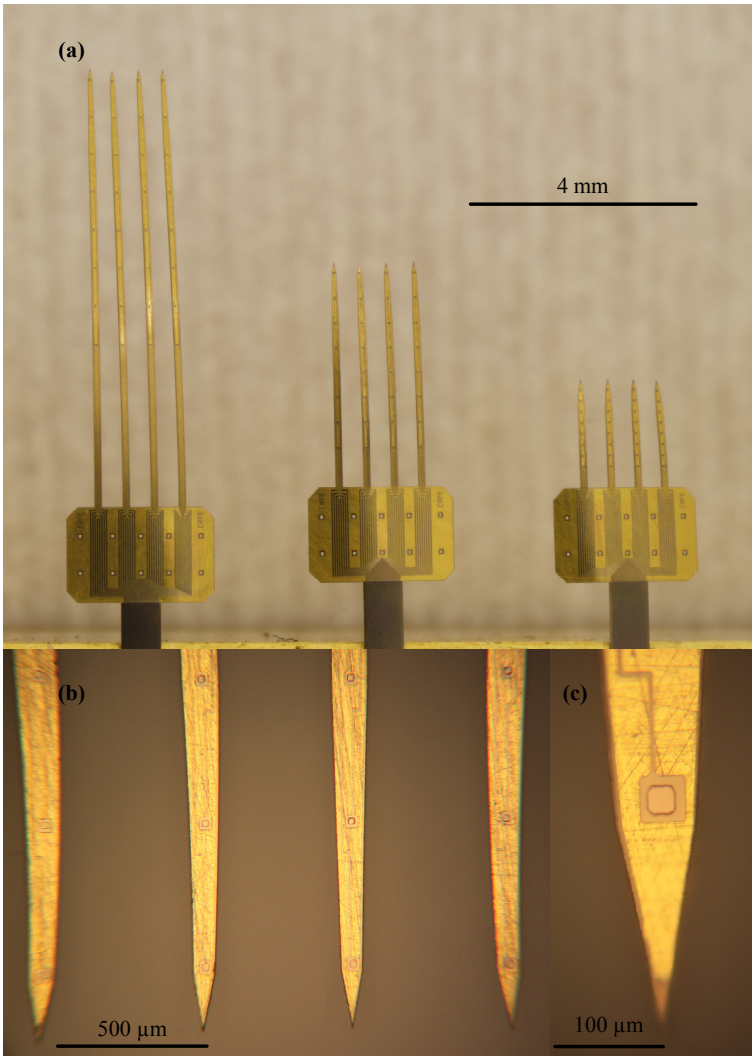


**Fig. 3.6: Optical images of (a) the implants tips, (b) probe shanks of a 4 mm-long design illustrating 3 rows of electrode sites, and (c) an electrode site.**

the surface defects and scratches of the gold micro-needles have not been transferred to the electrodes metal layer and have been planarized by the PI intermediate layer.

Fig. 3.7 illustrates the SEM image of a 2 and 4 mm-long intracortical microprobe. Arrays of small holes were produced in the base section connecting the shanks and the

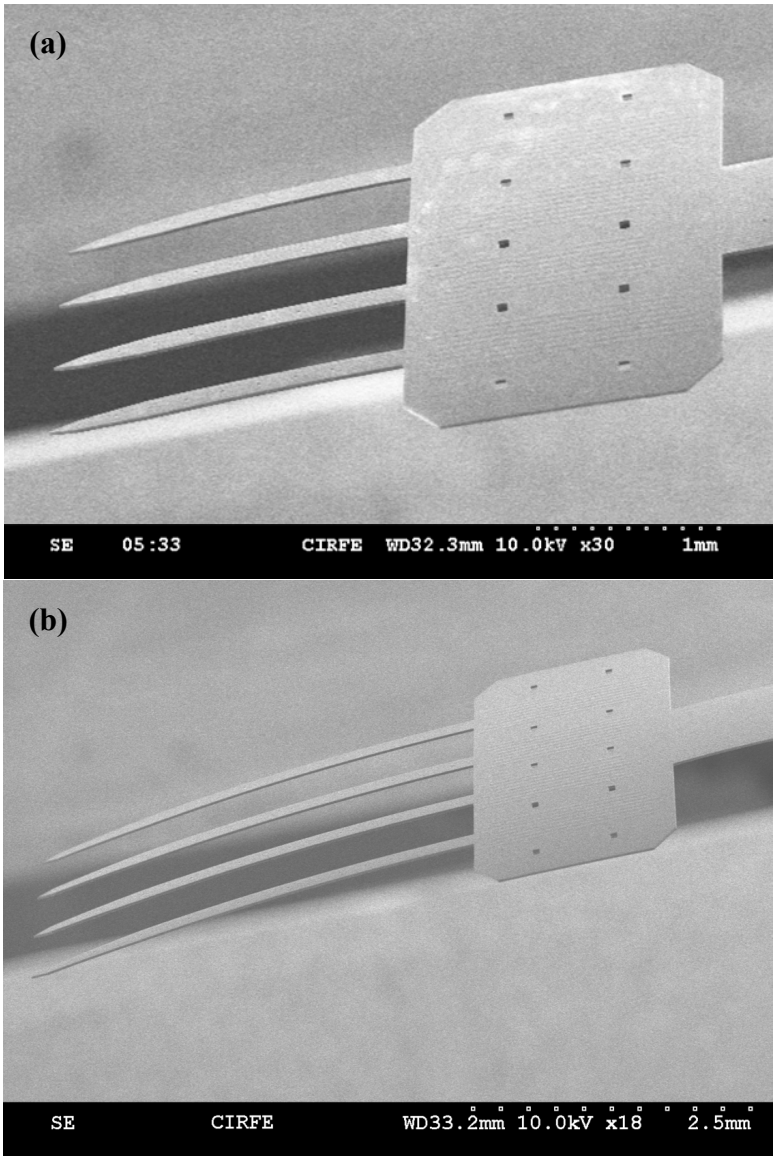


**Fig. 3.7: SEM images of intracortical microprobes with 2 and 4 mm long penetrating shanks.**

interconnection cable to reduce the duration of the release process. Fig. 3.8(a) and (b) show higher magnification images of the probe shanks and an electrode site located at the tip of a shank. No polyimide residues were observed on the sidewalls of the probes. Moreover, the surfaces of the PI insulating layer or the electrode sites have not been

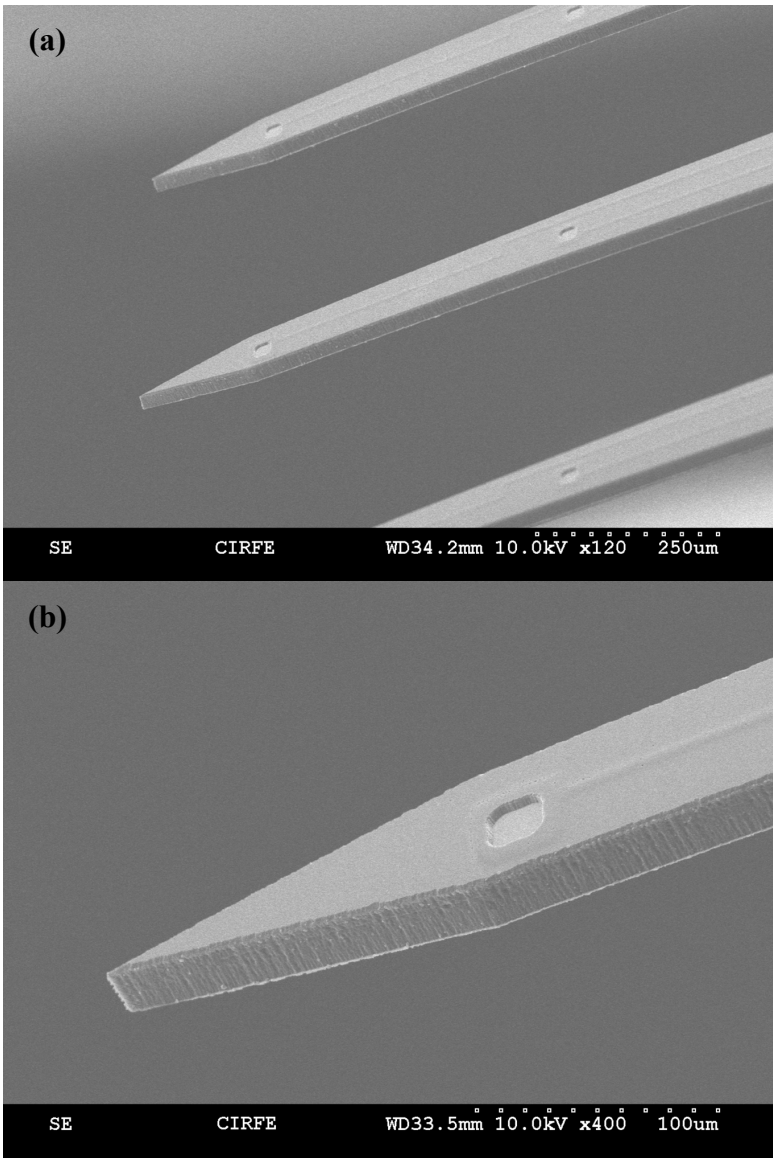


**Fig. 3.8: Close-up SEM images of a probe shank and an electrode site.**

damaged during the PI etching or the release of the device. Indeed, the $O_2$ / $CF_4$ plasma RIE process was optimized to etch the PI layers leaving minimal amount of polymeric residues which are soluble in IPA or EKC solutions.

To facilitate the electrical characterization of the fabricated devices, the microprobes were connected to commercially available IDC DIP plug connectors using custom made flexible adaptor boards. The adaptor boards were fabricated on Kapton sheets (500HN from DuPont) with a thickness of 127 $\mu$m using a 50 nm Cr / 1 $\mu$m Au bilayer as the addressing lines. The adaptor was mounted on the IDC connector and the electrical connections were made by silver epoxy. The electrical joints were then covered with nonconductive epoxy to increase the mechanical strength of the connection points. To connect the bonding pads of the microprobe to the adaptor circuit, silver epoxy can be used to create elevated contact points on either the pads of the connector or the microprobe. Fig. 3.9(a) and (b) show the

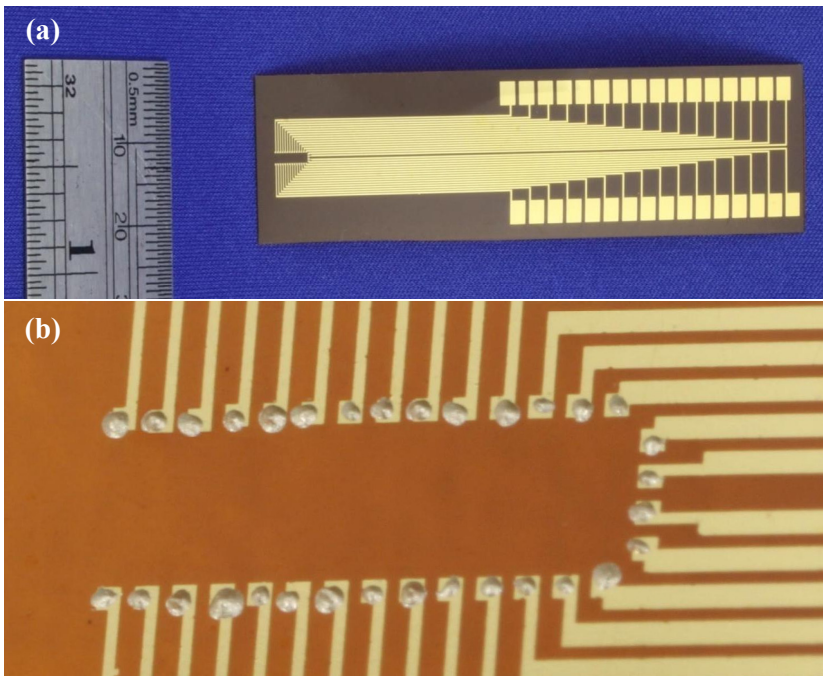


**Fig. 3.9: Images of (a) the flexible adaptor board and (b) the silver epoxy covered contact points.**

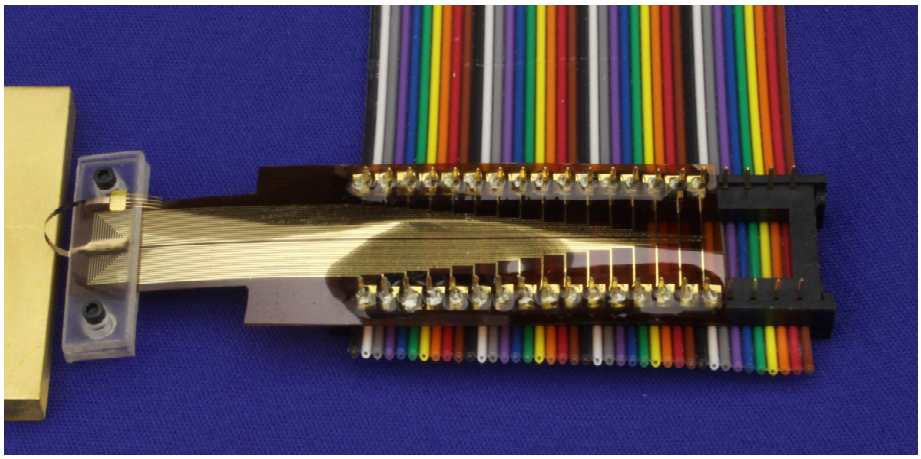

**Fig. 3.10: Photograph of a 32-site microprobe attached to a 40 pin IDC connector and a ribbon cable.**

optical image of the adaptor board and the close-up image of the adaptor's contact points covered with silver epoxy. The microprobes were then placed over the adaptor and the electrical connection between the contact pads was made by a mechanical force applied by 2 rectangular solid sheets pressed against each other. Fig. 3.10 presents the image of a 4 mm long microprobe integrated with a 40 pin IDC connector. A ribbon cable is attached to the connector for easy access to the recording channels.

## 3.3 Impedance Characteristics

The overall impedance of a neural electrode consists of the impedance of the electrode-electrolyte interface and the parasitic elements introduced by the addressing line. In this section, the electrical characteristics of the interconnection cable and the custom made connector are discussed. The experimental setup used for measuring the impedance is described and the obtained results for electrodes with Au and Ir stimulation / recording sites are presented.

### 3.3.1 Addressing Lines

The electrode sites are connected to the external circuitry through the integrated interconnection lines and the external cables. These components add parasitic series resistances and parallel capacitances to the recording channels. The channel to ground and channel to channel capacitances can be ignored in practical applications. These parasitic elements are estimated to be less than 1 pF for a 10 $\mu$m-wide 3 cm-long interconnection cable encapsulated by a 4 $\mu$m polyimide layer. These capacitance values translate into parallel parasitic impedances in the M$\Omega$-range at frequencies above 1 MHz where the channel impedance is below 10 k$\Omega$. On the other hand, the series DC resistance of the addressing lines may significantly increase the impedance of the channel and severely affect the signal to noise ratio. In this work, the addressing lines are made of gold to reduce the parasitic resistance to below 1 k$\Omega$. The measured resistance values ranges from 200 $\Omega$ to 260 $\Omega$ close to the theoretical value of the 220 $\Omega$ expected for a 300 nm-thick 3 cm-long conductor. The resistances of the flexible adaptor and cables are also in the range of 90 to 125 $\Omega$ significantly below the channel impedances.

### 3.3.2 Experimental Setup

The impedance of an electrode is commonly measured using a tri-electrode measurement setup illustrated in Fig. 3.11. In a two electrode setup, when the voltage of an electrode of interest is measured against a reference electrode, a voltage drop equal to $I \cdot R_s$ is included in the measured voltage. The $I$ is the electrode's current and $R_s$ is the resistance of the solution due to the ionic mass transfer. In a tri-electrode setup, the current is passed between the working electrode and a counter electrode. The voltage of the working electrode is monitored relative to a separate reference electrode that is placed near the working electrode. Therefore, the voltage of the working electrode remains constant and

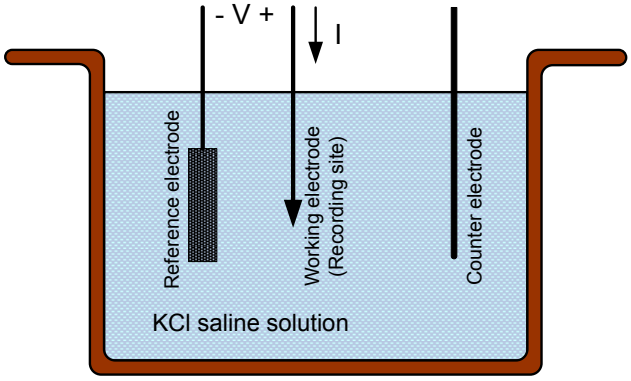


**Fig. 3.11: Schematic of a tri-electrode measurement setup.**

equal to the open circuit value. The tri-electrode setup employed in this study consists of an Ag-AgCl reference electrode and a platinum counter electrode. The input signal is applied between the electrode sites and the counter electrode. The resulting current and voltage between the electrode sites and electrolyte were recorded against the reference electrode and employed to calculate the site impedance.

### 3.3.3 Impedance of Au electrodes

The impedance of the recording channels was measured in a 1M KCl saline solution. Fig. 3.12 shows the impedance magnitude and phase of a representative channel over the 10 Hz – 300 kHz frequency range. The DC resistance of the addressing lines and the electrolyte impedance from the reference to counter electrode was found to be negligible compared to the channel impedance even at 300 kHz. Therefore, the recorded impedances accurately represent the impedance of the electrode sites particularly below 100 kHz.

The impedance of an electrode site is comprised of two distinct parallel components modeling the faradic charge transfer process to the solution and the charge / discharge of electrode-electrolyte double layer. At low frequencies, the impedance associated with

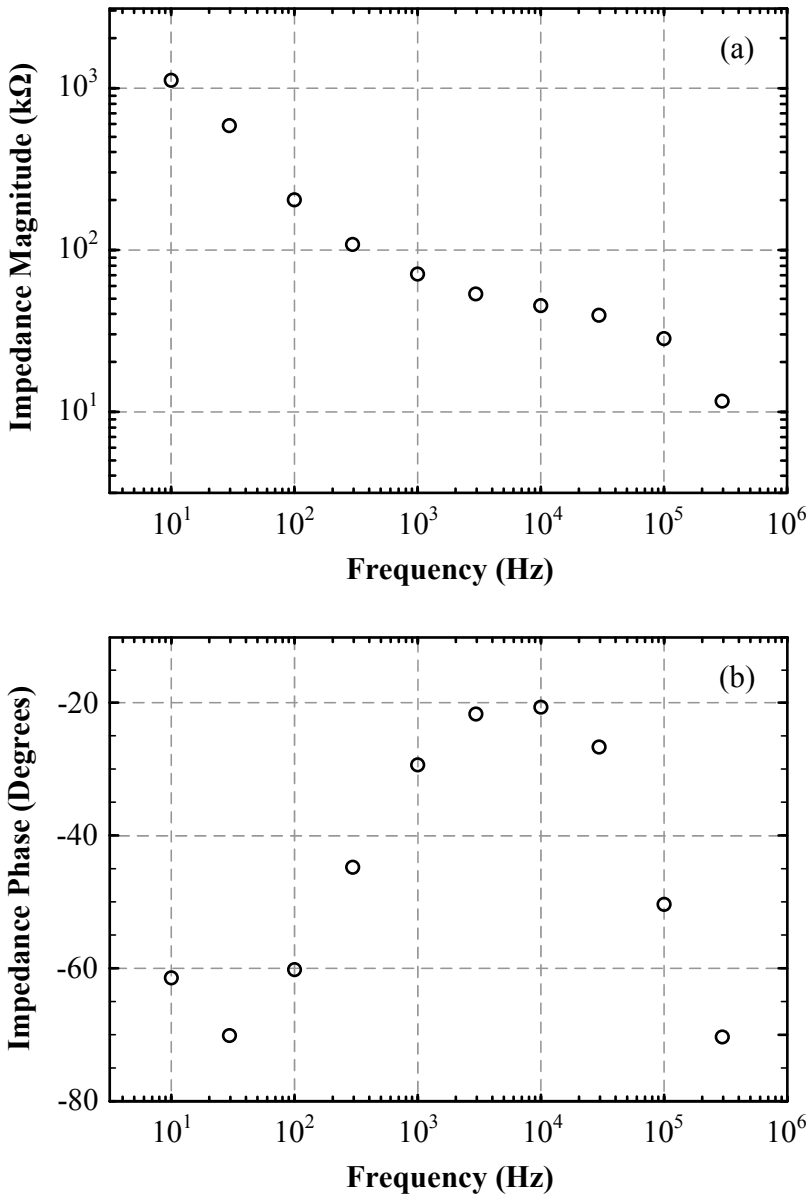


**Fig. 3.12: (a) Impedance magnitude and (b) phase of a 20 $\mu$m $\times$ 20 $\mu$m recording channel.**

the faradic process is dominant while at high frequencies, the double layer capacitance provides a more effective current path to the solution. As expected, the phase lag of the site impedance rapidly rises above 30 kHz. In this frequency range, the impedance of

the electrodes is determined by the double layer capacitance and exhibits more capacitive behaviour as the frequency increases. A key advantage of the fabricated devices is the low impedance of the channels particularly at high frequencies. Due to the utilization of gold as the addressing lines, the impedance of the electrodes is not limited by the parasitic series resistance. As a result, the high frequency features of the neurons' action potential can be recorded with an enhanced signal to noise ratio.

### 3.3.4 Impedance of Ir electrodes

The impedances of neural microelectrodes are mainly determined by the electrodes' dimensions, the sites material, and the properties of the biological environment such as the chemical compound and ionic concentration. The dimensions of the electrodes for recording the single neuron's activities are preferred to be in the range of 10 – 20 $\mu$m to avoid measuring the average responses of the adjacent cells [7]. However, electrodes with such dimensions demonstrate high impedances that undermine the signal to noise ratio of the recorded signal. Materials such as platinum black [49], iridium [100], and iridium oxide [101] have been widely used to enhance the capacity of the charge delivery and as a result to reduce the impedance of the electrode. To improve the electrical characteristics of the channels, a 200 nm thick Ir layer was electro-plated over the gold electrode sites with details explained in chapter 4. Fig. 3.13(a) illustrates the optical image of a probe tip with adjacent gold and Ir-plated electrode sites. The Ir-plated electrode site appears black due to the increased surface roughness of the electrode.

Fig. 3.13(b) and (c) present the impedance magnitude and phase of the Ir-plated electrodes over the 10 Hz – 300 kHz frequency range in a 1M KCl saline solution. As expected, the impedances of Ir electrodes are substantially less than the corresponding values for gold electrodes. The electrode impedances demonstrate enhanced capacitive

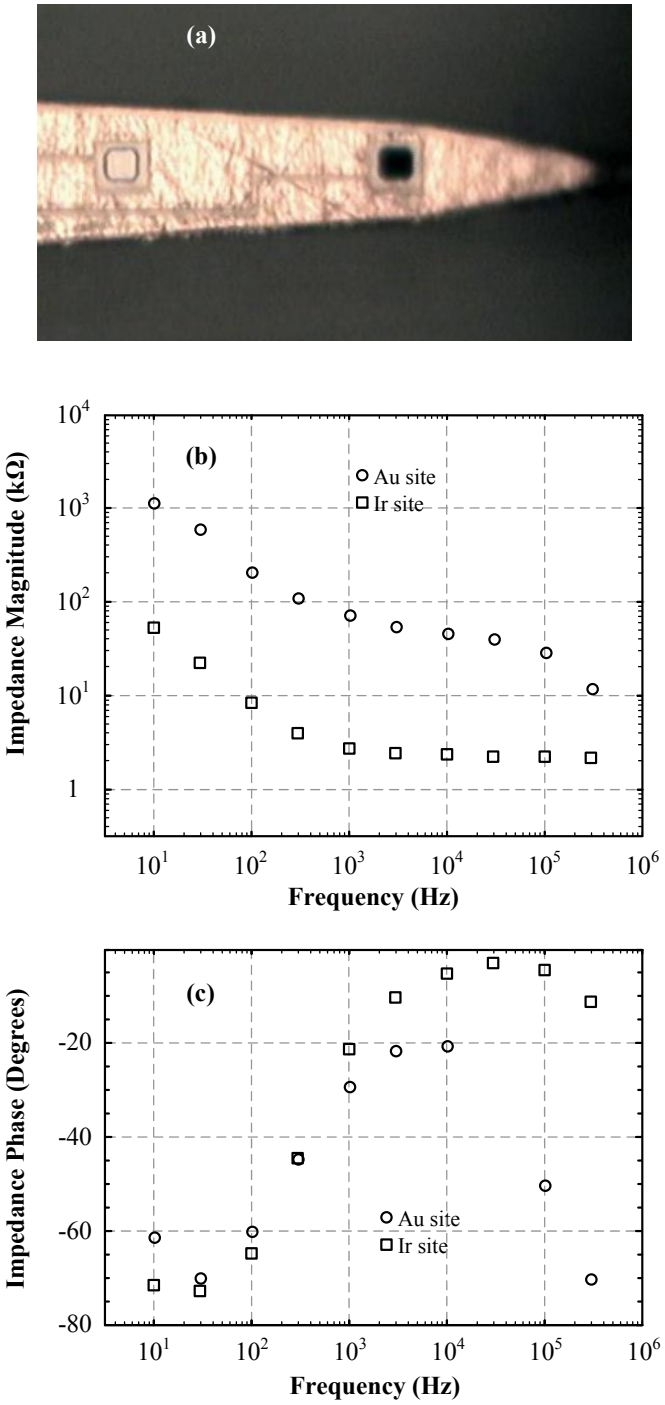


**Fig. 3.13: (a) Optical images, (b) impedance magnitude, and (c) phase of Au and Ir-plated electrode sites.**

characteristics below 100 Hz due to the increased surface roughness, and an enhanced resistive behaviour above 1 kHz as a result of the higher charge delivery capacity of the Ir layer.

## 3.4 Impedance Stability

The electrical characteristics of neural microprobes drift over time when the device is immersed in an ionic or biological environment. This characteristics drift is associated with the corrosion of the electrode metal and the erosion of the structural layer [28]. Such reactions deteriorate the performance of the microprobes by increasing the electrodes impedance and decreasing the isolation between the channels particularly when the electrode is used for stimulation. In this study, the impedance behaviour of Au and Ir electrodes in saline and strong acidic solutions was investigated. The Au electrode sites were subjected to a prolonged stress test with 100 million cycles of square pulses. A 10 kHz square pulse wave with a 2 V peak-to-peak amplitude (+1 V to -1 V) and a 50% duty cycle was applied between the channel and the reference electrode in a 1 M HCl solution. The measured impedance magnitude and phase of an electrode sites before and after the pulse test experiment are illustrated in Fig. 3.14.

The deviation in the impedance of the electrodes was smaller than 50% of the initial values. The measured impedances fall rapidly during the first 10 million cycles and then remain constant for the rest of the experiment. A possible explanation for this behavior is the electro-chemical cleaning of the electrode surface from polymeric residues that remained after the RIE etching of the top polyimide layer. These residues reduce the effective contact area of the electrode site and consequently the rate of charge transfer to the solution. Upon removal of this layer, the surface area of the electrode is enhanced resulting in a lower impedance with increased capacitive characteristics as observed in Fig. 3.14(b). This

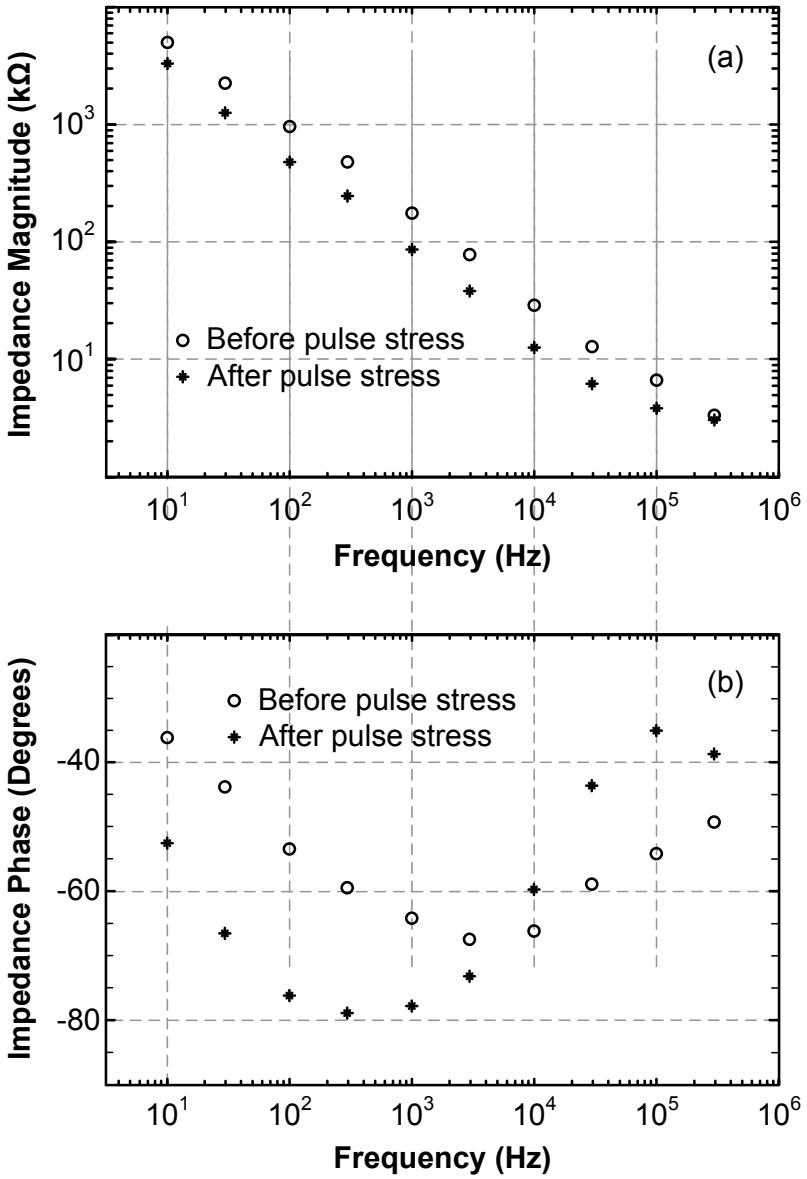


**Fig. 3.14: (a) Impedance magnitude and (b) phase of an Au electrode before and after the pulse test in 1 M HCl.**

speculation is also supported by a larger impedance deviation measured for microprobes which were not rinsed in the EKC solution after the RIE etching step. Furthermore, no signs of surface damage or metal delamination were detected in microprobes after the pulse test (see Fig. 3.16).

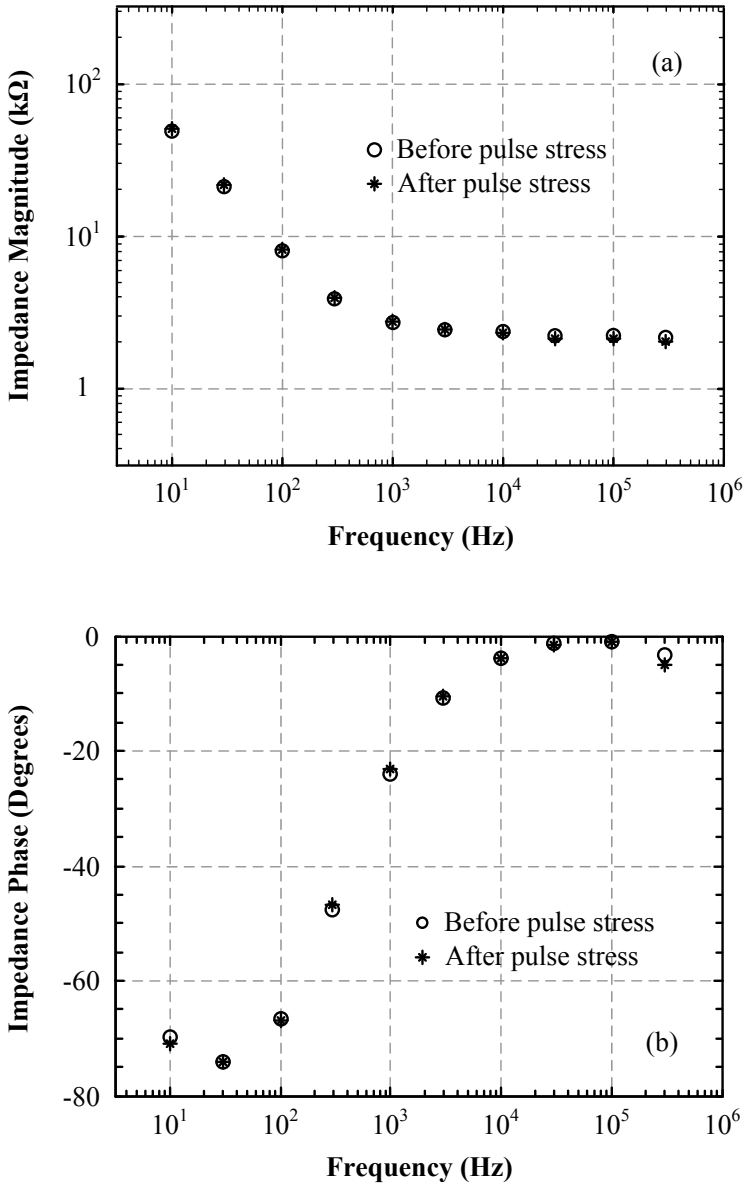


**Fig. 3.15: (a) Impedance magnitude and (b) phase of an Ir electrode before and after the pulse test in 1 M HCl.**

Fig. 3.15 depicts the impedance magnitudes and phases of Ir-plated electrodes after a 100 million cycle pulse stress test. The test was also performed in a 1 M HCl solution employing a square pulse wave with a 2 V peak-to-peak amplitude. Other parameters of the stress pulse were kept similar to the previous stability experiment. Stable impedance

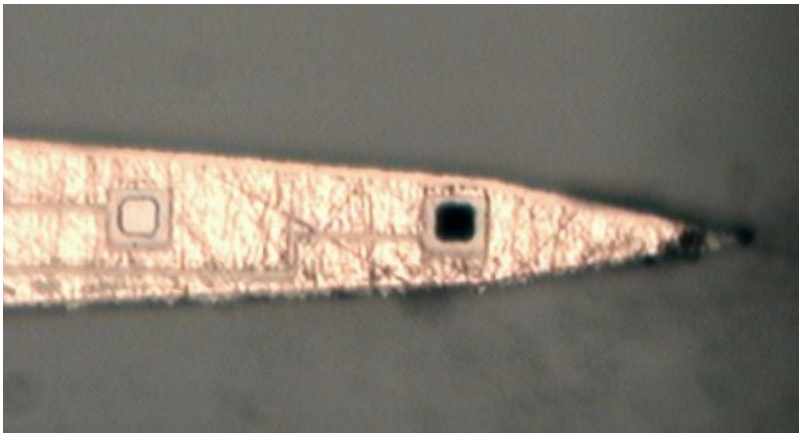

**Fig. 3.16: The optical images of an electrode site after the pulse test.**

characteristics were observed over the course of the experiment. The Optical image of an electrode site exposed to the pulse stress test is shown in Fig. 3.16. No sign of degradation in the gold or electroplated Ir layer was observed. Indeed, the fabricated microprobes demonstrate stable impedance characteristics and can be potentially employed in chronic applications.

## 3.5 In-vitro Recording

A 4mm-long single shank microelectrode was employed to record the neural activities of the whole hippocampus of a 7 day old postnatal C57BL/6 mouse. The hippocampus extraction method and the configuration of the perfusion chamber will be briefly described in chapter 4 while a comprehensive discussion on the methodology and experimental setup has been published in [102]. The microprobe was positioned on a micromanipulation stage and advanced into the tissue to place the electrode site approximately in the middle of the hippocampus. Moreover, the microprobe was inserted into and retrieved from several locations in the tissue without bending or mechanical damage. However, for a solid

confirmation additional experiments on thicker neural tissues are necessary.

The neural signals from the electrodes were first amplified using a custom made circuitry and captured using a HP DSO3202A digital oscilloscope with a 10 kHz sampling rate. The amplifier circuit employs an AMP02 instrumentation amplifier (Analog Devices) with the voltage gain set to 500 V/V. To improve the signal to noise ratio, a 10 pole low pass Chebyshev's filter with a cut-off frequency of 500 Hz was applied to the recorded signal in Matlab. Fig. 3.17 illustrates the periodic field potential activity recorded from a representative electrode site. The in-vitro experiments confirm the capability of the fabricated microprobes to record the neural activities. To enhance the signal to noise ratio of the recorded signal an improved packaging design, higher-gain amplifier, and shielded interconnection cables are necessary.

## 3.6 Summary

The design, fabrication, and characteristics of a novel generation of multisite flexible intracortical microprobes with improved structural design were described in this chapter. A 3-mask fabrication process was developed to produce the 32 channel microprobes integrated

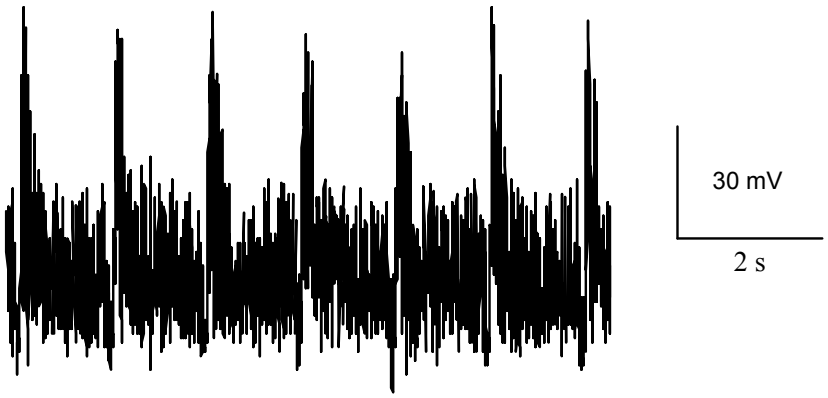


**Fig. 3.17: Recorded periodic field activities in a C57BL/6 mouse hippocampus.**

with 2 cm-long flexible interconnection cables. The electrode sites are located on 4 parallel shanks mechanically reinforced by embedded 15 $\mu$m-thick gold micro-needles. The microprobes are non-breakable and rigid enough for penetration into the tissue while connected to the external circuitry with an extremely flexible cable. To enhance the microprobe functionality, the impedances of the recording channels were reduced by electroplating Ir over the gold electrode sites. The impedance characteristics and stability of the electrodes were studied in acidic and saline solutions. The stable electrical characteristics of both iridium and gold electrodes were demonstrated over the courses of prolonged pulse stress tests for 100 million cycles. The functionality of the fabricated microprobes was confirmed by successful recording of the periodic field potential activity from an intact mouse hippocampus. Table 3.4 compares the properties of the proposed intracortical microprobes to those reported in literature.

**Table 3.4: Comparison of the intracortical microprobes' properties**

| Microprobe | Multisite shanks | 3D array | Integrated flexible cable | Rigid for penetration | Integrated electronics | Breakable structure |
|---|---|---|---|---|---|---|
| Michigan [7, 64] | Yes | Yes | Yes [a] | Yes | Yes | Yes |
| DRIE [71, 74] | Yes | Yes | No | Yes | Possible | Yes |
| Utah [76, 77] | No | No | No | Yes | No | No |
| Metallic arrays [30, 42] | No | No | No | Yes | No | No |
| Polyimide-based [34, 81] | Yes | Possible | Yes | No | No | No |
| Metal Shank [41, 43] | Yes | Possible | No | Yes | No | No |
| Proposed microprobes | Yes | Possible | Yes | Yes | No | No |

[a] Only out-of-plane flexibility.

# Chapter 4

# Multisite 3D Microprobes for Deep Brain Stimulation and Recording

Deep Brain Stimulation (DBS) has been accepted as an effective treatment for advanced Parkinson's disease [11], epilepsy [103, 104], and dystonia [12]. DBS is an alternative method for patients suffering from the complications of long-term levodopa therapy [105] and favoured over non-reversible destructive lesioning. DBS is performed by a multisite electrode connected to a pulse generator implanted in the chest. The electrical connection between the components is provided by a subdermally routed interconnection cable.

The DBS settings such as the polarity of the electrode sites, current amplitude, pulse width, and pulse frequency are adjusted to improve the efficacy and reduce the adverse effects of the treatment [106]. The commonly employed stimulation parameters are in the wide range of 1 to 5 V pulse amplitude, 60 to 200 $\mu$s pulse width, and 120 to 180 Hz stimulus frequency determined mainly by trial and error [107]. The trial and error approach is mostly effective in the treatment of disorders such as tremor that respond quickly to the stimulation. In cases such as dystonia and obsessive-compulsive disorder where the benefits of stimulation may appear weeks later, it is crucial to understand the therapeutic mechanism of DBS [108].

Despite the fast growth in clinical applications of DBS, the mechanism of the action still

remains unclear [109]. To understand the effect of DBS on targeted neurons, long-term stimulation and recording of the neural activity from a large number of closely located neurons are necessary. Hence, chronically implantable microelectrode arrays must be developed to stimulate individual cells and monitor their response. A large number and high density of electrode sites are demanded, while the size of the device must be scaled to minimize the volume of the displaced tissue and thus, the amount of damage introduced by the implant penetration. Moreover, to enhance the efficacy and minimize the adverse effects of the DBS treatment, the microprobe must be able to control the spatial distribution of the charge injected into the tissue. Such requirements were described in chapter 1 and a comprehensive review of the characteristics, designs and fabrication methods of currently available microprobes was provided in chapter 2. The reported microprobes do not satisfy many of the requirements such as the structural flexibility, recording capability, and 3D configuration.

In this doctoral study, a novel approach was developed to produce 3D microprobes with independent stimulation and recording electrodes around the probe shaft. Polyimide-based planar devices fabricated by MEMS processing techniques were assembled on a flexible support structure to construct the implants [110, 111]. Therefore, the dimensions and spatial distribution of the electrode sites are precisely controlled by lithography. Furthermore, flexible interconnection cables were integrated with these devices to facilitate their connections to external circuitry. The fabrication method and characteristics of the proposed DBS microprobes are presented in this chapter.

## 4.1 Structure and Design

The 3D structure of the proposed DBS microprobes along with the cross-section schematics of the probe tip are illustrated in Fig. 4.1. These implants offer independent electrodes

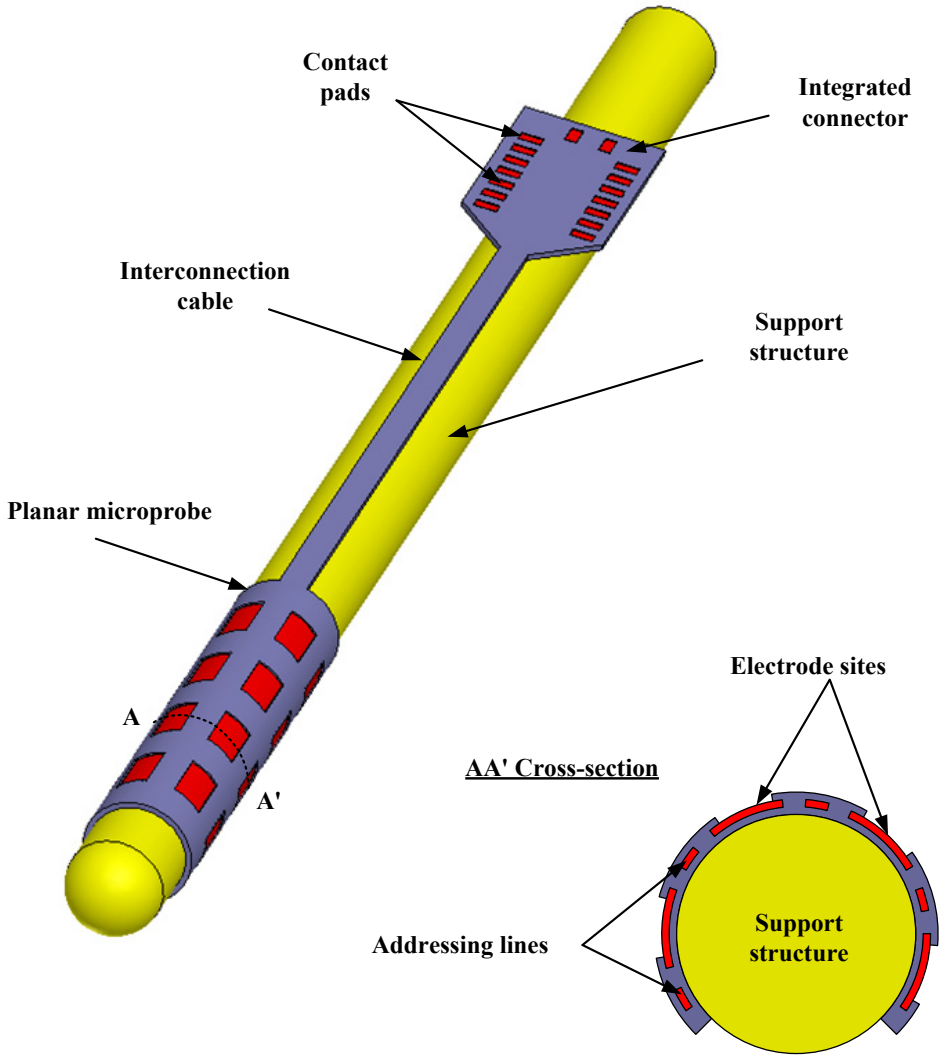


**Fig. 4.1: 3D schematic and the tip cross-section of a proposed DBS microprobe.**

around the probe shaft with dimensions suitable for stimulation or recording. The main component of these implants is a flexible planar microprobe wrapped around or assembled on a cylindrical support structure. Fig. 4.2 shows the 3D schematic of a planar thin film probe along with the device cross-section at the tip. The planar microprobes consist of three major components; namely, the probe tip, the interconnection cable, and the integrated connector. At the tip of the planar probe, an array of 16 stimulation and 16

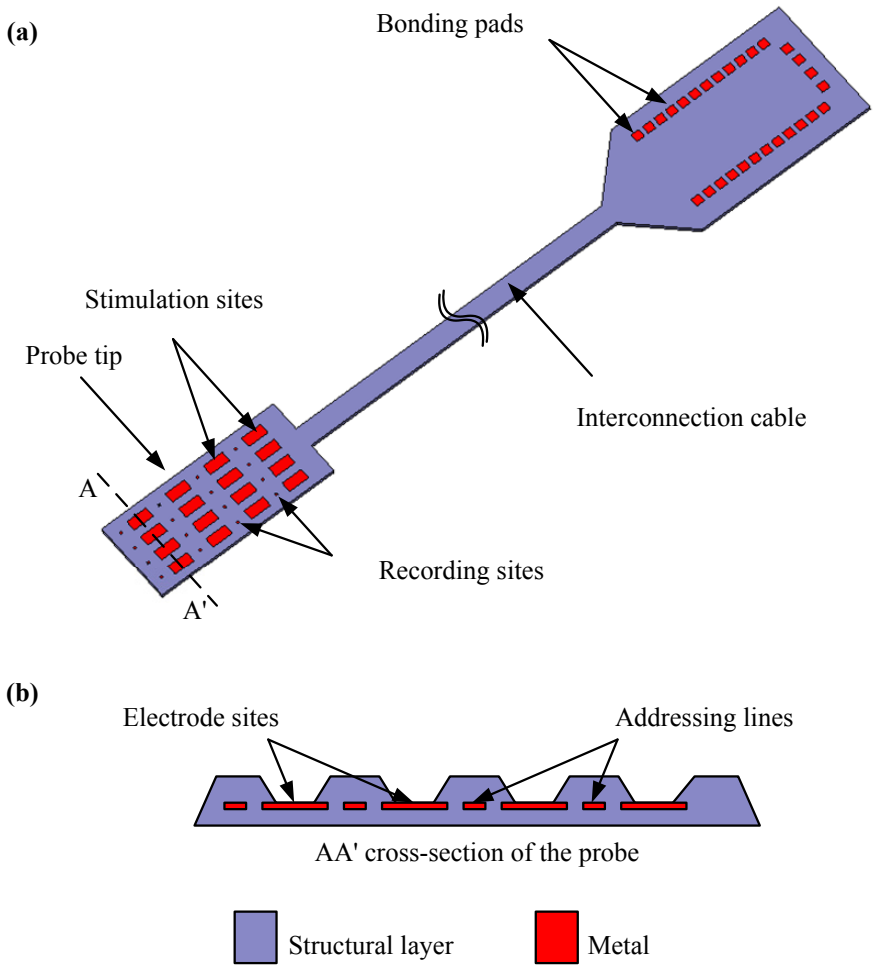


**Fig. 4.2: (a) 3D schematic of a planar microprobe and (b) the cross-section of the probe tip.**

recording electrodes is fabricated. The dimensions of the stimulation and recording sites are 100 $\mu$m $\times$ 1.5 mm and 20 $\mu$m $\times$ 20 $\mu$m, respectively. The length of the stimulation sites was set equal to those of the Medtronic's DBS leads to provide a large stimulation capability. Concurrently, it is possible to monitor the single neuron's activities using the embedded recording sites with micrometre-scale dimensions.

## 4.2 Methodology and Approach

The deposition, lithography and etching must be carried out over a 3D surface if conventional approaches are employed for the fabrication of the proposed DBS microprobes. Although one can use techniques such as 3D lithography or laser micromachining, the resolution and associated yields for such processes are limited. The small dimensions of the device also add to the complexity of these methods. To avoid facing such difficulties, the planar microprobes are fabricated conventionally and then bonded to a support structure using polyurethane or thermoplastic adhesive layers. Here, the fabrication of the planar thin film probes is discussed and then the details of the micro-assembly method is described.

### 4.2.1 Fabrication of Thin Film Microprobes

The fabrication sequence of the planar microprobes is shown in Fig. 4.3. The details of the fabrication steps and the processing conditions are presented in Appendix A.2. The 2-mask process begins with the deposition of Cr as the sacrificial layer on a rigid substrate such as a silicon or glass wafer. The rigidity of the substrate facilitates sample manipulation and handling throughout the fabrication process. Both Si and glass wafers were used as the substrate in different runs of the fabrication. As the first structural layer, polyimide (PI2611 HD Microsystems) is spin coated and cured with a final thickness of 4 $\mu$m. Subsequently, a 250 nm gold layer is E-beam deposited and patterned to form the electrode sites, addressing lines, and bonding pads. Then, the second polyimide layer (4 $\mu$m) encapsulates the gold patterns. To provide access to the bonding pads and the electrode sites, an oxygen plasma dry etching step is employed. The etching of the top polyimide structural layer does not affect the gold patterns and hence it is continued to define the shape of the microprobe as well. Finally, the sacrificial layer is removed in a

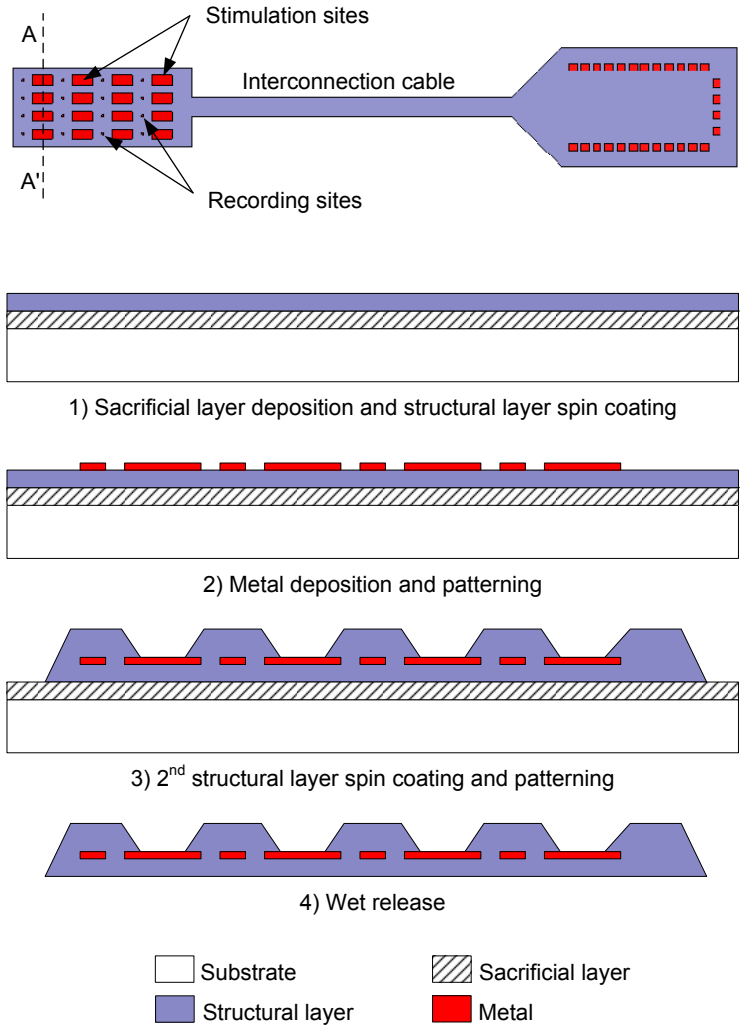


**Fig. 4.3: The fabrication sequence of planar microprobes.**

selective wet etchant solution to release the microprobes. The fabricated devices on Si or glass wafers demonstrate identical characteristics.

The photograph of a fabricated microprobe and close-up images of the stimulation and recording sites are shown in Fig. 4.4. The devices provide 16 stimulation and 16 recording channels integrated with a 2 cm long interconnection cable. Although no adhesion layer is employed, the gold metal layer is observed to have a proper adhesion to the bottom and top polyimide films. To improve the adhesion of the gold to the polyimide structural layer,

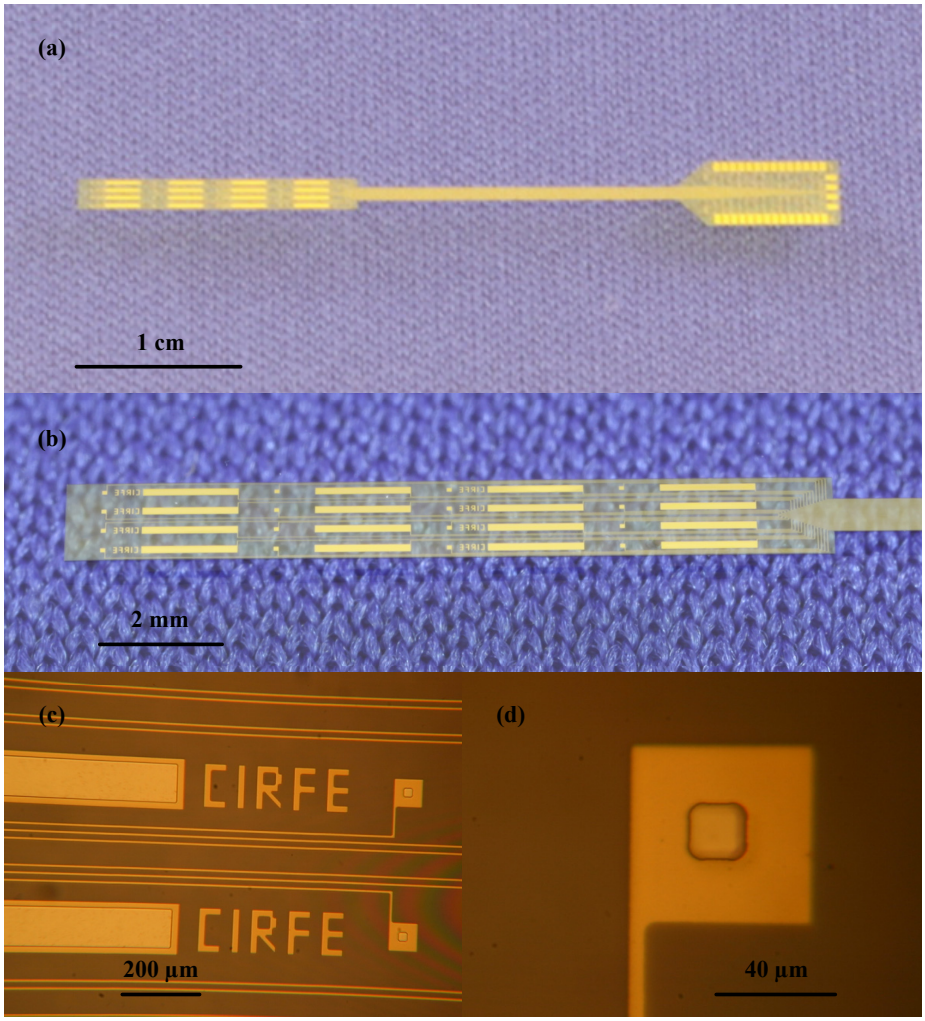


**Fig. 4.4: Optical images of (a) a planar device, (b) the microprobe tip, (c) a stimulation site, and (d) a recording site.**

an oxygen plasma surface treatment process was utilized. Hence, the application of the adhesion layer was avoided to achieve the highest degree of biocompatibility.

The surface morphology of the stimulation and recording sites were studied using SEM. Indeed, no cracks, defect points, or delamination were detected on the planar probes (see Fig. 4.5). The surface roughness of the polyimide and gold layers were also less than 2 nm, as confirmed by a Veeco Dektak 8 surface profiler.

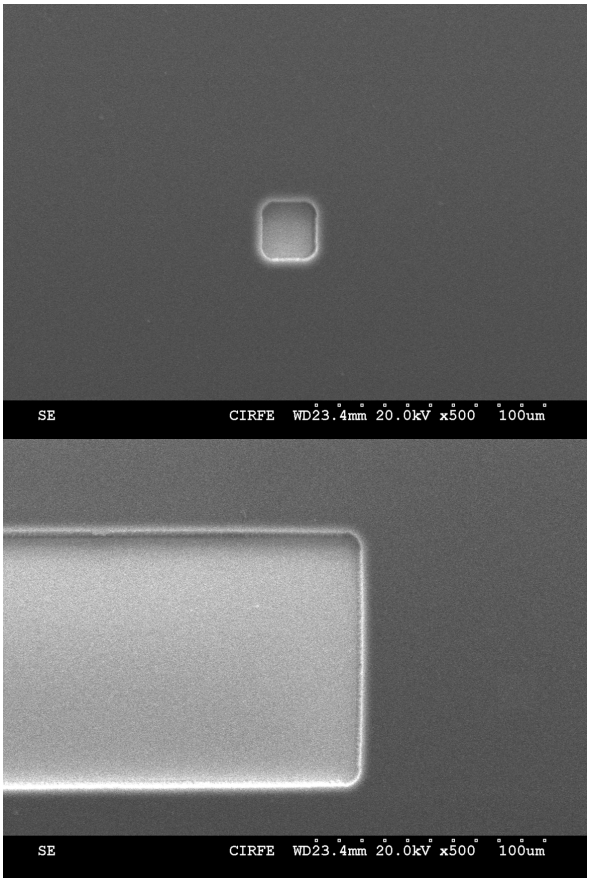


**Fig. 4.5: The close-up SEM image of (top) a recording and (bottom) a stimulation site.**

### 4.2.2 Micro-Assembly

Polyurethane A80 was used as the support structure or the shaft of the DBS microprobes. Polyurethane is a rubber compound that solidifies at room temperature after mixing the two liquid constituents. The high degree of biocompatibility and the robust mechanical properties are a strong motivation for the application of polyurethane as the shaft of the DBS probes. In fact, the commercially available DBS probes by Medtronic use polyurethane as the outer jacket. Here, Poly 75-79 from Polytech was injected inside a

cylindrical mold with a diameter of 700 $\mu$m. The mold is then heated to 50C for 24 hrs to cure the polyurethane. To facilitate the release process, the faces of the mold were coated with a thin layer of release agent, Pol-Ease 2300, prior to the injection of the polyurethane.

The planar devices were secured over the pre-made shafts using a thermoplastic film (3M thermo-bond film 406). The thermoplastic film is an adhesive layer (80 $\mu$m) that melts at elevated temperatures ($\sim$ 120 °C) and bonds the planar devices to the polyurethane shaft. The adhesive layer was cut to the size of the planar microprobe tip using a laser micromachining equipment with $\pm$ 2 $\mu$m precession. To fold a planar probe around a polyurethane shaft, a planar device was placed in the middle of a two piece cylindrical mold. Next, the thermoplastic layer and shaft were aligned to the middle of the probe with less than $\pm$ 5 $\mu$m positioning error and pushed inside the first piece of the mold. Prior to this step, the cured DBS shafts were rinsed in IPA and dehydrated at 100 °C for 30 min. The second mold piece is then closed folding the layers over the shaft. After annealing the device at 120 °C for 2hrs, the mold is opened and the device is released.

Although this method is capable of producing 3D microprobes, the yield of the fabrication is low since in the annealing step the thermoplastic layer may reflow and cover the electrode sites. The biocompatibility of thermoplastic layer is another concern particularly for implants used in chronic applications. To enhance the yield of the fabrication and the biocompatibility of the device, a thin layer of polyurethane was later employed to bond the planar probe to the support structure.

To produce a thin layer of polyurethane over the support structure, the shafts were immersed in freshly mixed polyurethane and kept in a vertical orientation to remove the excess liquid. This second layer of polyurethane was partially cured for 6 hrs resulting in a total sample diameter of 740 $\mu$m. Therefore, the partially cured polyurethane layer was as thin as 20 $\mu$m.

Fig. 4.6 and Fig. 4.7 illustrate the optical and SEM images of a completed DBS

microprobe. The fabricated devices provide 2 cm-long interconnection cables and large bonding pads that facilitate the connection of these devices to an external circuitry. The probe offers 16 stimulation and 16 recording sites placed at the tip of the microprobe. The stimulation sites are 100 $\mu$m $\times$ 1.5 mm and the recording sites measure 20 $\mu$m $\times$ 20 $\mu$m. The tip of the probe measures 1.2 mm in length and 750 $\mu$m in diameter. As a result, a 3-fold reduction in the volume of the device is achieved compared to a Medtronic DBS lead. More importantly, each cylindrical stimulation site in a commercial device has been replaced with 4 independent electrodes around the shaft of the implant. The thin film probes wrap around the polyurethane shafts with a $\sim 240^{\circ}$ solid angle. Wider solid angles are possible to achieve by increasing the width of the planar microprobe and employing a four piece mold for assembly.

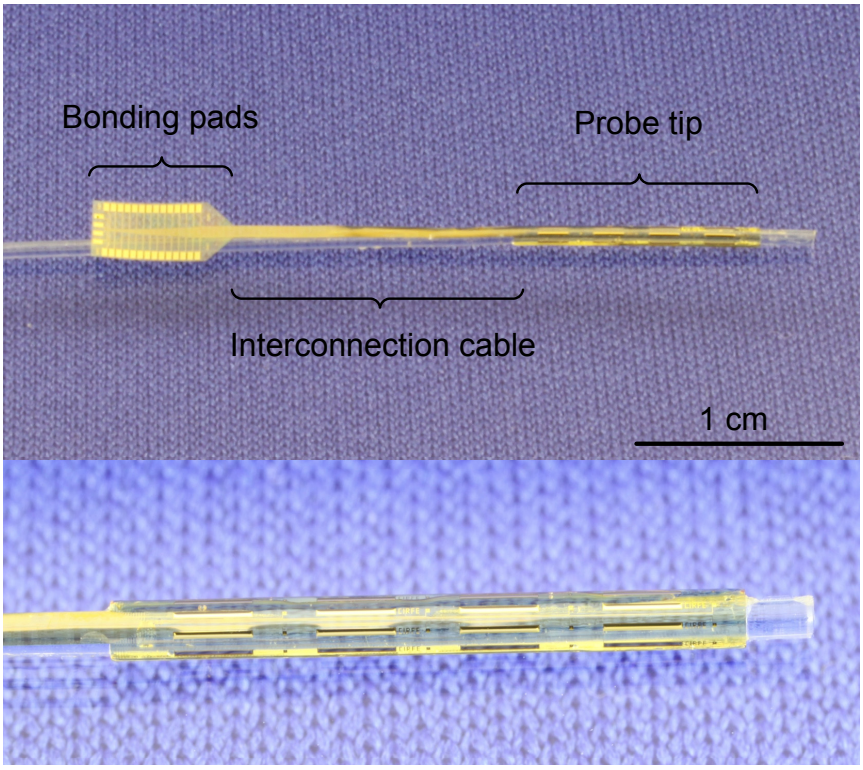


**Fig. 4.6: Optical images of a 3D DBS microprobe.**

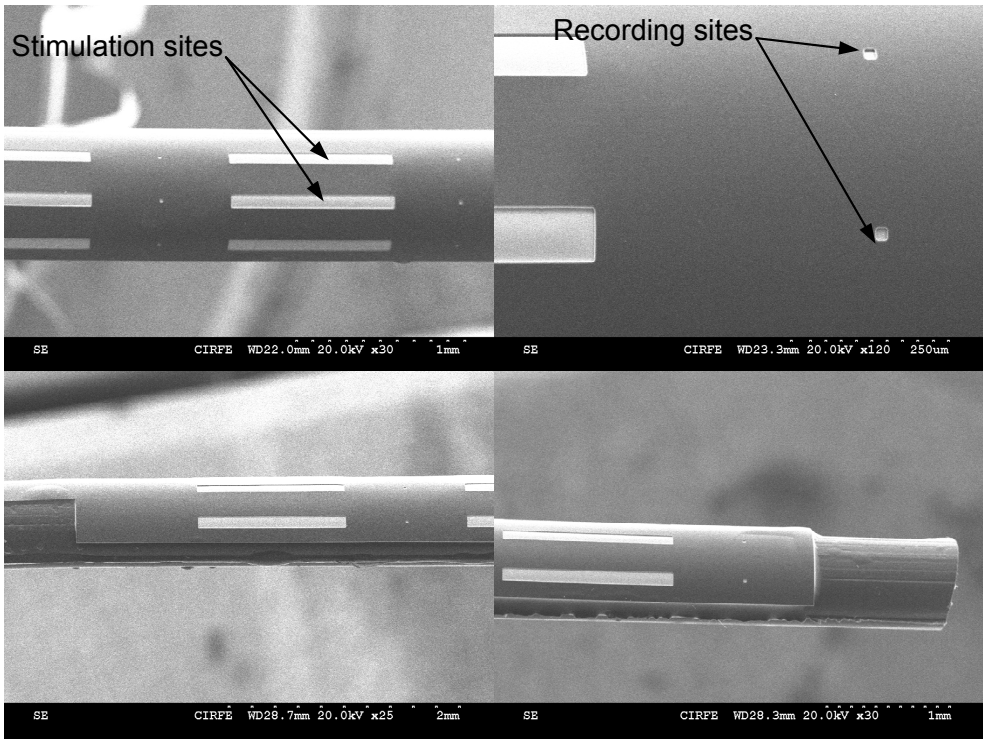


**Fig. 4.7: SEM Images of a 3D DBS microprobe.**

The close up SEM images in Fig. 4.7 confirms that the electrode sites, particularly the large stimulating sites, have not been damaged throughout the assembly process. The surface of the electrode sites is 4 $\mu$m below the top surface of the planar probe and therefore during the assembly the electrodes are not in immediate contact with the mold. Furthermore, the flexibility of the gold and polyimide allows the planar microprobes to uniformly bend over the shaft. No buckling in the gold electrode sites, cracks in the gold layer, or detachment of the metal from polyimide layer is seen in the SEM images. To further reduce the manipulation forces and improve the yield of the fabrication, prior to folding the devices over the polyurethane shafts, the thin film probes have been placed in a half cylindrical mold with diameter of 1 mm. A metal needle, 0.5 mm in diameter, has been used to push and hold the planar probes inside this mold. The ensemble was then annealed at 200 °C for 2 hrs. After release, the microprobes have a curved-shape with 1mm diameter.

The initial curvature of thin film probes significantly simplifies the alignment of the sample with the shafts and the insertion into the final mold.

After the fabrication of the microprobes, the bonding pads of the microprobes were connected to a commercially available IDC DIP plug connector using a custom made flexible cable. As described in chapter 3, a Kapton sheet (500HN from DuPont) with a thickness of 127 $\mu$m was used as the substrate of the flexible cable, and a 50 nm Cr / 1 $\mu$m Au bilayer was used to create the addressing lines. The IDC connector was mounted on the flexible cable, and the electrical connections were made by silver epoxy. To enhance the mechanical strength of the connection points, polyurethane were dispersed over the connection points and cured at 50°C for 24 hrs. The bonding pads of microprobes were then connected to the flexible cable using silver epoxy contact points and a mechanical force applied by 2 rectangular solid sheets screwed together. Fig. 4.8 presents the image of a DBS microprobe integrated with a 40 pin IDC connector. A ribbon cable can be easily attached to the connector to facilitate the electrical characterization of the fabricated devices.

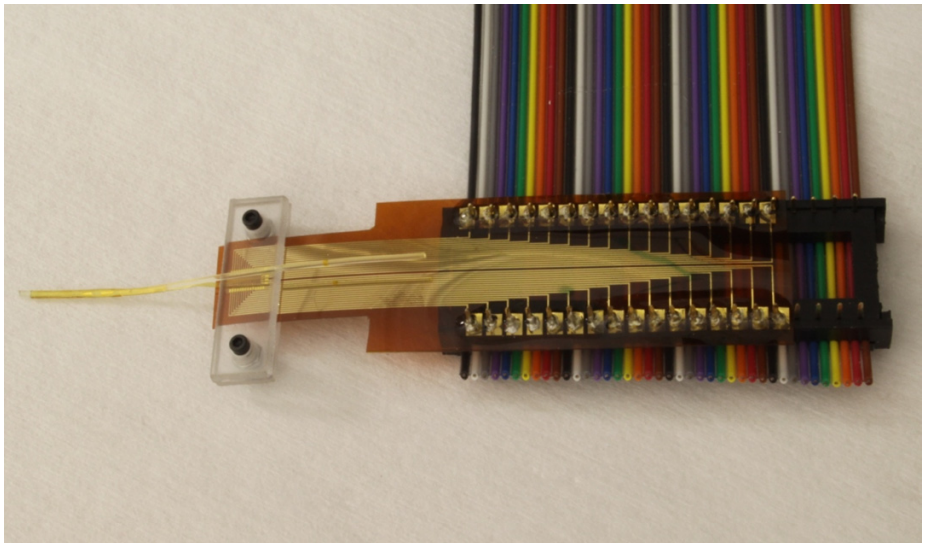

**Fig. 4.8: Photograph of a DBS microprobe integrated with a 40-pin IDC connector.**

## 4.3 Impedance Characteristics

The electrical characteristics of the addressing lines and electrode sites were studied employing the experimental setup described in section 3.3.2. An electroplating process was developed to deposit Ir over Au electrode sites. The impedance characteristics of the Ir and Au stimulation and recording electrodes are studied followed by the stability and in-vitro measurements.

### 4.3.1 Interconnection Cable and Connector

The DC resistances of the addressing lines connecting the bonding pads to the stimulating sites of the microprobe were measured using a four point probe technique. The lengths of the 10 $\mu$m-wide interconnection lines are 3 - 4 cm depending on the position of the site. The measured resistances are between 240 $\Omega$ to 340 $\Omega$ close to the theoretical value of 290 $\Omega$ expected for a 10 $\mu$m-wide, 300 nm-thick, and 4 cm-long gold conductor. The resistances of the interconnection lines for the recording sites can not be easily measured since the recording sites are smaller than the probe tip. Nevertheless, the lines should exhibit resistances close to those of the stimulating sites because of the similar aspect ratios. Similar to the IDC cables used for the intracortical microprobes, the resistances of the connector and cables are in the range of 90 $\Omega$ to 125 $\Omega$ measured between the contact points of the flexible cable and ends of the 1 m long ribbon wires.

### 4.3.2 Au Electrodes

The impedance magnitudes and phases of the stimulation and recording channels were measured in a 1M KCl saline solution using the tri-electrode experiment setup described

in section 3.3.2. Ag-AgCl and Pt were employed as the reference and counter electrodes, respectively. A sinusoidal input signal was applied between the electrode sites and the counter electrode. The current and voltage between the electrode sites and the KCl electrolyte were recorded against the reference electrode and employed to calculate the site impedances.

The impedances of the stimulation and recording channels over the 10 Hz – 300 kHz frequency range are presented in Fig. 4.9 and Fig. 4.10, respectively. The measured impedances consist of the resistance of the connector, cables, and addressing lines ($R_{Address}$), the electrode site impedance ($Z_e$), and the uncompensated electrolyte impedance ($Z_{Elec}$). The equivalent circuit model of a stimulating or recording channel in an electrochemical cell is shown in Fig. 4.11. The electrolyte impedance from the reference to the counter electrode was mainly resistive and found to be negligible compared to the recorded impedances of the channels even at 300 kHz. For the recording channels, the total parasitic resistance of the addressing line in series with resistance of flexible cable, connector, and test wires (less than 500 Ω) is substantially smaller than the impedance of the recording channels

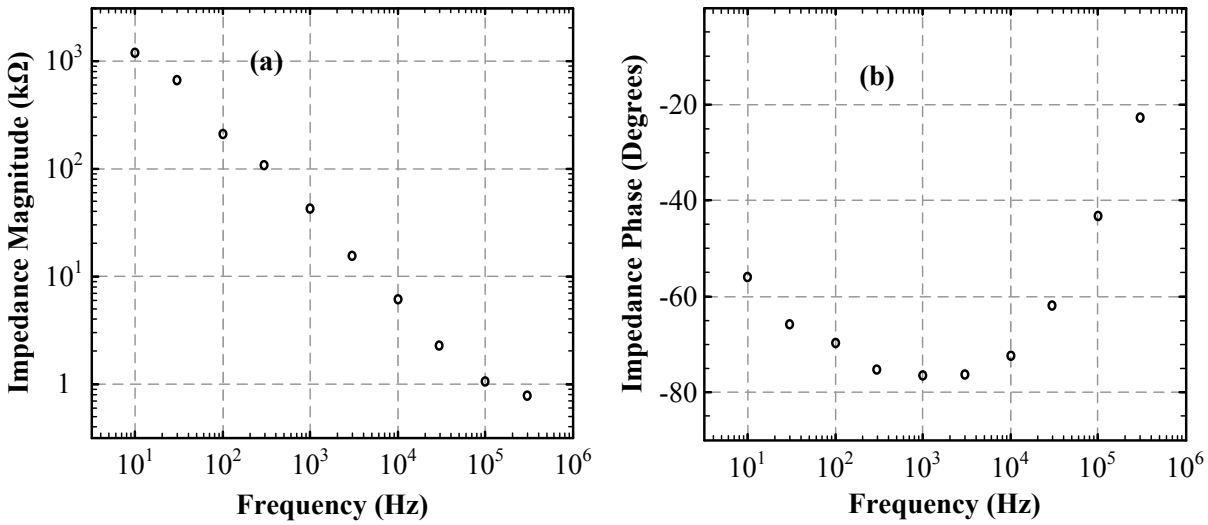


**Fig. 4.9: (a) Impedance magnitude and (b) phase of a 0.1 mm × 1.5 mm stimulation channel.**

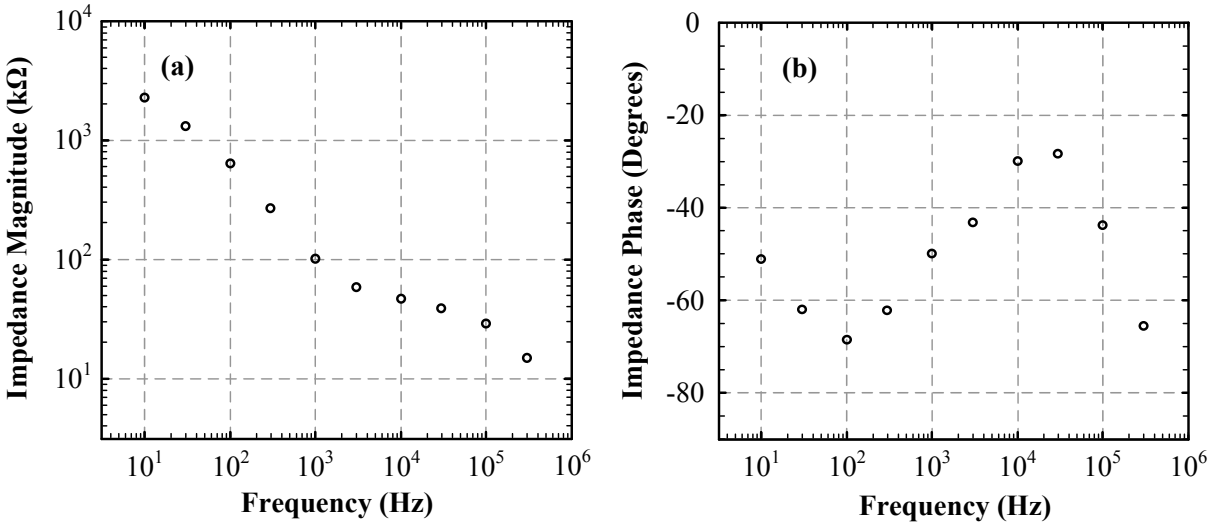


**Fig. 4.10: (a) Impedance magnitude and (b) phase of a 20 $\mu$m $\times$ 20 $\mu$m recording channel.**

(higher than 10 kΩ at 300 kHz) thus can be ignored in practical applications. On the other hand, for the stimulation channels, the series parasitic resistance is not negligible compared to the channel impedance at frequencies higher than 10 kHz. However, for most DBS applications, the frequency of stimulus is less than 1 kHz where the channel impedance is higher than 10 kΩ. The electrode site impedance is comprised of two distinct elements as shown in Fig. 4.11. The impedance $Z_f$ models the faradic charge transfer process to the solution, while the capacitance $C_d$ is the electrode-electrolyte double layer capacitance. At low frequencies, the impedance associated with the faradic process is dominant. For

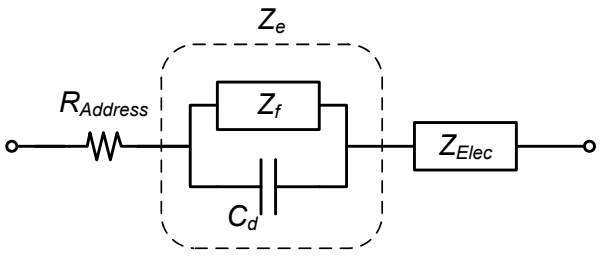


**Fig. 4.11: The equivalent circuit model of the measured channel impedances and the impedance of electrode sites, $Z_e$.**

the recording channels, at high frequencies, the double layer capacitance provides a more effective current path to the solution and therefore determines the overall electrode site impedance. In this frequency range, the impedance of the electrodes should exhibit more capacitive behaviour as the frequency increases. Fig. 4.10(b) confirms that the phase lag of the recording site impedance rapidly rises above 30 kHz. For the stimulation site, the high frequency impedance of the channels is mainly determined by the resistance of the addressing lines $R_{Address}$. In Fig. 4.9(b), a substantial drop is observed in the phase lag of the measured impedances at frequencies higher than 100 kHz. Furthermore, the impedance magnitude of the channel is close to the values of the $R_{Address}$.

### 4.3.3 Ir Electrodes

To improve the electrical characteristics of the channels in terms of the impedance and capacity of the charge delivery, the electrode sites were electroplated with iridium. The Ir electro-deposition was performed in an aqueous solution containing 6.2 $gr/l$ Ammonium Chloroiridate III, 14.0 $gr/l$ Ammonium Fluoride, 23 $ml/l$ sulphuric acid (98%), and 20 $ml/l$ sodium hydroxide (20%) [112]. At a current density of 200 $mA/cm^2$ and a temperature of 70 °C, a 200 nm layer of Ir was plated over the gold sites at a plating rate of 4.5 $\mathring{A}/s$. Films that were thicker than 500 nm or deposited at faster rates were not stable and delaminated

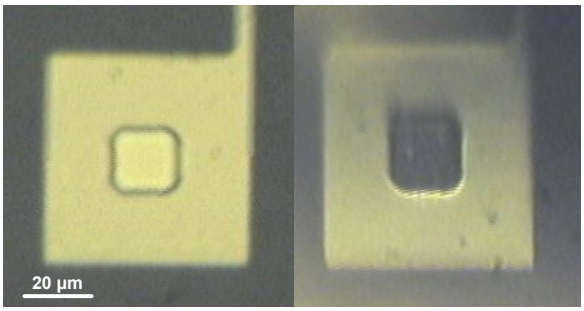


**Fig. 4.12: Optical images of a recording site before and after Ir plating.**

from the gold seed layer due to the presence of high residual stress in the Ir layer. Fig. 4.12 illustrates optical images of a recording electrode site before and after the Ir plating. The Ir-plated site (right) appears black in color due to the increased surface roughness of the electrode.

The impedances of the Ir-plated stimulation and recording channels over the 10 Hz – 300 kHz frequency range are depicted in Fig. 4.13. The measurements were performed

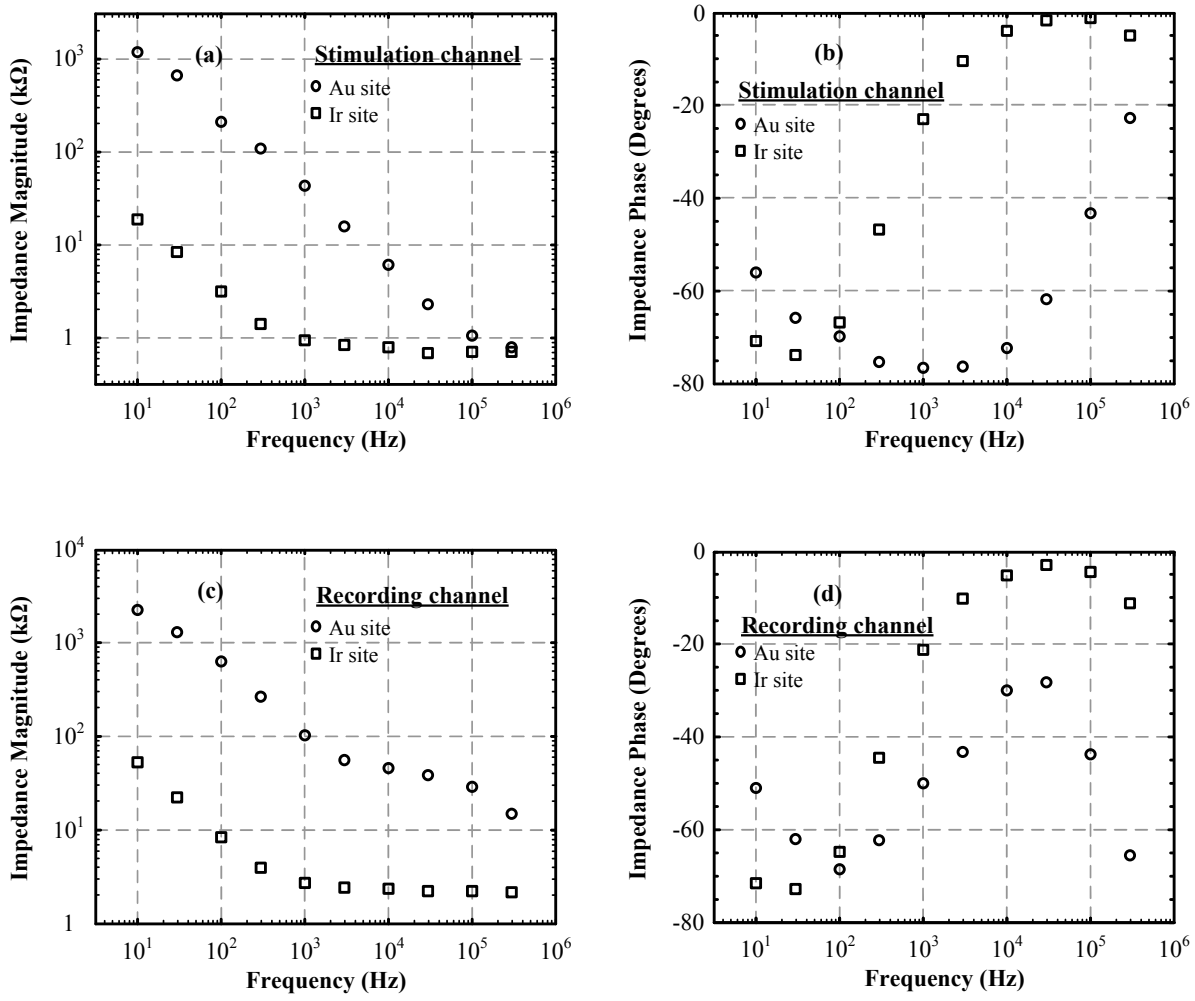


**Fig. 4.13: Impedance magnitudes and phases of Ir-plated stimulation ((a) and (b)) and recording ((c) and (d)) channels. The corresponding impedance values for gold electrodes are also shown for comparison.**

at room temperature in 1M KCl saline solution. As expected, the impedances of the Ir electrodes are substantially less than the corresponding values for the gold electrodes at frequencies where $Z_f$ is dominant. The electrode impedances demonstrate increased capacitive characteristics at very low frequencies such as 10 Hz. This behaviour can be attributed to the higher charge delivery capacity of the Ir layer and the increased surface roughness of the electrode sites. For recording electrodes, $Z_f$ rapidly becomes resistive at higher frequencies and thus determines the overall impedance of the channel. The same trend is also observed for the stimulation electrodes, although the resistance of the addressing lines dominates the channel impedance at frequencies above 1 kHz.

## 4.4 Impedance Stability

To study the impedance stability of the stimulating and recording sites, the Au and Ir electrode sites were subjected to a prolonged pulse test. A square wave pulse with a 4 V peak-to-peak voltage (+2 V to –2 V) was applied between the Au electrodes and the reference electrode for 100 million cycles in a 1 M KCL saline solution. The frequency of the stress pulse was 10 kHz with a 50% duty cycle. The electrode impedance was measured frequently during the pulse test. At these points, the stress pulse was stopped and a sinusoidal signal was employed for impedance measurement. Fig. 4.14 depicts the impedance magnitude and phases of the Au stimulation and recording electrode sites before and after the pulse stress test.

Fig. 4.15 shows the evolution of the impedance magnitudes and phases of an Au stimulation site at 100 Hz and 10 kHz, and an Au recording site at 10 Hz and 1 kHz during the pulse test experiment. Initially, a rapid change in impedance values occurs followed by a saturating behaviour at longer times. At low frequencies, the phases of the impedances increase and $Z_f$ demonstrates higher capacitive characteristics. At higher

frequencies, the impedance magnitude of the Au stimulation sites saturates to values close to the resistance of the addressing lines with a substantially dropped phase lag. The observed trend for the impedance shifts suggests that the $Z_f$ is reduced due to the increase

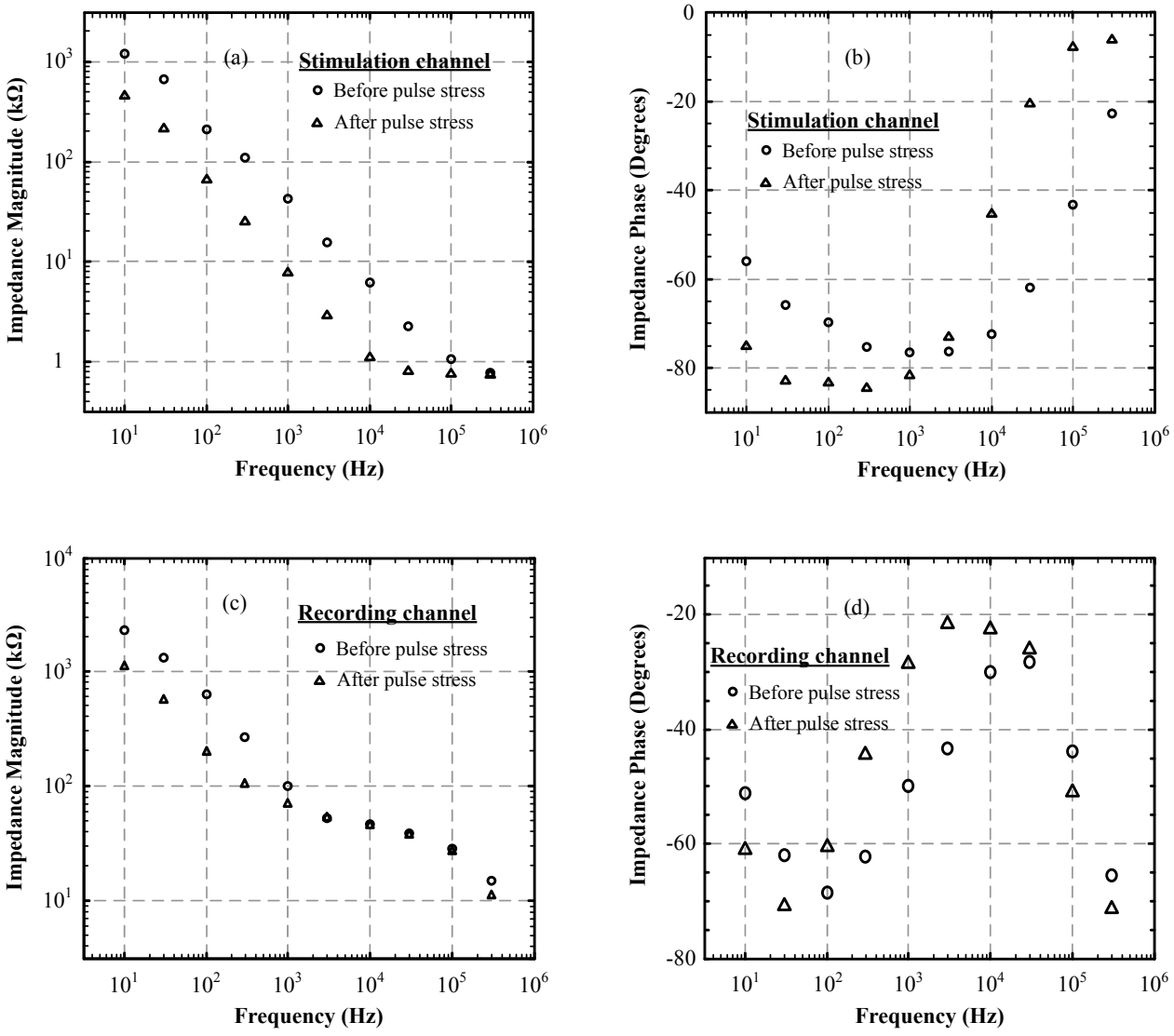


**Fig. 4.14: Impedance magnitudes and phases of Au stimulation ((a) and (b)) and recording ((c) and (d)) channels before and after 100 million cycle pulse test in KCl saline.**

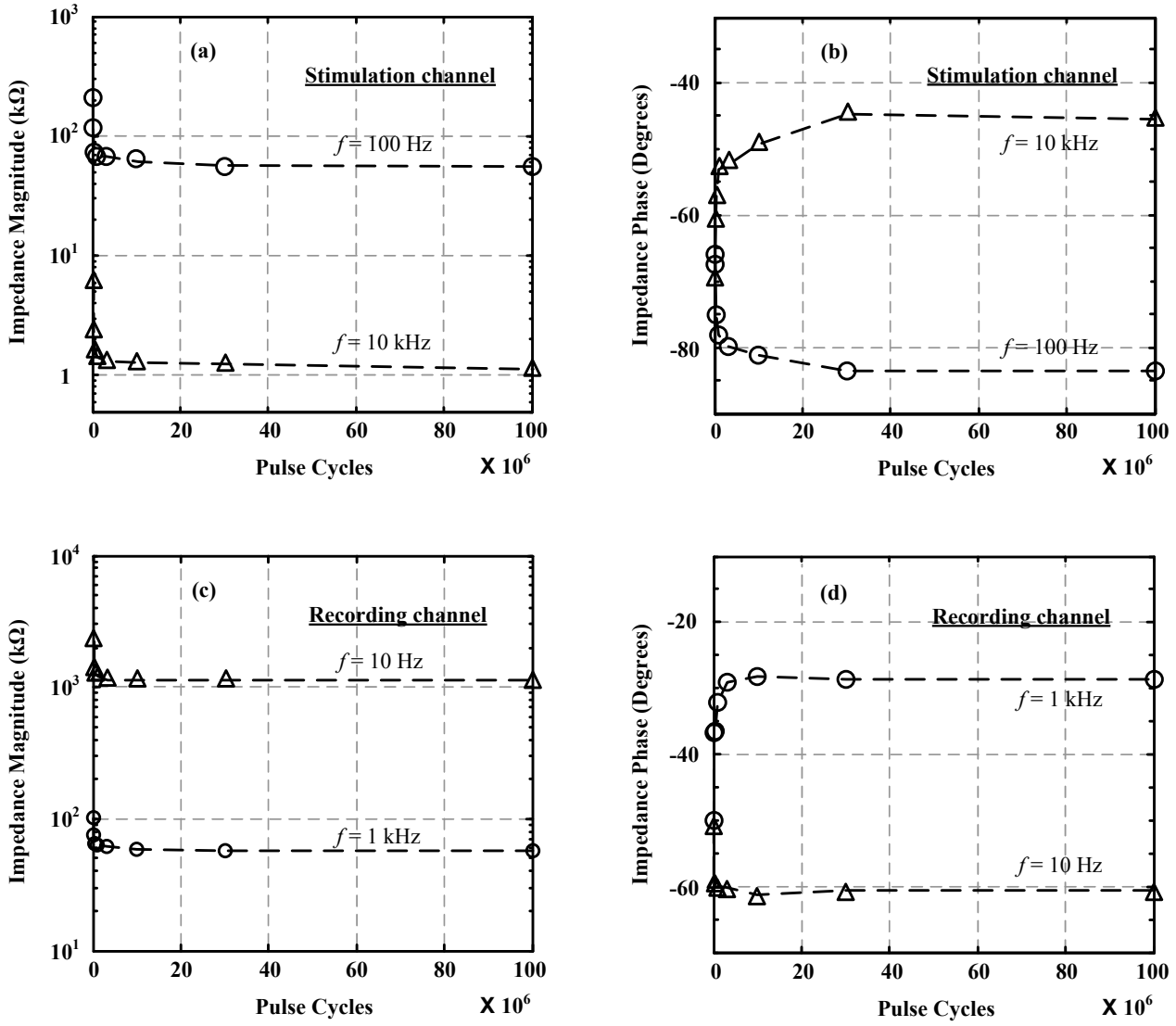


**Fig. 4.15: (a) and (b) Impedance magnitudes and phases of an Au stimulation site at 100 Hz and 10 kHz. (c) and (d) Impedance magnitudes and phases of an Au recording stimulation site at 10 Hz and 1 kHz.**

in the pseudo-capacitance of the faradic charge transfer process. A possible explanation for this behaviour is the cleaning of the electrode surface in a process similar to the electrochemical cleaning. To expose the electrode site, the polyimide was removed in an RIE dry etching process. The etching of polyimide in RIE is known to leave polymeric residues

on the surface of underlying layers [113]. Although, the RIE process was optimized to eliminate the polyimide residues, it is possible that a nanometre-thin polymer layer covers the surface of the electrode. Such a thin trace of residues is not detected in the SEM images but will reduce the effective area of the electrode and hinder the charge transfer to the solution. Upon removal of this layer, the surface area of the electrode is substantially enhanced, resulting in lower $Z_f$ and channel impedance.

A pulse stress test was also performed in a 1 M HCl solution to investigate the characteristics stability of the channels in a strong acidic solution. The drift in impedance was not as pronounced over the course of the experiment in HCl. The smaller initial impedances measured in the HCl can be explained by the effect that the HCl solution has on the polymeric residues left over the surface of the electrodes. When the probe is immersed in the solution, it is possible that the HCl solution partially dissolves or attacks the polymer layer. Therefore, the initial measured impedance value is less than that recorded in the KCl. After the pulse test, the electrode sites were examined under an optical microscope. No signs of surface damage or metal delamination were detected in the microprobes demonstrating the potential of fabricated microprobes for chronic applications.

The long term stability of Ir electrode sites under a prolonged pulse stress in a 1 M KCl solution was studied. A square wave signal with a peak-to-peak voltage of 3 V (+1.5 V to -1.5 V) was employed between the channel and the reference electrode in this experiment. The frequency and pulse width of the stress signal were set to 10 kHz and 50 s, respectively. The impedances of electrode sites were measured frequently during the pulse test. Fig. 4.16 depicts the impedance magnitudes and phases of the Ir-plated stimulation and recording channels before and after a 100 million cycle pulse stress test. The channels demonstrate a stable impedance over the course of the experiment. The electrode sites were then inspected under an optical microscope and no sign of degradation in the Ir-plated layer was observed.

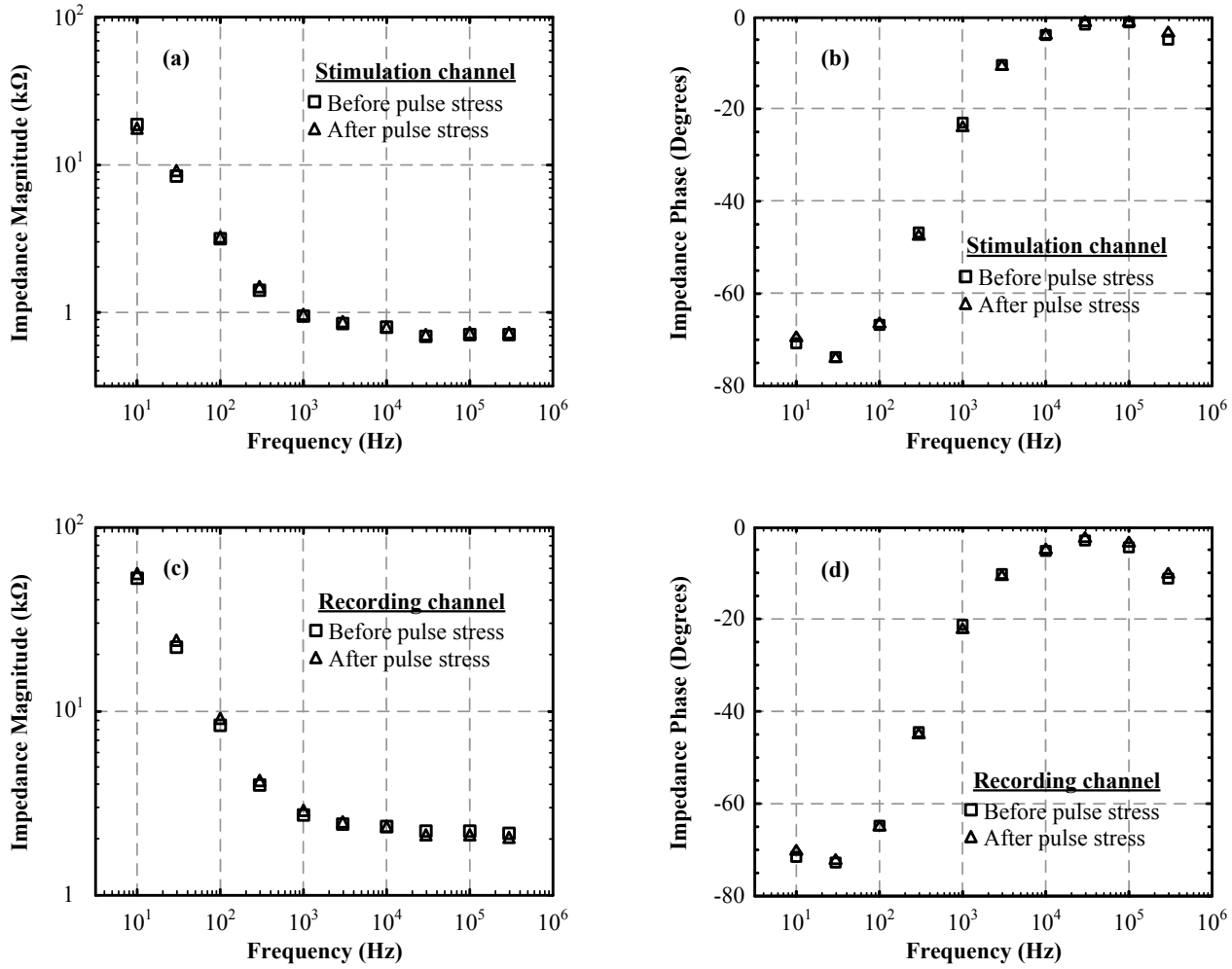


**Fig. 4.16: Impedance magnitudes and phases of an Ir-plated stimulation ((a) and (b)) and recording ((c) and (d)) site before and after a 100 million cycle pulse stress test.**

## 4.5 In-vitro Stimulation and Recording

The in-vitro experiments were performed in a whole hippocampus prepared from 7-10 days postnatal C57BL/6 mice. To comply with the animal care standards, these mice were housed with one to six littermates and a nursing mother in a well equipped animal facility,

receiving artificial light for 12 hrs every day at a constant temperature of 23 ± 1 °C. These animals were anesthetized with Isoflurane 2.5% MAC to extract their brains. The brains were rapidly submerged in cold (≤ 4 °C) Artificial Cerebro-Spinal Fluid (ACSF) with an osmolarity of 300 ± 10 $mOsm/l$ and a Ph of 7.38 ± 0.05 after bubbled with carbogen (95% $O_2$ + 5% $CO_2$). The ACSF solution contains 123 $mM$ NaCl, 4.0 $mM$ KCl, 1.5 $mM$ $CaCl_2$, 1.6 $mM$ $MgSO_4$, 25 $mM$ $H_2CO_3$, 1.2 $mM$ $NaH_2PO_4$, and 10 $mM$ D-glucose. After approximately 2 min, the hemispheres were removed from the cold ACSF solution and the hippocampi were extracted as described in [102]. Next, the tissues were placed for 30 min into a 33 °C oxygenated ACSF bath containing 1 $mM$ kynurenic acid. Subsequently, the bath passively cooled down and maintained at room temperature for at least one hour prior to the start of the experiment.

Electrical stimulation and recordings were performed in a custom made perfusion chamber at a constant temperature of 34 °C. The chamber supplies a surrounding fast ACSF flow of $\sim 10$ $cc/min$ for sufficient oxygenation of the submerged tissue [114]. The 3D DBS microprobe was mounted on a micromanipulator to position the stimulation and recording electrodes into the tissue. The neural signals from the 3D DBS microprobe and an extracellular glass electrode with a resistance of 3-5 MΩ were amplified using Axoclamp 200B amplifiers (500 gains) and digitized with a Digidata 1322A digitizer (Axon Instruments). The signal was acquired at a sample rate of 10 kHz after passing through a lowpass filter with a 5 kHz cut-off frequency. The post signal processing analyses were then carried out in Clampfit 10.1 software (Axon Instruments) using a 10-pole Chebyshev bandpass filter with 0.5 Hz and 1 kHz 3dB frequencies.

Fig. 4.17(a) and (b) demonstrate the spontaneous field activities recorded by the 3D DBS probe and the glass electrode. A good agreement is observed between the signals confirming the capability of the fabricated devices to record small signals from population activity. The response of the hippocampal network circuitry to the electrical stimulation

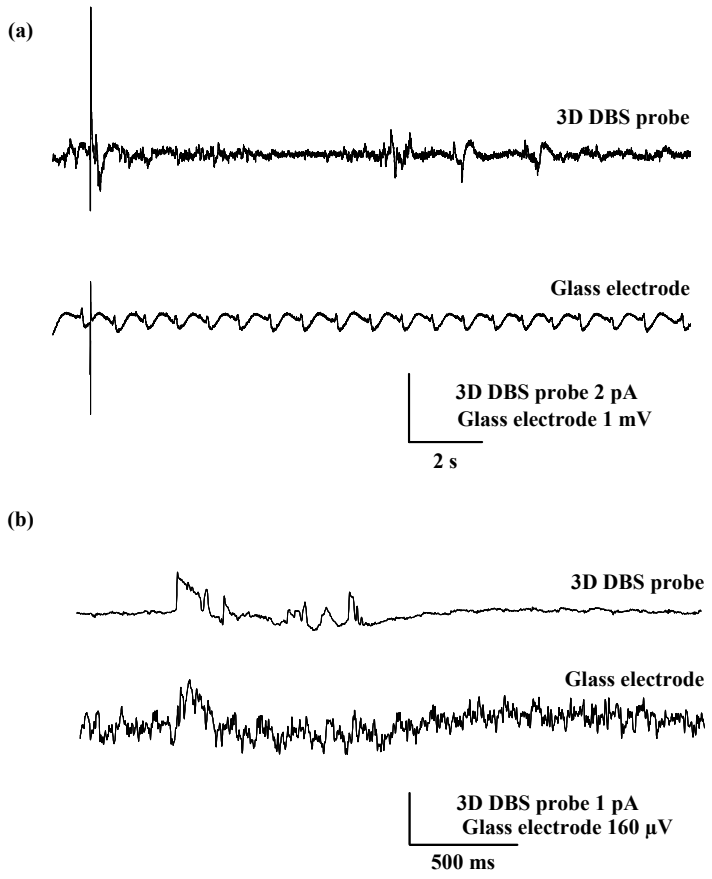


**Fig. 4.17: Recorded spontaneous field activities in a C57BL/6 mouse hippocampus with 3D DBS and glass electrodes.**

was also investigated by the application of a stimulus signal shown in 4.18(a). Both the recording electrode from the 3D DBS and the glass electrode were able to record the stimulus artifact and the biological response as illustrated in Fig. 4.18(b). The Excitatory Post-Synaptic Potential (EPSP) was observed with an average amplitude of 20 $pA$ and a decay time of 7 $pA/ms$. The recording from the 3D DBS electrode was carried out in current clamp configuration mode due to the incompatible impedance of the fabricated devices with that of the input stage amplifier. However, it is possible to approximate the voltage level of the neural activity from the recorded current and the frequency response of the electrode impedance.

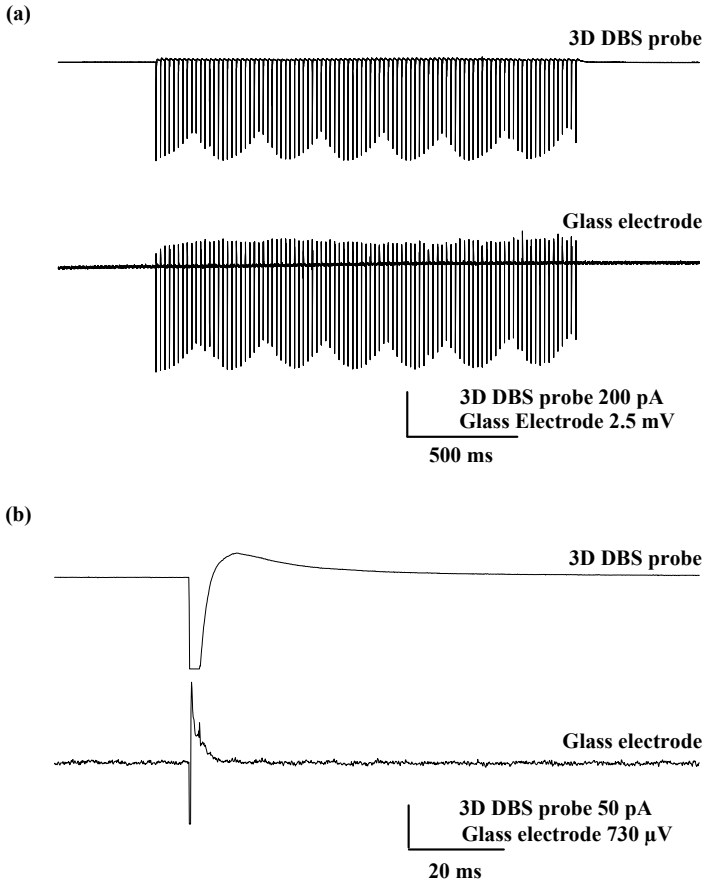


**Fig. 4.18: (a) The 100 Hz stimulus signal produced by the 3D DBS stimulating site and recorded with an adjacent recording site and the glass electrode. (b) Excitatory postsynaptic potential (EPSP) evoked by the 3D DBS probe.**

## 4.6 Summary

This chapter elaborated on the fabrication and characterization of the proposed 3D DBS microprobes offering independent stimulation and recording sites around the shaft. The dimensions and density of the electrode sites are precisely controlled by the lithography processes employed for the fabrication of thin film planar devices. These devices are then assembled on a flexible support structure to construct the implants. The fabricated microprobes are 12 mm in length and 750 $\mu$m in diameter at the tip section and provide 16

stimulation and 16 recording channels. The device volume has been reduced to one third the volume of a conventional Medtronic DBS lead. The impedances of the stimulation and recording channels with Ir and Au electrode sites were studied employing a tri-electrode experimental setup. Both the stimulation and recording channels exhibit long term stable characteristics in saline and acidic solutions. The spontaneous field activity and Excitatory Post-Synaptic Potential (EPSP) were successfully evoked and recorded employing the proposed 3D DBS microprobes in a mouse hippocampus. Table 4.1 compares properties of the proposed 3D DBS microprobes to those reported in literature.

**Table 4.1: Comparison of the DBS microprobes' properties**

| DBS probe | Stimulation channels | Recording channels | Cross-section (mm) | Precise dimension control | Integrated flexible cable | Control field distribution |
|---|---|---|---|---|---|---|
| Niotrode [52] | 0 | 9 | r = 0.1 | No | No | No |
| Microwire bundles [27] | 0 | 16 | r = 2 | No | No | Limited |
| Medtronic's lead [50] | 4 | 0 | r = 1.27 | Yes | Yes | No |
| 3D Electroplated [33] | 5 | 0 | $0.3 \times 0.1$ | Yes | No | No |
| Proposed 3D probes | 16 | 16 | r = 0.75 | Yes | Yes | Yes |

# Chapter 5

# MEMS Integration

In the neural stimulation and recording with a large number of electrodes, the application of a site selection matrix is a common solution to reduce the number of channels and to simplify the signal processing circuitry [115, 116]. The site selection matrix is a switching matrix comprised of several switching elements to route the stimulating or recording circuitry to the appropriate electrode site. The integration of the switching matrix with the microprobe and the interconnection cable on the same substrate also decreases the number of connections between the probe and the external circuitry. Silicon Very Large Scale Integrated (VLSI) circuits have been successfully used for the implementation of the site-selection matrices and the integration with implantable devices [115–118]. Although these circuits are attractive because of their reliable performance, small size, mature fabrication process, and easy passivation, they cannot be fabricated on the non-silicon substrates used for the production of flexible microprobes.

Micro-Electro-Mechanical Systems (MEMS) technology is a promising candidate for the fabrication of switching matrices on flexible substrates. The switching matrix, the microprobe, and the interconnection cable can be integrated on the same substrate to improve the reliability and reduce the cost of the device. Another advantage of the MEMS switches over the conventional semiconductor switching elements is the good switching performance

of the MEMS devices [53] in terms of a low on-state resistance, high off-state isolation, and low power consumption. These attributes are very desirable for biomedical applications, where a long battery lifetime of the implanted device is of significant importance.

This chapter involves the development of switching elements and matrices for futuristic integration with biomedical devices. Multiport switch matrices are introduced for low frequency and Radio Frequency (RF) applications. A novel generation of magnetic actuated switches is reported for enhanced operation reliability. A detailed discussion of the fabrication, design, and characteristics of these devices are presented.

## 5.1 Multichannel Stimulation and Recording

The simplified block diagram of a wireless neuroprosthetics system is illustrated in Fig. 5.1. The system consists of a multisite neural microprobe, power supply, transceiver, switching matrix, and a microcontroller unit. The stimulation/recording channels of the micro-

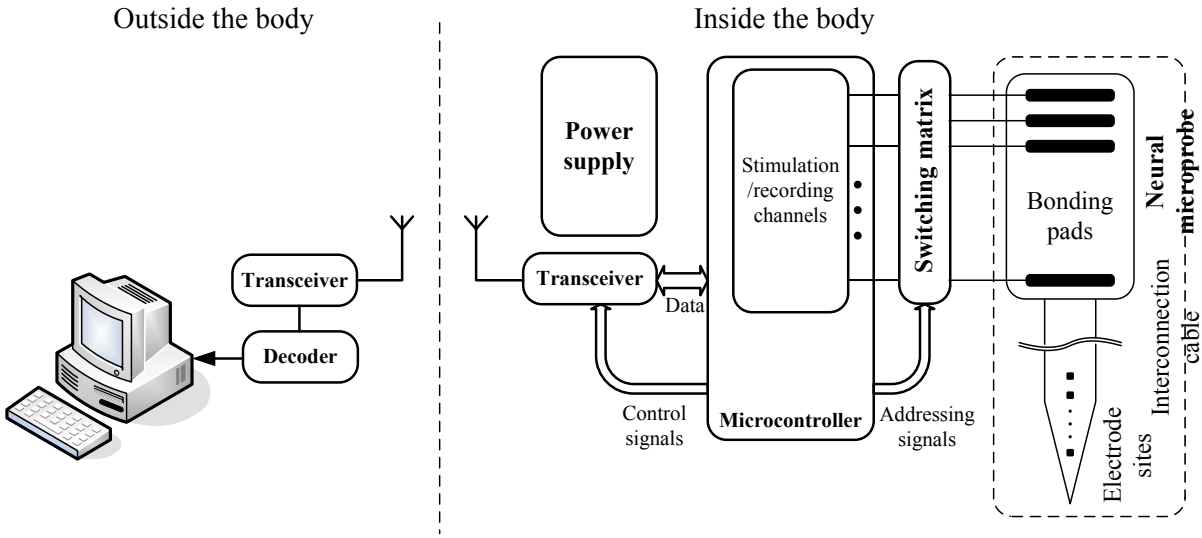


**Fig. 5.1: Block diagram of a wireless neuroprosthetics.**

controller are connected to the electrode sites through the switching matrix. The functions of the transceiver are to transmit the recorded signal and receive the stimulation program. The micro-controller synchronizes the operation of the components, applies the stimulation signal, records the neural activities, performs the digital/analog data conversion, and carries out other necessary signal processing tasks. For instance, the micro-controller must encrypt the transmitted signal to ensure the security of the communicated information. The data is then transferred to a computer through a transceiver for monitoring the recorded activities and modifying the stimulation program.

A stimulation channel consists of a Digital to Analog Converter (DAC) and a driver circuit to generate the stimulation waveform. The main components of a recording channel are a low noise amplifier to enhance the signal to noise ratio and an Analog to Digital Converter (ADC) to digitize the recorded signal. An embedded switching matrix significantly reduces the complexity and dc power consumption of the electronics. Fig. 5.2 illustrates a possible design of a 32 channel conventional recording system in which each channel has been directly connected to the micro-controller. Therefore, 32 independent recording amplifiers and ADCs are required to construct this system. Alternatively, if a switching

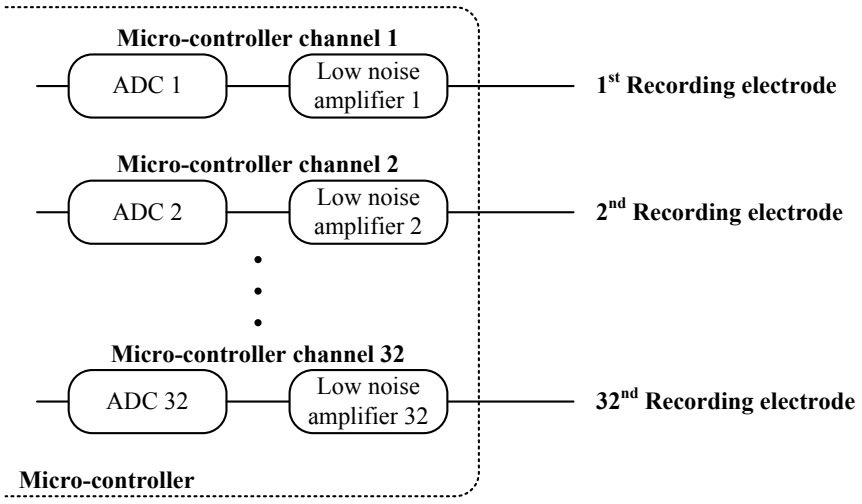


**Fig. 5.2: Configuration of a 32 channel neural recording system.**

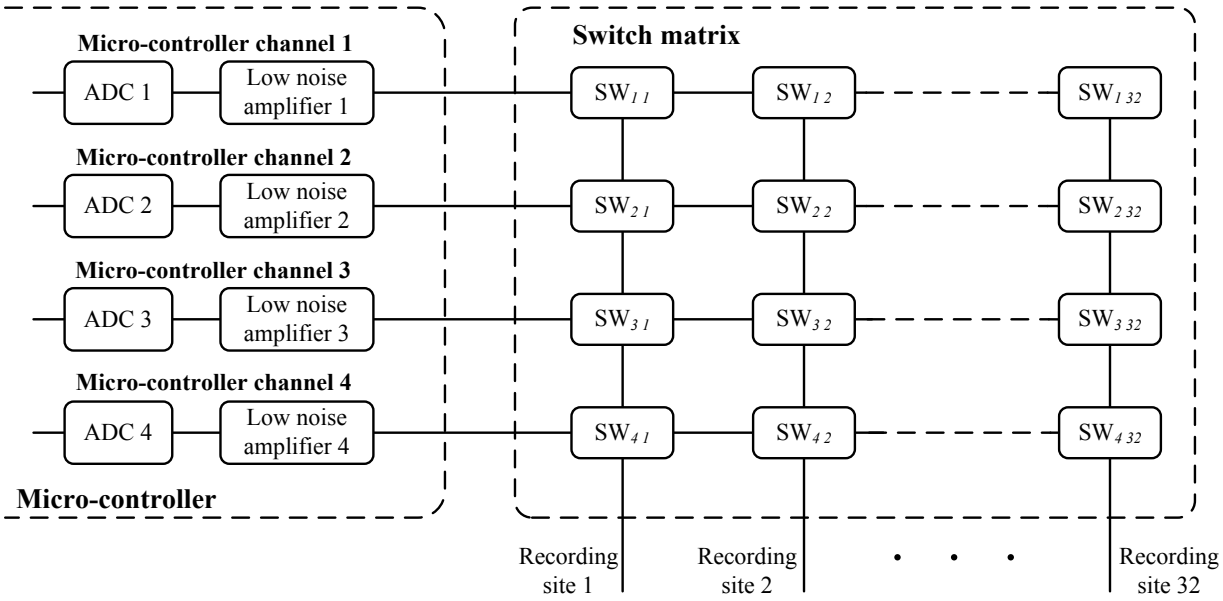


**Fig. 5.3: Configuration of a 32 channel neural recording system utilizing a switch matrix for connecting a 4 channel micro-controller to a 32 site neural microprobe.**

matrix is employed as shown in Fig. 5.3, only 4 recording amplifiers and 4 ADCs are needed. The micro-controller channels can access the desired electrode sites by activating the appropriate switching elements in Fig. 5.3. Consequently, each micro-controller channel can be shared between several electrode sites of the microprobe. Moreover, in the case of a channel failure, it is still possible to record from all of the recording electrodes of the probe by routing the electrode sites to the functional channels.

In this doctoral study, electrostatic and magnetic-actuated contact type MEMS switches were fabricated for the application as the building block of a site selection switch matrix. Multiport $4 \times 4$, $8 \times 8$, and $4 \times 12$ matrices were successfully constructed and characterized.

## 5.2 MEMS Switching Elements

The basic principle behind the operation of MEMS switches is the displacement or deflection of a moving part such as a cantilever or a beam by various types of actuation mechanisms. Typically, actuation occurs by the application of electrostatic [119–123], electrothermal [124–127], or electromagnetic [128–130] forces. MEMS switching elements offer exceptional characteristics such as very low power consumptions, high isolation, and low insertion loss [131, 132]. The superior performance of MEMS devices can be employed to construct multiport switch matrices with scaled dimensions or improved characteristics compared to those produced by mechanical or semiconductor devices. Although several MEMS switch matrices have been reported in literature [133, 134], these circuits are mostly suited for RF applications due to their large dimensions and relatively low number of input / output ports.

The approach adopted here is based on the development of contact type series switches to provide the low On-state resistance demanded in biomedical applications. In this category of switches, a metal conductor physically connects the input and output terminals when the device is turned On. In the Off-state, this metal conductor is disconnected from one or both of the signal lines, eliminating the signal path. Both metal and dielectric cantilever devices were explored in this study due to the simplicity of the design, structure, and fabrication.

## 5.3 Electrostatic-Actuated Monolithic MEMS Switch Matrices for Wide-Band Applications

Several switching cells are employed in the form of a simple array to create a $4 \times 4$ matrix [98, 135]. The switching cells are constructed from metal cantilever switches with a

Single Pole Single Throw (SPST) configuration. The expansion of the matrix can be easily accomplished by adding more rows or columns of the switching cells. The fabrication and the RF performance of the fabricated matrix is presented. The impact of the sheet resistance of the bias lines on the RF characteristics and switching speed of the overall switch matrix are discussed in details.

### 5.3.1 Structure and Design

The proposed 4 × 4 switching matrix in this work has a cross-bar structure that consists of an array of switching units connecting the horizontally and vertically running input and output ports (Fig. 5.3). To be able to route any of the input ports to any of the output ports, each unit cell must offer two operating states; namely, the "Through" and "Turn" states. In the "Turn" state, the input port is connected to the output port and in the "Through" state, one or both of the ports are joined to the designated port(s) of the adjacent unit(s).

The operating states of the unit cell are graphically illustrated in Fig. 5.4(a). To achieve these operating states, three SPST switches and a crossover are employed in the structure of the switching unit in the configuration shown in Fig. 5.4(b). In the "Turn" state, the connection switch (S2) is On and the isolation switches (S1 and S3) are Off. Therefore, the input and output states are connected and isolated from other ports. In the "Through" state, either one or both of the isolation switches are On providing the transition of the desired port(s) to the adjacent unit cell(s). To further enhance the performance of the constructed switch matrix based on this cell, at the last row or column of the matrix, the corresponding isolation switch is removed.

The compact size and simple structure of the metal cantilever contact type MEMS switches render them as one of the best candidates to produce this circuit. The devices

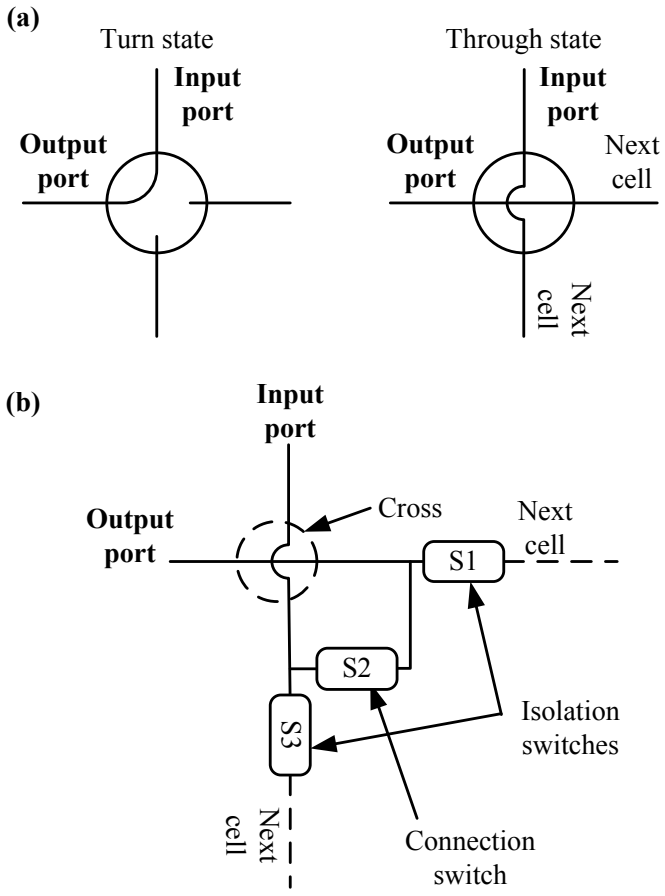


**Fig. 5.4: (a) Operating states and (b) configuration of the switching cell proposed for construction of the monolithic RF MEMS switch matrix.**

are coupled to Co-Planar Waveguide (CPW) transmission lines since the dimensions of the structures can be scaled below 100 $\mu$m, while, at the same time the desirable characteristics impedance of 50 $\Omega$ is achieved for the lines. The 3D schematic of the proposed structure is shown in Fig. 5.5. The signal and ground crossover lines are constructed using the top metal layer of the process that is employed to form the cantilever beams. From each of the transmission lines a shunt stub is branched toward the connection point. In fact, one of the stubs is the connection switch S2 shown in Fig. 5.4(b). To complete the structure of the circuit, two MEMS devices are placed in series at the end of each transmission line

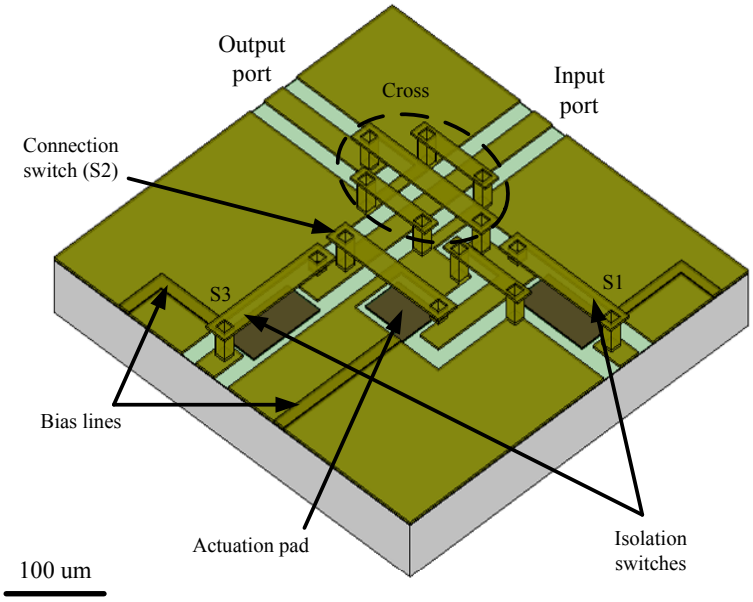


**Fig. 5.5: 3D schematic of the switching cell employed as the building block of the monolithic RF MEMS switch matrix.**

to act as the isolation switches S1 and S3.

The equivalent circuit shown in Fig. 5.6 is considered to describe the design methodology and the reason behind the selection of the proposed structure. At the frequencies where the signal wavelength is much larger than the sizes of the cross and MEMS elements, lumped element components can be used to model the response. In this circuit, the signal on each port can be coupled to the ground or to the other port at the crossover point through the signal-to-signal ($C_{ss}$) or signal-to-ground ($C_{sg}$) capacitances. To reduce the detrimental effects of these parasitic elements, the reduction in component sizes is necessary. If the widths of the signal line and ground crossover are set to 20 $\mu$m, these capacitances are approximated to be in the range of 1.5 fF. This value of capacitances produces shunt impedances as high as 3 k$\Omega$ even at frequencies as high as 40 GHz. As a result, compared to the values of 50 $\Omega$ for the characteristics impedance of the transmission line, the loading effect of these capacitances can be neglected.

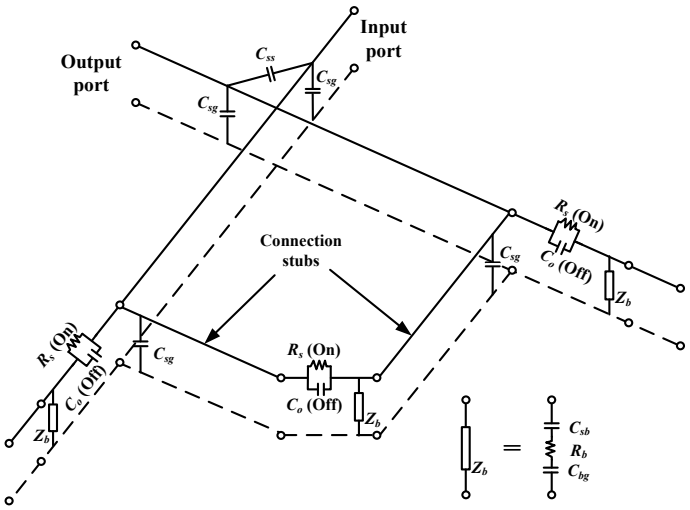


**Fig. 5.6: The equivalent circuit model of the switching cell.**

The lengths of the connection stubs affect the performance of the unit cell especially in the "Through" state. In the proposed design, the connection stubs are chosen to be shorter than 150 $\mu$m which is roughly 5% of the guided wavelength at 40 GHz ($\lambda_g = 3400$ $\mu$m simulated in ADS). Hence, the connection stubs will act according to the operating state of the connection switch and produce an insignificant effect in the "Through" state.

The widths and lengths of the MEMS switches' cantilevers are set to 20 $\mu$m and 145 $\mu$m, respectively; based on the designed values for the widths of the signal / ground crossovers and the lengths of the connection stubs. The MEMS switches can be modeled by a capacitance ($C_o$) when the switch is Off. The magnitude of the $C_o$ is similar to $C_{sg}$ or $C_{ss}$ and the same discussion applies for the loading of the MEMS switches in the Off-state. On the other hand, in the On-state of the switch, a series resistance ($R_s$) is limiting the operation. Indeed, the larger the switching matrix, the higher the demand on the contact properties of the switches. Depending on the contact force and the contact material, $R_s$ values as low as 0.1 – 0.5 $\Omega$ can be achieved. In our proposed design, for each of the operating states, there is only one MEMS switch located in the signal path. This means the loss of the signal, which is mainly due to the contact resistance of the switches, should

be approximately similar for all the paths. Consequently, in a 4 × 4 switch matrix, the highest insertion loss is expected to be associated with the longest path connecting the farthest ports that includes 7 switching elements.

The EM simulation results produced by High Frequency Simulation Software (HFSS) are shown in Fig. 5.7 for the response of the switch cell in the "Turn" and "Through" operating states. It is predicted that the unit cell performs satisfactory at frequencies

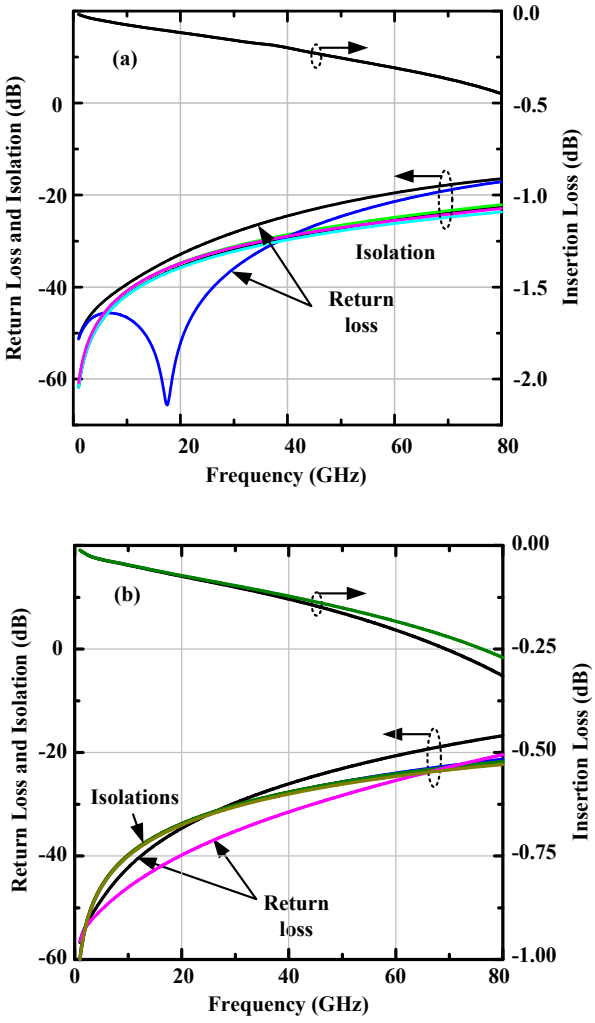


**Fig. 5.7: The EM Simulation results of the switching cell in (a) "Turn" and (b) "Through" states.**

as high as 60 GHz. However, the effects of the bias lines and the contact resistances of the switches have been ignored to simplify the simulation process. The bias lines provide coupling paths from the signal to the ground where the bias line connects to the actuation pads of the MEMS devices or underpass the transmission lines. The effect can be modeled by a shunt impedance, $Z_b$, comprised of the capacitance between the signal and bias lines ($C_{sb}$) in series with the bias line resistance ($R_b$) and the bias line to the ground capacitance ($C_{bg}$). As it will be discussed in details, the application of the conventional material such as chromium for the bias lines limits the proper performance of the device especially for large matrices. The contact resistances also deteriorate the insertion loss of the system. However, it will be demonstrated that the simulated results are in good agreement for a fabricated matrix up to 40 GHz.

### 5.3.2 Fabrication

The fabrication of the proposed devices and switch matrices was carried out in the Center for Integrated RF Engineering (CIRFE) laboratory at the University of Waterloo. Illustrated in Fig. 5.8 is a 6 mask process developed to construct the MEMS switches as well as the bias and interconnecting transmission lines on an Alumina wafer. The details of the fabrication steps and the processing conditions are presented in Appendix A.3.

The process begins with the deposition and patterning of a 300 nm layer of heavily phosphorous-doped hydrogenated amorphous silicon ($n^+$ a-Si:H) to form the bias lines and actuation pads. Mask 2 defines the opening in the silicon oxide (500 nm) layer deposited to passivate the bias lines. To construct the CPW lines, a thin layer of Cr/Au bilayer will be deposited which subsequently is used as the seed layer for the electroplating of a 1 $\mu$m-thick Au film inside a PR mold. Then, the seed layer will be quickly removed in a wet etching process. This method is employed to avoid the undercuts associated with the

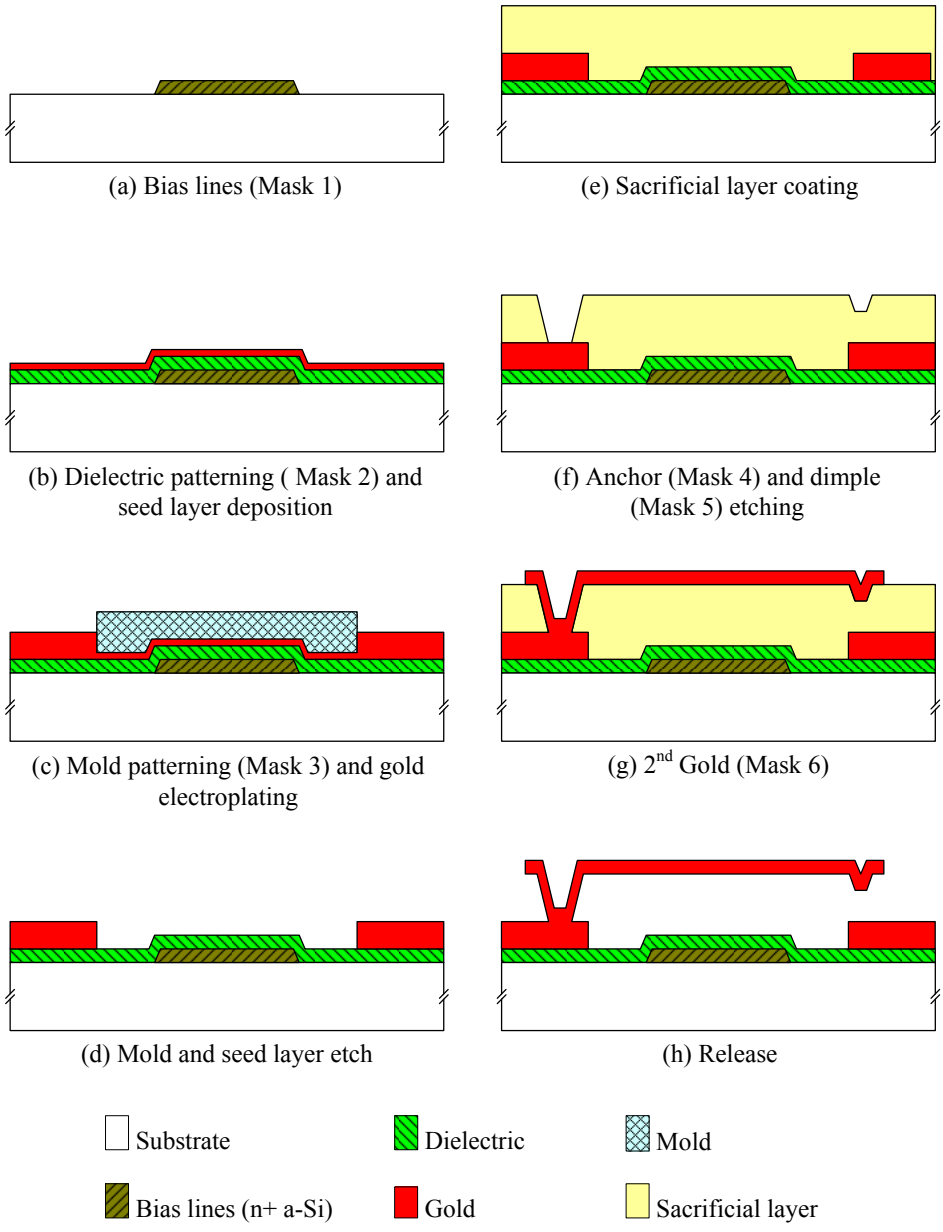


**Fig. 5.8: Fabrication sequence of the proposed devices viewed in the cross section of a MEMS switch.**

wet etching of gold layers and to provide better agreement with the dimensions of patterns and the designed values. To be able to perform high temperature annealing treatments before the release of the devices, polyimide (PI2562, HD Microsystems) is employed as the

sacrificial layer. The speed and time of the spin coating was adjusted to produce a 2.5 $\mu$m thick polyimide layer that specifies the initial air gap of the devices. Next, the polyimide is dry-etched in an RIE system to create the anchor and dimples of the cantilever using Mask 4 and Mask 5, respectively. The dimples (1 $\mu$m deep) are embedded in the structure of the MEMS switches to reduce the air gap at the contact points. As a result, the contact force is increased and the On-state resistance of the device is decreased. Finally, the electroplating of the second gold layer (1 $\mu$m thick) completes the structure of the signal crossovers and metal cantilever switches. Prior to release, the sample is annealed in $N_2$ ambient for 2 hrs at 380 °C to eliminate the stress gradient along the thickness of the top gold layer. The sacrificial layer is then removed in an inductively coupled oxygen plasma to release the MEMS elements. We found the generated plasmas in the parallel plate systems not suitable for the release process as the ion bombardment produces excessive heat that damages the MEMS devices.

Fig. 5.9 shows the SEM image of a fabricated 4 $\times$ 4 switch matrix, switching cell and one of the metal cantilever beams. For easy access to the bias lines, 200 $\times$ 200 $\mu m^2$ bias pads are placed on two sides of the matrix opposite to the input and output ports. However, in monolithic applications, smaller bias pads can be employed to reduce the total size of the matrix. The matrix measures 1.45 $\times$ 1.45 $\mu m^2$ in dimensions excluding the area consumed by the bias pads. The close-up SEM image of a contact type MEMS switch is shown in Fig. 5.9(c). The uniform air gap along the cantilever length suggests that the stress gradient over the thickness of the top gold layer has been eliminated by the pre-release annealing treatment. Moreover, the thickness of the cantilever over the sidewalls of the anchor and dimple is constant. If the step coverage of the deposited material is not sufficient especially in the anchor, the mechanical stability of the cantilever will be compromised.

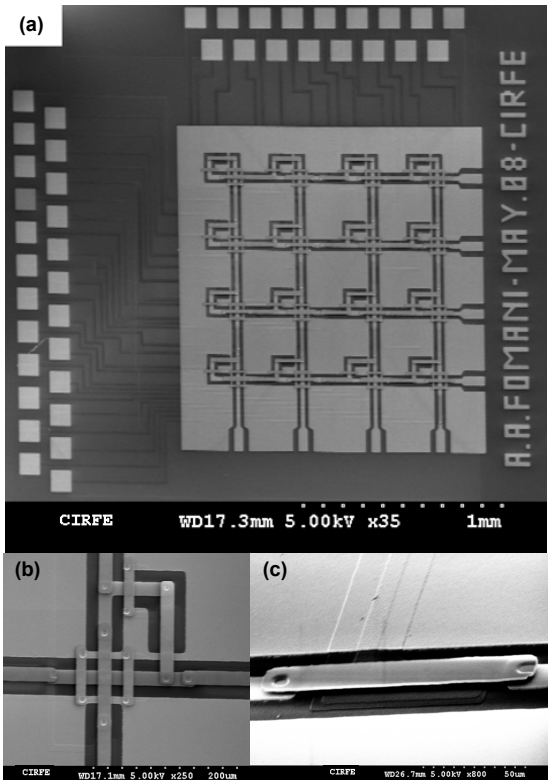


**Fig. 5.9: SEM micrographs of (a) a fabricated 4 × 4 monolithic RF switch matrix, (b) switching unit, and (c) typical cantilever beam contact switch.**

### 5.3.3 Characteristics

#### DC and RF performance

The fabricated 4 × 4 monolithic RF switch matrices illustrated in Fig. 5.9(a) consist of 41 SPST MEMS devices. The widths of the signal line ($S$) and gap to the ground ($G$) are designed to be 20 $\mu$m and 14 $\mu$m, respectively, to ensure a characteristic impedance of $\sim$ 50 $\Omega$ for the CPW transmission lines. The MEMS devices employ 125 $\mu$m-long cantilevers and 10 × 10 $\mu$m$^2$ dimples and anchors. The measured actuation voltage for 1 $\mu$m-thick gold beams is 65 – 75 V that is in good agreement with the CoventorWare simulation results

($\sim$ 60 V). The MEMS switches exhibit 0.2 – 0.3 $\Omega$ DC resistance at the holding voltage of 80 V measured using the four-point-probe technique. To facilitate the connection of the ports to the probes, single stage transitions were used to widen the transmission lines to $S$ = 45 $\mu$m and $G$ = 25 $\mu$m. The simulated return losses of the transitions are close to –20 dB at 40 GHz.

The RF response of the matrix was measured up to 40GHz using an Agilent 8722ES network analyzer connected to CPW probes with 150 $\mu$m signal to ground terminal spacing. As expected from the simulation results, the worst-case return loss is related to the farthest path, i.e. $S_{44}$, and that of the isolation comes from the two adjacent longest paths, $S_{38}$. Fig. 5.10 illustrates the measured RF performance of the matrix in the connection configuration

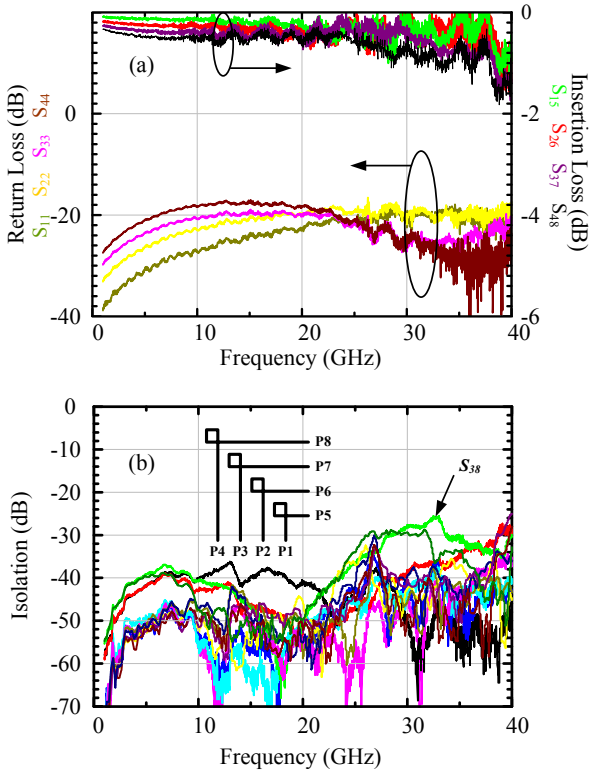


**Fig. 5.10: (a) Insertion and return losses of the 4 $\times$ 4 switch matrix. (b) Ports isolations in the connection configuration shown in the inset.**

shown in the inset of Fig. 5.10(b). To bias the circuit, the corresponding bias pads are connected using a wire bonder and the bias voltage is applied through a single DC probe. The worst-case for insertion and return losses of the device are respectively –17 dB and –1.8 dB up to 40 GHz. The circuit demonstrates a reasonable performance of better than –1 dB insertion loss below 30 GHz. As it will be presented later, the return loss deviates slightly from the designed value of –20 dB the worst-case scenario. It is believed that the fabrication tolerances can cause a shift in the dimension of the transmission lines, hence changing the characteristic impedance of the line. The transition sections also deteriorate the response and more complex transitions are required to improve the performance. A 3-stage transition with better than –32 dB return loss has been designed and will be integrated with the matrix in future attempts. As shown in Fig. 5.10(b), isolations better than 26 dB have been achieved between ports in the frequency range of DC to 40 GHz. Indeed, the system exhibits an excellent performance of more than 35 dB isolation below 20 GHz.

**Impact of bias network on switch matrix performance**

In the proposed MEMS switch matrix, a network of bias lines spreads under the RF signal paths to address the actuation pads of the MEMS elements. A thin dielectric layer covers the bias network to isolate them from the transmission lines. At the crossovers of bias and transmission lines, a parasitic signal path is created through the bias line from the signal to the ground. This loading effect can be modeled by an equivalent circuit consisting of a capacitance between signal to bias ($C_{sb}$) in series with the bias line resistance ($R_b$) and bias to the ground capacitance ($C_{bg}$). At very low frequencies, the impedance of the capacitances is much higher than the characteristic impedance ($Z_0$) of the transmission line. Hence, the signal coupling to the ground through the bias lines is negligible. At higher frequencies, the impedance of $C_{sb}$ and $C_{bg}$ will drop bellow $Z_0$ leaving a shunt

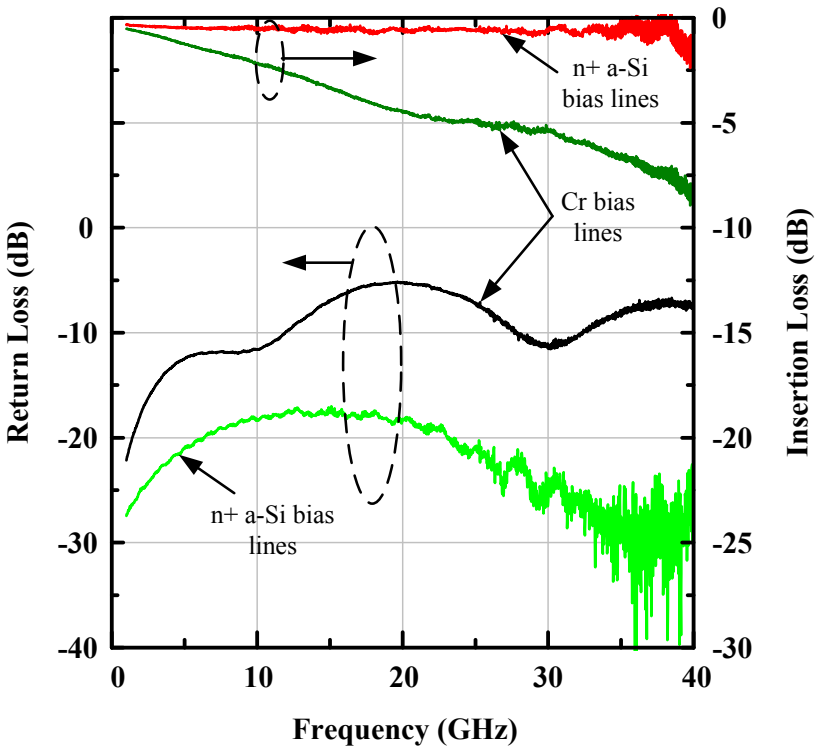


**Fig. 5.11: The worst-case insertion and return losses of 4 × 4 switch matrices with $n^+$ a-Si:H and Cr bias networks.**

impedance close to $R_b$ between the signal and ground. Consequently, the application of metals with low sheet resistances severely deteriorates the operation of this type of switch matrix configuration.

Fig. 5.11 depicts the worst-case return loss and isolation of a 4 × 4 switch matrix with Cr bias lines compared to the response of the fabricated system with an $n^+$ a-Si:H bias network. The former matrix demonstrates an acceptable response only at frequencies below 2 GHz. The application of the $n^+$ a-Si:H material for the bias lines and actuation pads of the MEMS devices extends the functionality of the system to frequencies above 40 GHz. As a matter of fact, the deposited $n^+$ a-Si:H layer (300 nm-thick) with the typical sheet resistance of 2 – 5 M$\Omega/square$ [136] appears transparent to the RF signal.

**Switching speed**

The experimental setup employed to measure the switching speed of the MEMS elements is illustrated in Fig. 5.12(a). To be able to change the operating state of the Device Under Test (DUT), the drain terminal of a high voltage transistor is connected to the bias pad of the device and at the same time through a pull-up resistor to the DC bias required for the actuation. A continuous wave RF signal at 2 GHz centre frequency with the power level of 20 dBm is sent to the input port of the switch using an HP8510 Synthesized Sweeper. The output port of the DUT is fed to a crystal detector (HP420A N-type Detector) that provides a negative DC voltage proportional to the power level of the signal in the frequency range of 0.1 – 12.5 GHz. The frequency and power level of the RF signal have been selected to avoid the degradation of the switch at high powers and maximize the dynamic range of the output signal from the detector. If a high to low voltage pulse (trigger signal) is applied to the gate of the transistor, the bias pad voltage changes from 0 to $V_{DD}$ and the DUT provides a signal path between the input and output ports. Therefore, the delay of the crystal detector signal from the falling edge of the trigger signal provides the turn-on time of the DUT.

The switching speed of the switching cell has been measured for the fabricated devices using Cr and $n^+$ a-Si:H bias lines. The former matrix demonstrates a 10.8 $\mu$s turn-on time while the later has a response time longer than 570 $\mu$s. This drastic difference in switching speed of the matrix is expected as the sheet resistance of $n^+$ a-Si:H is close to 5 orders of magnitude higher than Cr. Therefore, the RC delay between bias and the actuation pads is accordingly higher for the $n^+$ a-Si:H lines and the switching time is limited by the RC delay rather than the mechanical response of switches. It must be mentioned that in selecting the material for the bias network, a trade-off exists between the switching speed and RF performance of the matrix. The application of high resistive material improves the RF response while at the same time deteriorates the speed. However, a significant reduction in

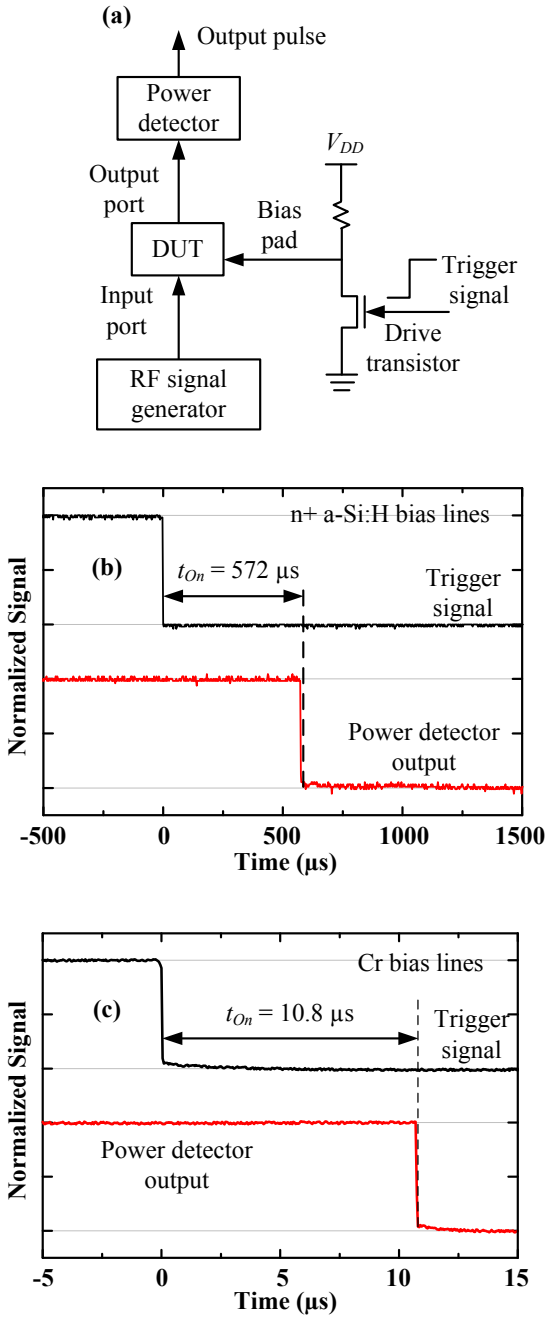


**Fig. 5.12: (a) The experimental setup for the switching speed measurements. The turn-on time, $t_{On}$, of the switching cell for the fabricated devices with (b) $n^+$ a-Si:H, and (c) Cr bias lines.**

the RC delay and a negligible loading effect on the RF signal for a 4 × 4 switch matrix are expected if heavily-doped hydrogenated micro-crystalline silicon ($n^+$ $\mu$c-Si:H) is employed as the material of choice for the bias network. The sheet resistance of $n^+$ $\mu$c-Si:H is in the range of 1 – 100 k$\Omega/square$ depending on the deposition conditions and thickness of the layer [137]. Hence, the bias lines with sheet resistance of $\sim$ 50 k$\Omega/square$ can be made of n+ $\mu$c-Si:H material to reduce the RC delay of the switching by a factor of 100. On the other hand, the bias lines exhibit more than 3 orders of magnitude higher resistance than the 50 Ω characteristic impedance of the transmission lines and consequently impose a negligible effect on the RF response.

## 5.4 Electrostatic-Actuated MEMS Switch Matrices for Low Frequency Applications

The switch matrix presented earlier employs 3 MEMS elements to provide a wide band operational frequency. In the stimulation and recording the neural activities, the bandwidth of the signal is in the 0 – 100 kHz frequency range. For these applications, the structure of the switch matrix can be simplified to only one MEMS element at the cross-section of the vertically running input and output terminals as shown in Fig. 5.3. The optical and SEM images of a 8 × 8 switch matrix comprised of 64 MEMS switches are shown in Fig. 5.13. The MEMS cantilevers are 125 $\mu$m × 25 $\mu$m in dimension with 15 × 15 $\mu m^2$ dimples and anchors. The fabrication process of these devices is similar to the monolithic RF MEMS switch matrices with Cr bias lines. The switching resistances of the fabricated devices were measured less than 0.5 Ω for several switching states of the matrix. Although the actuation voltage of these devices are fairly high (65 – 75 V), the small dimensions of the cantilever allows a high yield fabrication of these devices.

The large number of electrical connections that must be established between the micro-

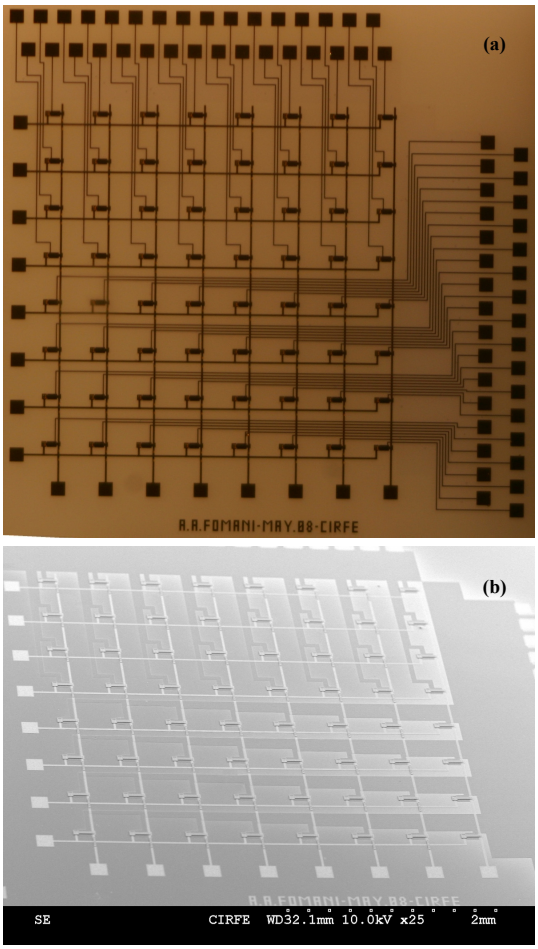


**Fig. 5.13: (a) Optical and (b) SEM images of an 8 × 8 low frequency MEMS switch matrix.**

controller and a MEMS switch matrix can severely undermine the reliability of the system. In the earlier presented MEMS circuits, for each switching unit, at least one bias line is required to control the switching state of the matrix. In Fig. 5.14, a 4 × 12 switch matrix is presented with a reduced number of the actuation pads. The switching cell of the system consists of 2 MEMS devices that must be actuated concurrently to route an input to the output port. A horizontal bias line addresses the actuation pads of the first MEMS element of the cells located in the same row while a vertical bias line connects the second MEMS element of the cells in the same column. Consequently, the number of the bias pads is

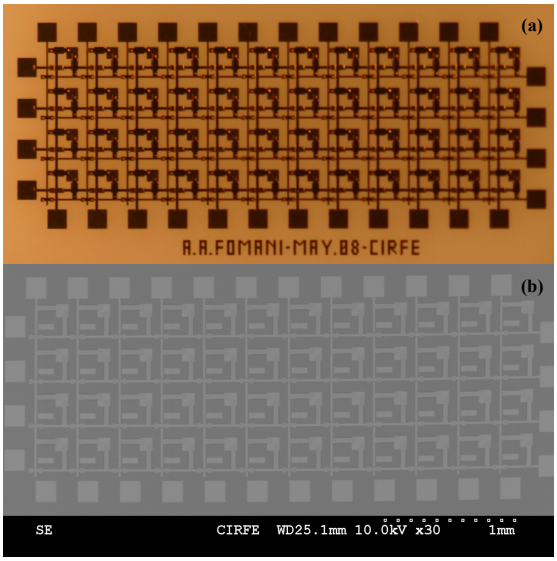


**Fig. 5.14: (a) Optical and (b) SEM images of a 4 $\times$ 12 low frequency MEMS switch matrix with 16 bias pads.**

reduced from 48 to 16 by employing this configuration for the switch matrix. However, the reduction in the number of bias pads was made possible at the cost of limiting the matrix's functionality. Indeed, at a certain time, only one of the input terminals can be connected to an output port. The switching resistance between different terminals of the matrix was measured to be less than 1.0 $\Omega$. The other characteristics of the switch matrix such as the actuation voltage and switching speed are in good agreement with the prior reported results due to the similar dimensions of the MEMS elements employed in different designs.

## 5.5 Magnetic-Actuated MEMS Switches

The electrostatic-actuated switches operate with extremely low powers and have simple structures that facilitate the fabrication of these devices. However, this category of switching elements demands high actuation voltages that degrade the lifetime of the device and induce mechanical instability. Moreover, the electrostatic force rapidly reduces with the

distance between the actuation electrodes; therefore, the large initial gaps demanded for the high Off-state isolations of RF MEMS switches cannot be produced. In the case of the electrothermal switches, the high power consumption and low switching speed severely limit the application. Alternatively, the actuation can be performed using electromagnetic force and the cantilever can be held in the Down-state by electrostatic force. The voltage required to maintain the device in the Down-state is substantially lower than the actuation voltage from Up-state as the distance between the cantilever and the actuation pad is reduced to only a fraction of the initial gap.

Here, electromagnetic-actuated switches are fabricated with an integrated current coil on the substrate as well as on the cantilever [138]. The substrate coil produces the magnetic field required for actuation and also acts as the holding electrode. A key advantage of the present design is the contribution of all the segments of the cantilever coil in the generation of the actuation force due to the presence of a perpendicular local magnetic field. In the previously reported devices [128, 129], the direction of external magnetic field is fixed and only segments along the width of the cantilever produce normal forces to the cantilever. The details of the fabrication process as well as the characteristics of the MEMS switches are reported in this section.

### 5.5.1 Structure and Design

A Three Dimensional (3D) schematic of the proposed switch is depicted in Fig. 5.15. The device consists of a metal coil (cantilever coil) that is integrated on top of a dielectric cantilever, and a contact bar at the tip of the beam to connect the input and output ports when the switch is turned On. Another coil (substrate coil) is integrated on the substrate to generate the required magnetic field for actuation. The substrate coil also acts as the holding electrode to maintain the cantilever in the Down position (On-state operation of

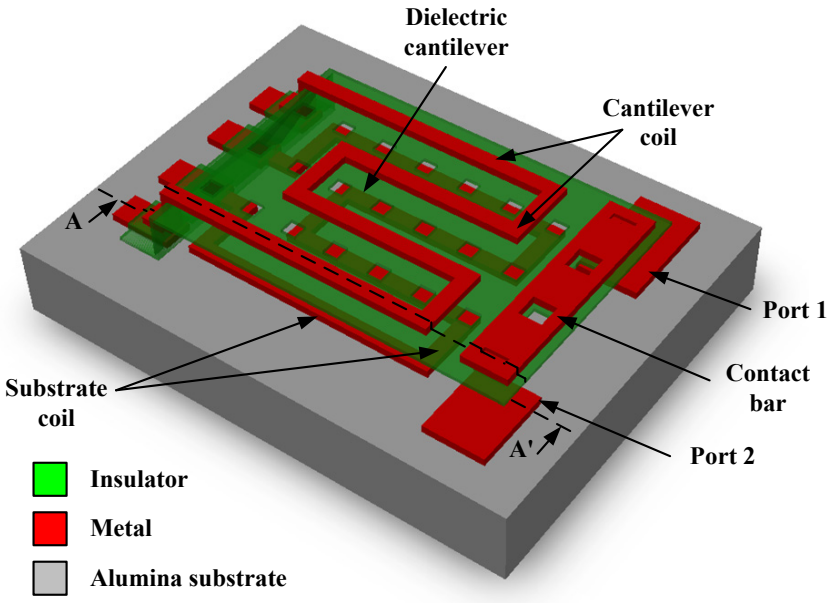


**Fig. 5.15: The 3D schematic of the proposed magnetic-actuated RF MEMS switch.**

the switch) using electrostatic force after the actuation of the device.

To actuate the device, a DC current is applied to the cantilever coil. In the presence of a magnetic field, a Lorentz force is exerted on this coil and transferred to the cantilever if the magnetic field is not parallel with the direction of the current. This magnetic field is generated by an applied current running through the substrate coil located just below the cantilever coil. With a good approximation, the field vector is perpendicular to the current and parallel with the plane of the beam; hence, the applied force is normal to the cantilever. If the current direction in the two coils is the same, the applied force will be attractive, pulling down the beam to turn on the switch. In this design, the field vector is perpendicular to each segment of the cantilever coil since it is mainly produced by the same section of the substrate coil. Therefore, the maximum possible force normal to the cantilever is generated. It is also possible to reverse the current in one of the coils to change the direction of the magnetic force and move the device into the Off-state.

The RF performance of the magnetic devices is expected to be superior to that of the

electrostatic switches. The device utilizes a dielectric cantilever that minimizes the signal coupling between the ports. In conventional metal contact type switches, one of the ports is connected to the metal cantilever whereas in our proposed design the contact bar is isolated from both ports. This is also beneficial in terms of the power handling as the self-actuation of the cantilever will be pushed to higher powers since the contact bar is not connected to the ports.

The RF characteristics of the switch in the On and Off-states of the operation have been simulated in HFSS. Fig. 5.16(a) illustrates the simulated insertion loss, return loss, and isolation of the device. The configurations and dimensions of the ports and the discontinuity in the transmission line are presented in Fig. 5.16(b).

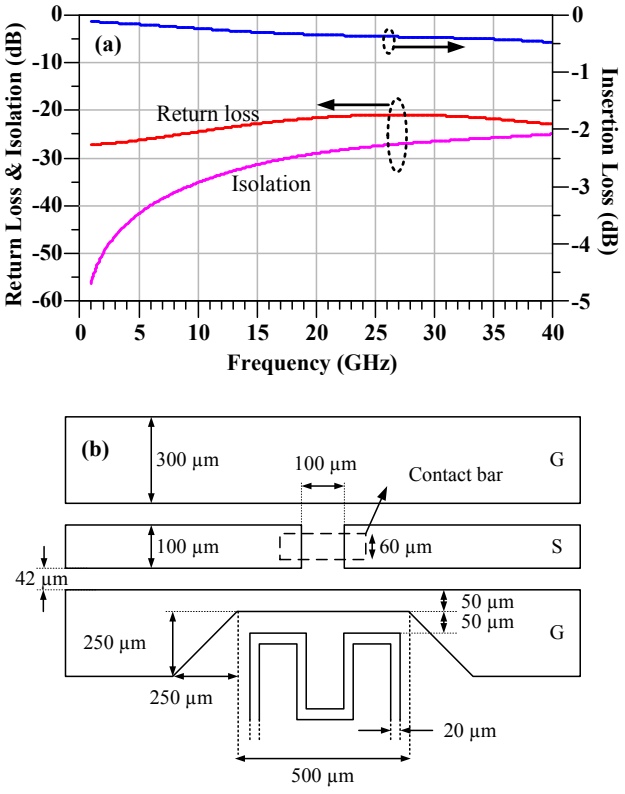


**Fig. 5.16: (a) The EM-simulated RF performance and (b) the configuration and dimensions of a magnetic-actuated MEMS switch.**

The input and output ports are Co-Planar Waveguide (CPW) transmission lines. The signal lines' width and gap to the ground are set to 100 $\mu$m and 42 $\mu$m respectively to achieve a 50 $\Omega$ characteristic impedance for the transmission line on a 635 $\mu$m-thick (25 mil) Alumina substrate ($\epsilon_r = 9.9$). The CPW topology has been considered for the device due to its smaller dimensions compared to other types of planar waveguides. The ground line under the cantilever has been narrowed to 50 $\mu$m in width to reduce the length of the cantilever. A 100 $\mu$m discontinuity in the signal line is embedded to achieve the minimum of 20 dB isolation between the ports for up to 40 GHz. The contact bar is 60 $\mu$m wide and has a 40 $\mu$m overlap with the signal lines. In the OFF-state the distance between the contact bar and the substrate is assumed to be 60 $\mu$m in accordance with the released cantilever. For low frequency applications, the ground conductor can be removed and the dimensions of the cantilever can be scaled to reduce the size of the MEMS switch.

### 5.5.2 Fabrication

The fabrication of magnetically actuated RF MEMS switches was carried out in the Centre for Integrated RF Engineering (CIRFE) laboratory at the University of Waterloo. Fig. 5.17 depicts the fabrication sequence of a typical device seen from the AA$'$ cross section in Fig. 5.15. The process requires only 4 lithographic steps compared to 7 masks previously employed to produce the magnetic switches [128]. The details of the fabrication steps and the processing conditions are presented in Appendix A.4

After an RCA cleaning of a 25 mil Alumina substrate, a thin layer of Cr/Au bilayer will be deposited as the seed layer for the electroplating of a 1 $\mu$m-thick Au film inside a PR mold to form the CPW lines, substrate coil and the bias pads. Although this method involves more processing steps than the wet etching of the deposited gold, the dimensions of the patterns are in better agreement with the designed values since there are no undercuts

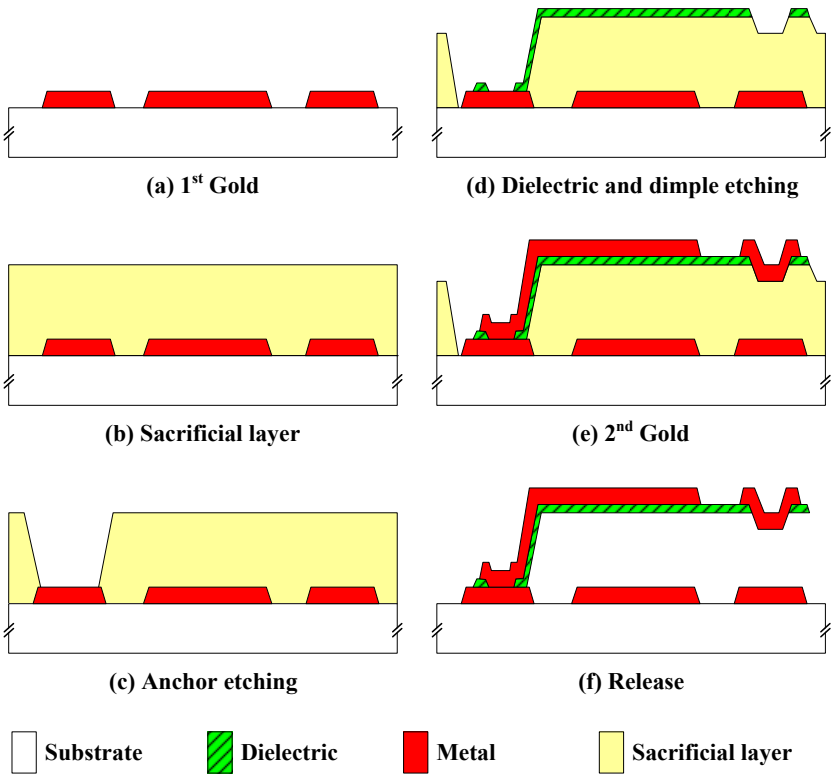


**Fig. 5.17: The fabrication sequence of the magnetic switches viewed in AA′ cross-section of Fig. 5.15.**

associated with etching of the layer. Then, the seed layer will be quickly removed in a wet etching process and a 5 $\mu$m-thick layer of polyimide (PI2611, HD Microsystems) is spin coated and cured as the sacrificial layer. The thickness of the polyimide film specifies the initial air gap of the fabricated devices. In the second photolithography step, the anchor of the cantilever is defined. The etching of the polyimide is performed in a Reactive Ion Etching (RIE) system in an oxygen plasma environment. Next, a 0.5 $\mu$m SiN dielectric is deposited in PECVD and patterned to form the cantilever. Subsequently, the cantilever is used as the mask to etch dimples in the sacrificial layer. The dimples reduce the air gap at the contact points in order to increase the contact force, and consequently, decrease the On-state resistance of the device. To complete the structure of the switches, a second

gold layer with the thickness of 1 $\mu$m is electroplated to produce the cantilever coil and the contact bar. Finally, the sacrificial layer is removed in a dry etching process to release the MEMS devices.

In this design, there is no need for an insulator layer to cover the substrate coil. The cantilever coil is located on top of the dielectric cantilever therefore isolated from the substrate coil when the switch collapses to the Down-state. The contact bar is also placed on top of the dielectric cantilever and extended below the beam through via holes over the contact regions. This will eliminate the demand for deposition and patterning of a metal layer to create the contact bar underneath the cantilever. Moreover, the dimples are self aligned with the contact holes of the cantilever since the cantilever itself serves as the mask to produce the dimples. This significantly simplifies the fabrication process.

Fig. 5.18 shows the SEM image of a released device utilizing a cantilever with dimensions of 530 $\mu$m and 500 $\mu$m in length and width, respectively. A matrix of holes etched through the cantilever facilitates the release process by providing access to the sacrificial layer. Less than 3 hours of Inductively Coupled Plasma (ICP) at 20 mTorr pressure and 300 W of power is sufficient for the complete release of the devices.

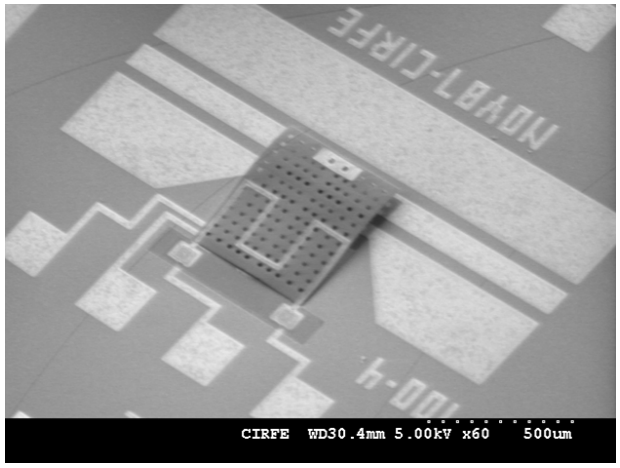


**Fig. 5.18: SEM image of a fabricated magnetic switch.**

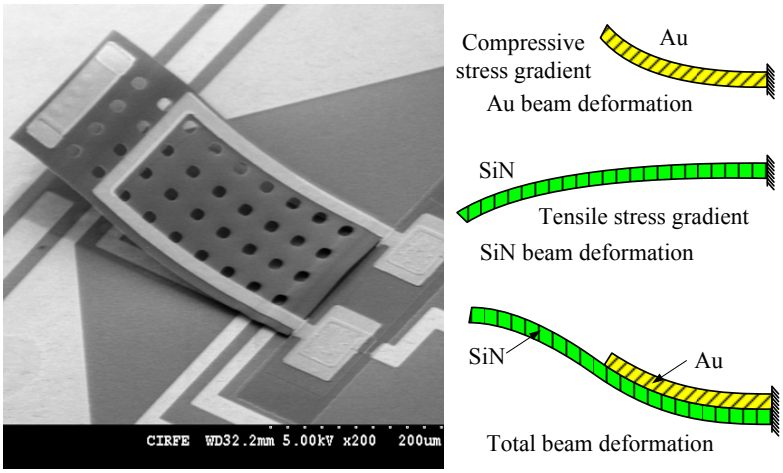


**Fig. 5.19: Suggested stress profile in gold, SiN, and stacked cantilevers (right). SEM image of a switch with a single turn cantilever coil (left).**

The presence of stress gradient in the metal and dielectric layers deforms the structure. The deformed shape of the cantilevers suggests that metal has a tensile stress gradient across the film thickness, and the SiN material suffers from the compressive stress profile. This can be easily deduced from the SEM image of a switch utilizing a single turn cantilever coil in Fig. 5.19. To confirm the stress profile of the SiN material, the cantilever coils of several switches were removed in a wet etching solution prior to the release of the device. The collapse of the dielectric cantilevers to the substrate was observed in the SEM images as a result of the tensile stress gradient in the SiN material.

### 5.5.3 Characteristics

#### Actuation

The deflection of several cantilevers as a function of the applied current to the actuation coils has been measured employing a Veeco WYKO NT1100 optical profiler. The measurement setup is shown in Fig. 5.20(a) consisting of an optical profiler, current source,

vibration isolation table, and a positioning stage. For the experiments, the two bias pads in the middle (see Fig. 5.18) are shorted using a wire bonder and a constant current is applied between the outer pads. This ensures the flow of equal magnitude unidirectional currents through both coils. At each bias point, the cantilever profile is obtained using the optical profiler and the height of the contact bar from the substrate is extracted from the result. Fig. 5.20(b) presents the displacement of the contact bar located at the tip of the cantilever shown in Fig. 5.19 as a function of equal magnitude unidirectional currents

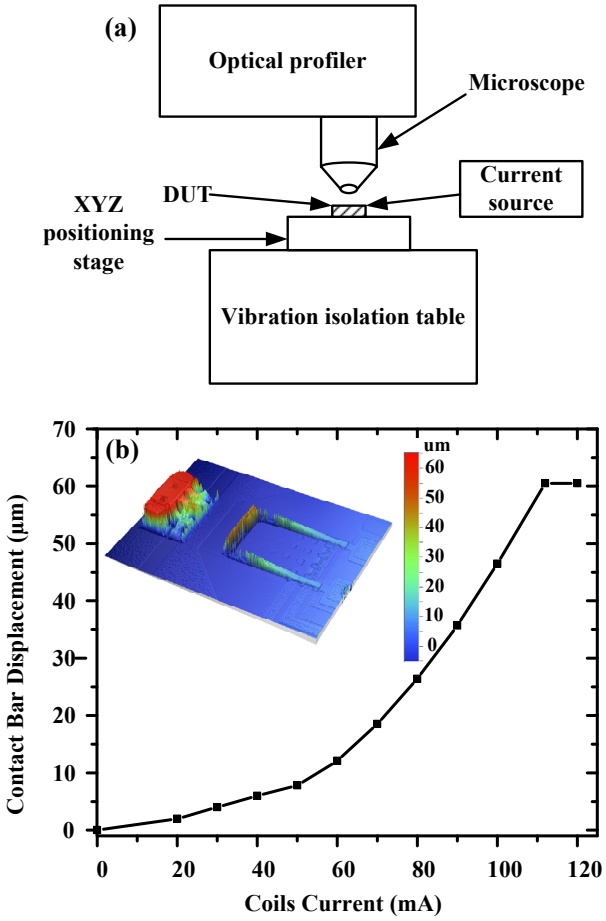


**Fig. 5.20: (a) The experimental setup employed in the measurement of the cantilever deflection. (b) The displacement of the cantilever tip vs. the actuation coil currents. The inset shows the optical profile of a cantilever with a single-turn coil.**

applied to the coils. An example of the optical profile of the cantilever for the actuation current of 20 mA is illustrated in the inset of Fig. 5.20(b). It must be mentioned that flow of currents as high as 150 mA in the cantilever coil induces no change in the shape of the cantilever when the substrate coil does not carry a current. Therefore, the possibility of thermal actuation of the cantilever due to heat generation in the top coil is ruled out.

When unidirectional currents flow in the cantilever and substrate coils, an electromagnetic force is applied to the cantilever. The actuation force can be approximated by

$$F_{act} = I_c l \times B, \tag{5.1}$$

where, $I_c$, $l$, and $B$ are the current, total length, and the magnetic field experienced at each section of the cantilever coil, respectively. If the air gap is small relative to the spacing between the coils, the magnetic field seen by each section of the cantilever coil is mainly produced by the same section in the substrate coil. Hence, the magnetic field is perpendicular to the current, and the actuation force is normal to the cantilever. Moreover, $B$ is proportional to the substrate coil current, $I_s$, and an inverse function of the coil width, $w$,

$$B = \mu_0 I_s / w. \tag{5.2}$$

At equilibrium, the actuation force is equal to the opposing force arising from the spring constant, k, of the cantilever

$$F_{act} = k(g_0 - g). \tag{5.3}$$

By substituting 5.1 and 5.2 into 5.3, the deflection of the cantilever from the initial height, $g_0$ is expressed as

$$d = g_0 - g = \frac{\mu_0 I_s I_c l}{kw}. \tag{5.4}$$

This equation defines the actuation condition as

$$I_c I_s > \frac{k g_0 w}{\mu_0 l}. \tag{5.5}$$

It is important to note that for any arbitrary displacement, it is possible to find the actuation currents which satisfy 5.4. Therefore, the impact force transferred to the cantilever when the switch goes to Off-state can be minimized by choosing the coil currents slightly above the actuation condition described in 5.5. However, in the case of electrostatic switches, the solution to the height of the cantilever results in a stable position up to approximately $g_0/3$ and then a complete collapse to the substrate. Consequently, both the cantilever and the dielectric covering the actuating electrode are subjected to a substantially large impact force compared to what is needed to achieve a low contact resistance [53]. This impact force can induce mechanical instability of the cantilever over time as well as creation of cracks and defects in the insulator.

### DC and RF Performance

The RF characteristics of the fabricated switches were measured using a 130 mA unidirectional actuation current applied to the coils of a device shown in Fig. 5.18. After the actuation, it is possible to hold the cantilever in the Down-state using a $\sim$ 24 V voltage difference between the coils. The electrostatic actuation of the devices is also possible by the application of $\sim$ 55 V. The devices exhibit a 0.5 – 0.6 $\Omega$ contact resistance at the holding voltage of 40 V measured using four point probe technique. The $S$-parameters of the fabricated RF MEMS switches have been measured using an Agilent 8722ES network analyzer connected to CPW probes with a 150 $\mu$m signal to ground terminal spacing. Fig. 5.21(a) illustrates the measured RF characteristics in the On-state of operation for a switch with a similar design of the device shown in the SEM image of Fig. 5.18. The insertion

and return losses are lower than –0.3 dB and –24 dB, respectively, at 10 GHz. The device also demonstrates a quite reasonable performance up to 40 GHz with a worst-case return and insertion losses of –0.8 dB and –18 dB. Moreover, the measured results are in good agreement with the EM simulation results presented in Fig. 5.16. The slight discrepancy between the curves is due to deviation in geometries of the device because of the fabrication tolerance.

In the Off-state operation, the contact bar is separated from the signal lines, therefore the input port is isolated from the output. Fig. 5.21(b) shows the measured isolation of the same switch used in On-state measurements. The device exhibits excellent isolation of more than 34 dB at 10 GHz. The worst-case isolation of the switch for the frequency range of DC to 40 GHz is also better than 24 dB.

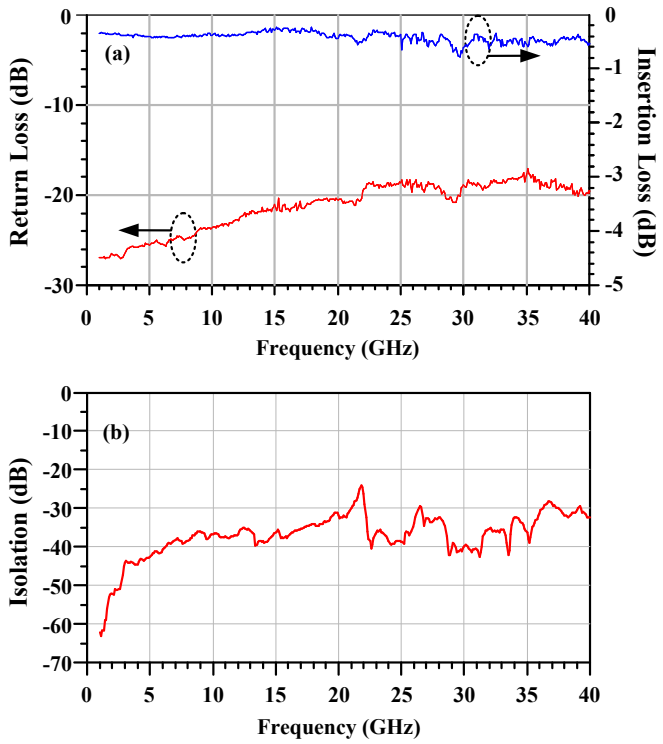


**Fig. 5.21: The measured RF characteristics of the fabricated magnetic-actuated switch in the (a) On-state and (b) Off-state of operation.**

## 5.6 Summary

The fabrication, design, and characteristics of MEMS switches and switching matrices have been discussed in this chapter. An electrostatic-actuated 4 × 4 switch matrix employing high resistive $n^+$ a-Si:H bias lines were presented providing an excellent RF performance up to 40 GHz. Miniature 8 × 8 and 4 × 12 switch matrices were also reported for low frequency applications. The MEMS switching elements operate at actuation voltages of 65 – 75 V and offer response times faster than 11 $\mu$s and On-resistances lower than 0.5 $\Omega$.

To enhance the reliability of the MEMS elements, actuation based on electromagnetic force was proposed. Fully integrated magnetically-actuated dielectric cantilever MEMS switches were developed offering current coils on the substrate and on top of the cantilever. The device is actuated by applying a unidirectional current to the coils, and is maintained at the Down-state by employing a potential difference between the coils. The actuation current and holding voltage are measured to be as low as 110 mA and 24 V, respectively. The holding voltage is substantially smaller than the actuation voltage of electrostatic actuated devices with similar initial gaps. Moreover, it is possible to force these devices into the Up-state using a repulsive electromagnetic force in the case of release failure.

Despite the superior characteristics, issues such as reliability, fabrication yield, large number of bias pads, and high actuation voltages prevent the application of MEMS switch matrices in neuroprosthetics systems. Nevertheless, the low On resistance of the circuits and the possibility for integration with neural microprobes is attractive for futuristic applications.

# Chapter 6

# Conclusions and Future Work

Novel generations of neural microprobes were developed in this doctoral study to enhance the functionality of neuroprosthetics systems [91, 92, 110, 111]. This work concentrates on the fabrication and characterization of chronically implantable microprobes for intracortical and DBS applications. For neurological research and treatments, multisite 3D microprobes capable of both stimulation and recording are demanded. These microprobes must be rigid enough to penetrate inside the tissue while integrated with flexible interconnection cables. In addition, the DBS implants must be capable of adjusting the distribution of the injected charge inside the tissue to enhance the efficacy of the treatment. Here, the most significant contributions of this research are summarized.

- A new method of fabrication was developed to produce intracortical microprobes with improved structural design [91, 92]. These devices are integrated with 2 cm-long flexible interconnection cables and provide adequate mechanical strength for penetration into the tissue. Gold micro-needles are embedded in the probe shanks to locally reinforce the implants. These microprobes offer an array of electrodes with 32 recording channels located on 4 parallel shanks with 2, 4, and 8 mm lengths. The functionality and characteristic stability of the fabricated microprobes was confirmed in acidic and saline solutions. The periodic field potential activity from an intact

mouse hippocampus was successfully recorded using a fabricated device.

- Novel Three Dimensional (3D) multi channel microprobes were presented for Deep Brain Stimulation (DBS) and recording [110, 111]. These microprobes offer independent electrode sites around the shaft of the implant providing the capability to control the profile of the injected charge into the tissue. The devices are comprised of planar flexible microprobes assembled or folded over cylindrical poly-urethane shafts with diameters as low as 750 $\mu$m. A dramatic enhancement in the density/number of the channels and a precise control over the dimensions of the electrode sites were achieved. The fabricated devices host 16 stimulating and 16 recording channels. The low impedance characteristics and long term behavior of the Au and Ir electrodes were demonstrated in acidic and saline solutions. The in-vitro experiments in a whole hippocampus of a C57BL/6 mouse confirmed the potential application of fabricated microprobes in simultaneous neural stimulation and recording.

In this work, the possibility of employing MEMS switches for the construction of a site selection matrix integrated with the neural microprobe was explored. Significant progress has been made in the development of high yield MEMS fabrication processes. A $4 \times 4$ monolithic RF MEMS switch matrix with exceptional RF performance and miniature dimensions was reported [98,135]. An $8 \times 8$ and a $4 \times 12$ matrix were successfully fabricated for low frequency applications. To enhance the reliability of operation, a fully integrated magnetic-actuated RF MEMS switch was proposed, fabricated, and characterized [138]. Although, the reliability and fabrication issues are of severe concern, the excellent switching properties of these matrices may be utilized to advance the functionality of future neuroprosthetics systems.

# Future Work

Despite the extensive research carried throughout this study, many unexplored and unresolved issues still remain concerning the reliability and operation of neural microprobes. A compact summary of such issues and the recommended solutions are summarized here.

- The intracortical microprobes presented in chapter 3 may be affected by the humidity absorption in the polyimide structural layer. The impact can be the reduction in the electrical isolation between the adjacent channels and also the delamination of the electrodes from the microprobe. However, the developed methodology and approach is applicable to other types of spin-coated polymers with higher resistivity against moisture intake. Polymers such as polyurethane and PDMS along with PECVD-deposited dielectrics may be employed to enhance the stability of these devices.

- 3D arrays of intracortical electrodes must be developed based on the proposed flexible microprobes. A possible configuration for such an array is shown in Fig. 6.1. The

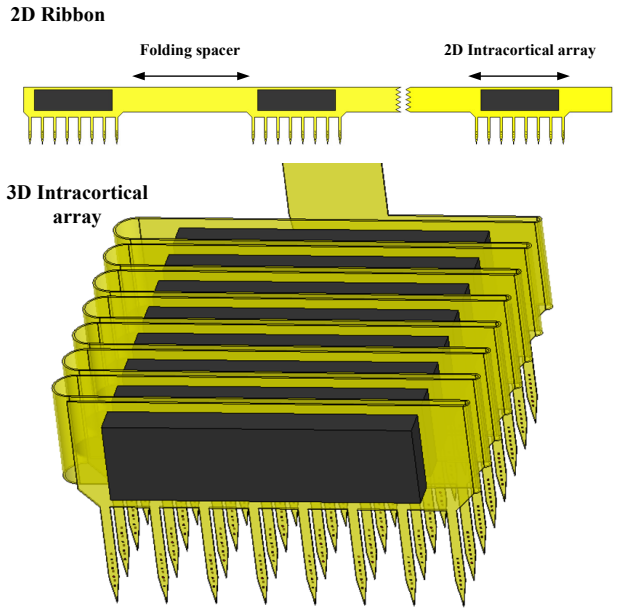


**Fig. 6.1: The possible configuration of a 3D intracortical array.**

array includes several microprobes stacked together and connected to the outside circuitry using a single flexible interconnection cable. Several low noise amplifiers and multiplexer circuits can be bonded to individual microprobes to enhance the signal to noise ratio of the recording and to reduce the number of conductors in the interconnection cable.

- The thin film planar devices employed in the fabrication of DBS microprobes may also be susceptible to moisture absorption and ionic diffusion. Polyurethane can be used as the structural layer of these devices to extend the lifetime of the implant and to improve the bonding strength to the shaft. Long-term accelerated stability tests at elevated temperatures are required to confirm the durability of these devices in biological environments for several years. The safe voltage range of the stimulation must be also determined and the dimensions of the electrode sites must be optimized based on the shape of the targeted tissue.

- Further research to improve the reliability, enhance the yield of fabrication, and reduce the actuation voltages / currents of the MEMS switching elements is demanded. Progress in packaging and interfacing methods is required for the integration of MEMS switch matrices with neural microprobes.

# Appendix A

# Fabrication Sequence and Processing Conditions

The following sections provide the fabrication sequence and the processing conditions developed to construct the neural microprobes and MEMS switching systems presented in this thesis.

## A.1 Process Flow of the Intracortical Microprobes

The processing conditions and the details of the fabrication steps illustrated in Fig. 3.3 for the construction of the proposed intracortical microprobes are as follows:

1. **Substrate Cleaning**
   Cleaning Process: RCA 1
   Hot Wash: 15 min

2. **Sacrificial Layer:**
   **Mo Sputtering**
   Pressure: 10 mTorr

Sputtering Gas: Ar

Plasma Source: DC

Power Density: 1.3 W/cm$^2$

Deposition Rate: 1.6 $\mathring{A}$/s

Thickness: 500 nm

or

**Cr E-beam Evaporation**

Base Pressure: $< 10^{-6}$ Torr

Beam Voltage: 5 kV

Deposition Rate: 3 $\mathring{A}$/s

Thickness: 500 nm

3. **Structural Layer: PI Coating**

   PI 2611 Coating

   Spin Speed: 5000 rpm

   Spin Duration: 1 min

   Bake 1: 2 min at 90 °C

   Bake 2: 2 min at 150 °C

   Cure: 30 min at 350 °C

   Thickness: 3 $\mu$m

4. **Electroplating Seed Layer: Au E-beam Evaporation**

   Base Pressure: $< 10^{-6}$ Torr

   Beam Voltage: 5 kV

   Deposition Rate: 10 $\mathring{A}$/s

   Thickness: 100 nm

5. **Electroplating Mold: PI Coating**

   PI 2611 Coating

Spin Speed: 1500 rpm

Spin Duration: 1 min

Bake 1: 2 min at 90 °C

Bake 2: 2 min at 150 °C

Second Coating

Process Conditions: similar to the first step

Cure: 60 min at 350 °C

Thickness: 18 $\mu$m

6. **Electroplating Mold: Al Sputtering**

   Pressure: 3.5 mTorr

   Sputtering Gas: Ar

   Plasma Source: DC

   Power Density: 2.7 W/cm$^2$

   Deposition Rate: 3 $\mathring{A}$/s

   Thickness: 300 nm

7. **Electroplating Mold: Mask 1**

   AZ3330 Coating

   Spin Speed: 3000 rpm

   Spin Duration: 1 min

   Softbake: 3 min at 90 °C

   Exposure Time: 15 s (UV Intensity: 40 mW/cm$^2$)

   Post Exposure Bake: 2 min at 90 °C

   Development Time: 45 – 60 s

   Hardbake: 2 min at 110 °C

8. **Electroplating Mold: Al Etching**

   Etchant: PAN at 40 °C

Etching Time: 80 – 100 s

9. **Electroplating Mold: PI RIE Etching**

   First RIE Etching:

   Pressure: 20 mTorr

   Gases and Flow Rates: $O_2$ 18 SCCM and $CF_4$ 2 SCCM

   RIE Power Density: 0.39 W/cm$^2$

   ICP Power Density: 0.39 W/cm$^2$

   Time: 1800 s

   EKC Rinse: 3 min

   IPA Rinse: 10 min

   Second RIE Etching:

   Process Conditions: similar to the first step

   Time: 300 s

   EKC Rinse: 3 min

   IPA Rinse: 10 min

10. **Electroplating Mold: Al Etching**

    Process Conditions: similar to the previous Al etching step

    Etching Time: 90 s

11. **Reinforcement Micro-Needles: Au Electroplating**

    Solution: Techni-Gold 434, Technic Inc.

    Current Density: 2.2 mA/cm$^2$

    Plating Rate: 16 – 18 $\mathring{A}$/s

12. **Reinforcement Micro-Needles: Planarization**

    Step 1: Diamond Lapping Film (UltraPrep, Buehler) 6 $\mu$m Abrasive Particles

    Step 2: Diamond Lapping Film (UltraPrep, Buehler) 1 $\mu$m Abrasive Particles

13. **Structural Layer: PI Coating**

    Process Conditions: similar to the first PI coating step

14. **Electrodes: Ti / Au / Ti E-beam Evaporation**

    Ti Deposition:

    Base Pressure: $< 10^{-6}$ Torr

    Beam Voltage: 5 kV

    Deposition Rate: 1.0 $\mathring{A}$/s

    Thickness: 20 nm

    Au Deposition:

    Deposition Conditions: similar to the previous Au deposition step

    Thickness: 300 nm

    Ti Deposition:

    Process Conditions: similar to the previous Ti deposition step

    Thickness: 20 nm

15. **Electrodes: Mask 2**

    AZ3312 Coating

    Spin Speed: 4000 rpm

    Spin Duration: 1 min

    Softbake: 1 min at 90 °C

    Exposure Time: 8 s (UV Intensity: 40 mW/cm$^2$)

    Development Time: 45 – 60 s

    Hardbake: 1 min at 110 °C

16. **Electrodes: Metal Etching**

    Ti RIE Etching:

    Pressure: 20 mTorr

    Gases and Flow Rates: Ar 20 SCCM

RIE Power Density: 0.4 W/cm$^2$

Etching Time: 60 s

Au Etching:

Etchant: Gold Etchant TFA, Transene Company Inc. at Room Temperature

Etching Time: 40 – 50 s

Ti RIE Etching:

Process Conditions: similar to the previous Ti etching step

Etching Time: 60 s

17. **Electrodes: Photoresist Removal**

    Solution: AZ KWIK Strip Remover at 60 °C

    Time: 30 min

18. **Structural Layer: PI Coating**

    Process Conditions: similar to the first PI coating step

19. **Structural Layer Patterning: Al Sputtering**

    Process Conditions: similar to the previous Al sputtering step

    Thickness: 300 nm

20. **Structural Layer Patterning: Mask 3**

    AZ3330 Coating

    Process Conditions: similar to the previous AZ3330 patterning step

21. **Structural Layer Patterning: Al Etching**

    Process Conditions: similar to the previous Al etching steps

    Etching Time: 90s

22. **Structural Layer Patterning: PI RIE Etching**

    First RIE Etching:

Process Conditions: similar to the PI Mold etching step

Time: 1800 s

EKC Rinse: 3 min

IPA Rinse: 10 min

Second RIE Etching:

Time: 300 s

EKC Rinse: 3 min

IPA Rinse: 10 min

23. **Structural Layer Patterning: Electroplating Seed Layer Etching**

    Process Conditions: similar to the previous Au etching step

    Etching Time: 15 – 20 s

24. **Structural Layer Patterning: PI RIE Etching**

    Process Conditions: similar to the PI Mold etching step

    Time: 600 s

    EKC Rinse: 3 min

    IPA Rinse: 10 min

25. **Electrodes Preparation: Ti RIE Etching**

    Process Conditions: similar to the previous Ti etching steps

    Etching Time: 60 s

26. **Release: Al Mask Etching**

    Process Conditions: similar to the previous Al etching steps

    Etching Time: 3 min

27. **Release: Sacrificial Layer Etching**

    Mo Sacrificial Layer:

    Etchant: PAN at 40 °C

Etching Time: 24 – 48 hrs

or

Cr Sacrificial Layer:

Etchant: CRE-473 Chromium Etch, Transene Company Inc., at 40 °C

Etching Time: 48 – 72 hrs

28. **Microprobe Cleaning**

    IPA Rinse: 10 min for 3 times

    DI Water Rinse

## A.2 Process Flow of the Thin Film Planar Microprobes

The processing conditions and the details of the fabrication steps illustrated in Fig. 4.3 for the construction of the proposed thin film planar microprobes are as follows:

1. **Substrate Cleaning**

    Cleaning Process: RCA 1

    Hot Wash: 15 min

2. **Sacrificial Layer: Cr E-beam Evaporation**

    Base Pressure: $< 10^{-6}$ Torr

    Beam Voltage: 5 kV

    Deposition Rate: 3 $\mathring{A}$/s

    Thickness: 500 nm

3. **Structural Layer: PI Coating**

    PI 2611 Coating

Spin Speed: 4000 rpm

Spin Duration: 1 min

Bake 1: 2 min at 90 °C

Bake 2: 2 min at 150 °C

Cure: 30 min at 350 °C

Thickness: 4 $\mu$m

4. **Electrodes: Au E-beam Evaporation**

   Base Pressure: $< 10^{-6}$ Torr

   Beam Voltage: 5 kV

   Deposition Rate: 10 $\mathring{A}$/s

   Thickness: 250 nm

5. **Electrodes: Mask 1**

   AZ3312 Coating

   Spin Speed: 4000 rpm

   Spin Duration: 1 min

   Softbake: 1 min at 90 °C

   Exposure Time: 8 s (UV Intensity: 40 mW/cm$^2$)

   Development Time: 45 – 60 s

   Hardbake: 1 min at 110 °C

6. **Electrodes: Au Etching**

   Etchant: Gold Etchant TFA, Transene Company Inc. at room Temperature

   Etching Time: 40 – 50 s

7. **Electrodes: Photoresist Removal**

   Solution: AZ KWIK Strip Remover at 60 °C

   Time: 30 min

8. **Structural Layer: PI Coating**

   Process Conditions: similar to the previous PI coating step

9. **Structural Layer Patterning: Al Sputtering**

   Pressure: 3.5 mTorr

   Sputtering Gas: Ar

   Plasma Source: DC

   Power Density: 2.7 W/cm$^2$

   Deposition Rate: 3 $\mathring{A}$/s

   Thickness: 300 nm

10. **Structural Layer Patterning: Mask 2**

    AZ3330 Coating

    Spin Speed: 3000 rpm

    Spin Duration: 1 min

    Softbake: 3 min at 90 °C

    Exposure Time: 15 s (UV Intensity: 40 mW/cm$^2$)

    Post Exposure Bake: 2 min at 90 °C

    Development Time: 45 – 60 s

    Hardbake: 2 min at 110 °C

11. **Structural Layer Patterning: Al Etching**

    Etchant: PAN at 40 °C

    Etching Time: 80 – 100 s

12. **Structural Layer Patterning: PI RIE Etching**

    Pressure: 20 mTorr

    Gases and Flow Rates: $O_2$ 18 SCCM and $CF_4$ 2 SCCM

    RIE Power Density: 0.39 W/cm$^2$

ICP Power Density: 0.39 W/cm$^2$

Time: 900 s

EKC Rinse: 3 min

IPA Rinse: 10 min

13. **Release: Al Mask Etching**

    Process Conditions: similar to the previous Al etching step

    Etching Time: 3 min

14. **Release: Sacrificial Layer Etching**

    Etchant: CRE-473 Chromium Etch, Transene Company Inc., at 40 °C

    Etching Time: 48 – 72 hrs

15. **Microprobe Cleaning**

    IPA Rinse: 10 min for 3 times

    DI Water Rinse

## A.3 Process Flow of the Monolithic MEMS Switch Matrices

The processing conditions and the details of the fabrication steps illustrated in Fig. 5.8 for the construction of the proposed monolithic MEMS switch matrices are as follows:

1. **Substrate Cleaning**

    Cleaning Process: RCA 1

    Hot Wash: 15 min

2. **Bias Lines: $n^+$a-Si:H Deposition**

   Pressure: 150 mTorr

   Deposition Temperature: 260 °C

   Gases and Flow Rates: $SiH_4$(1% $PH_3$) 20 SCCM

   Plasma Source: 13.56 MHz

   Power Density: 11 mW/cm$^2$

   Deposition Rate: 2.5 $\mathring{A}$/s

   Thickness: 300 nm

3. **Bias Lines: Mask 1**

   AZ3330 Coating

   Spin Speed: 3000 rpm

   Spin Duration: 1 min

   Softbake: 3 min at 90 °C

   Exposure Time: 15 s (UV Intensity: 40 mW/cm$^2$)

   Post Exposure Bake: 2 min at 90 °C

   Development Time: 45 – 60 s

   Hardbake: 2 min at 110 °C

4. **Bias Lines: $n^+$a-Si:H RIE Etching**

   Pressure: 250 mTorr

   Gases and Flow Rates: $CF_4$ 30 SCCM

   RIE Power Density: 0.20 W/cm$^2$

   ICP Power Density: 0.20 W/cm$^2$

   Time: 300 – 360 s

5. **Bias Lines: Photoresist Ashing**

   Pressure: 20 mTorr

   Gases and Flow Rates: $O_2$ 20 SCCM

RIE Power Density: 0.20 W/cm$^2$

ICP Power Density: 0.20 W/cm$^2$

Time: 200 s

6. **Dielectric: $SiO_x$ Deposition**

   Pressure: 900 mTorr

   Deposition Temperature: 250 °C

   Gases and Flow Rates: $SiH_4$ 20 SCCM, $N_2$ 118 SCCM, and $N_2O$ 140 SCCM

   Plasma Source: 10 kHz

   Power Density: 0.33 W/cm$^2$

   Deposition Rate: 9.1 $\mathring{A}$/s

   Thickness: 500 nm

7. **Dielectric: Mask 2**

   AZ3330 Coating

   Process Conditions: similar to the previous AZ3330 patterning step

8. **Dielectric: $SiO_x$ RIE Etching**

   Pressure: 250 mTorr

   Gases and Flow Rates: $CF_4$ 30 SCCM

   RIE Power Density: 0.20 W/cm$^2$

   ICP Power Density: 0.39 W/cm$^2$

   Etching Time: 500 – 530 s

9. **Dielectric: Photoresist Ashing**

   Process Conditions: similar to the previous photoresist ashing step

   Time: 200 s

10. **Metal 1: Electroplating Seed Layer Deposition**

    Cr E-beam Evaporation:

Base Pressure: $< 10^{-6}$ Torr

Beam Voltage: 5 kV

Deposition Rate: 3.0 $\mathring{A}$/s

Thickness: 30 nm

Au E-beam Evaporation:

Base Pressure: $< 10^{-6}$ Torr

Beam Voltage: 5 kV

Deposition Rate: 10 $\mathring{A}$/s

Thickness: 100 nm

11. **Metal 1: Mold Patterning (Mask 3)**

    AZ nLof 2035 Coating

    Spin Speed: 4000 rpm

    Spin Duration: 1 min

    Softbake: 1 min at 110 °C

    Exposure Time: 15 s (UV Intensity: 40 mW/cm$^2$)

    Post Exposure Bake: 1 min at 110 °C

    Development Time: 135 – 150 s

    Hardbake: 1 min at 110 °C

12. **Metal 1: Au Electroplating**

    Solution: Techni-Gold 434, Technic Inc.

    Current Density: 2.2 mA/cm$^2$

    Plating Rate: 16 – 18 $\mathring{A}$/s

    Thickness: 1.0 $\mu$m

13. **Metal 1: Cr E-beam Evaporation**

    Base Pressure: $< 10^{-6}$ Torr

    Beam Voltage: 5 kV

Deposition Rate: 3.0 $\mathring{A}$/s

Thickness: 30 nm

14. **Metal 1: Electroplating Mold Removal**

    Solution: AZ KWIK Strip Remover at 60 °C

    Time: 60 min

15. **Metal 1: Electroplating Seed Layer Etching**

    Au Etching:

    Etchant: Gold Etchant TFA, Transene Company Inc. at Room Temperature

    Etching Time: 20 – 25 s

    Cr Etching:

    Etchant: CRE-473 Chromium Etch, Transene Company Inc., at 40 °C

    Etching Time: 10 – 15 s

16. **Sacrificial Layer Coating**

    PI 2562 Coating

    Spin Speed: 1400 rpm

    Spin Duration: 1 min

    Bake 1: 2 min at 90 °C

    Bake 2: 2 min at 150 °C

    Cure: 30 min at 350 °C

    Thickness: 2.5 $\mu$m

17. **Anchor: Al Sputtering**

    Pressure: 3.5 mTorr

    Sputtering Gas: Ar

    Plasma Source: DC

    Power Density: 2.7 W/cm$^2$

Deposition Rate: 3 $\mathring{A}$/s

Thickness: 300 nm

18. **Anchor: Mask 4**

    AZ3330 Coating

    Process Conditions: similar to the previous AZ3330 patterning steps

19. **Anchor: Al etching**

    Etchant: PAN at 40 °C

    Etching Time: 80 – 100 s

20. **Anchor: PI RIE Etching**

    Pressure: 250 mTorr

    Gases and Flow Rates: $O_2$ 30 SCCM

    RIE Power Density: 0.10 W/cm$^2$

    ICP Power Density: 0.20 W/cm$^2$

    Time: 600 s

21. **Anchor: Al etching**

    Process Conditions: similar to the previous Al etching step

    Etching Time: 120 s

22. **Dimple: Mask 5**

    AZ3330 Coating

    Process Conditions: similar to the previous AZ3330 patterning steps

23. **Dimple: PI RIE Etching**

    Pressure: 250 mTorr

    Gases and Flow Rates: $O_2$ 30 SCCM

    RIE Power Density: 0.10 W/cm$^2$

ICP Power Density: 0.10 W/cm$^2$

Time: 240 s

24. **Dimple: Photoresist Removal**

    Solution: AZ KWIK Strip Remover at 60 °C

    Time: 30 min

25. **Metal 2: Electroplating Seed Layer Deposition**

    Pressure: 3.5 mTorr

    Sputtering Gas: Ar

    Plasma Source: DC

    Power Density: 1.6 W/cm$^2$

    Deposition Rate: 5 $\mathring{A}$/s

    Thickness: 100 nm

26. **Metal 2: Mold Patterning (Mask 6)**

    Process Conditions: similar to the metal 1 mold pattering step

27. **Metal 2: Au Electroplating**

    Process Conditions: similar to the metal 1 Au electroplating step

    Thickness: 1.0 $\mu$m

28. **Metal 2: Cr E-beam Evaporation**

    Process Conditions: similar to the metal 1 Cr E-beam evaporation step

    Thickness: 30 nm

29. **Metal 2: Electroplating Mold Removal**

    Process Conditions: similar to the electroplating mold removal step for metal 1

30. **Metal 2: Electroplating Seed Layer Etching**

    Process Conditions: similar to the electroplating seed layer etching for metal 1

31. **Annealing**

    360 – 400 °C for 3hrs

32. **Release: PI RIE Etching**

    Pressure: 10 mTorr

    Gases and Flow Rates: $O_2$ 20 SCCM

    ICP Power Density: 0.58 W/cm$^2$

    Time: 1 – 2 hrs

## A.4 Process Flow of the Magnetic-Actuated MEMS Switches

The processing conditions and the details of the fabrication steps illustrated in Fig. 5.17 for the construction of the developed magnetic-actuated MEMS switches are as follows:

1. **Substrate Cleaning**

   Cleaning Process: RCA 1

   Hot Wash: 15 min

2. **Metal 1: Electroplating Seed Layer Deposition**

   Cr E-beam Evaporation:

   Base Pressure: $< 10^{-6}$ Torr

   Beam Voltage: 5 kV

   Deposition Rate: 3.0 $\mathring{A}$/s

   Thickness: 30 nm

   Au E-beam Evaporation:

   Base Pressure: $< 10^{-6}$ Torr

Beam Voltage: 5 kV

Deposition Rate: 10 $\mathring{A}$/s

Thickness: 100 nm

3. **Metal 1: Mold Patterning (Mask 1)**

   AZ nLof 2035 Coating

   Spin Speed: 4000 rpm

   Spin Duration: 1 min

   Softbake: 1 min at 110 °C

   Exposure Time: 15 s (UV Intensity: 40 mW/cm$^2$)

   Post Exposure Bake: 1 min at 110 °C

   Development Time: 135 – 150 s

   Hardbake: 1 min at 110 °C

4. **Metal 1: Au Electroplating**

   Solution: Techni-Gold 434, Technic Inc.

   Current Density: 2.2 mA/cm$^2$

   Plating Rate: 16 – 18 $\mathring{A}$/s

   Thickness: 1.0 $\mu$m

5. **Metal 1: Cr E-beam Evaporation**

   Base Pressure: $< 10^{-6}$ Torr

   Beam Voltage: 5 kV

   Deposition Rate: 3.0 $\mathring{A}$/s

   Thickness: 30 nm

6. **Metal 1: Electroplating Mold Removal**

   Solution: AZ KWIK Strip Remover at 60 °C

   Time: 60 min

7. **Metal 1: Electroplating Seed Layer Etching**

   Au Etching:

   Etchant: Gold Etchant TFA, Transene Company Inc. at Room Temperature

   Etching Time: 20 – 25 s

   Cr Etching:

   Etchant: CRE-473 Chromium Etch, Transene Company Inc., at 40 °C

   Etching Time: 10 – 15 s

8. **Sacrificial Layer Coating**

   PI 2611 Coating

   Spin Speed: 3000 rpm

   Spin Duration: 1 min

   Bake 1: 2 min at 90 °C

   Bake 2: 2 min at 150 °C

   Cure: 30 min at 350 °C

   Thickness: 5 $\mu$m

9. **Anchor: Al Sputtering**

   Pressure: 3.5 mTorr

   Sputtering Gas: Ar

   Plasma Source: DC

   Power Density: 2.7 W/cm$^2$

   Deposition Rate: 3 $\mathring{A}$/s

   Thickness: 300 nm

10. **Anchor: Mask 2**

    AZ3330 Coating

    Spin Speed: 3000 rpm

    Spin Duration: 1 min

Softbake: 3 min at 90 °C

Exposure Time: 15 s (UV Intensity: 40 mW/cm$^2$)

Post Exposure Bake: 2 min at 90 °C

Development Time: 45 – 60 s

Hardbake: 2 min at 110 °C

11. **Anchor: Al etching**

    Etchant: PAN at 40 °C

    Etching Time: 80 – 100 s

12. **Anchor: PI RIE Etching**

    Pressure: 250 mTorr

    Gases and Flow Rates: $O_2$ 30 SCCM

    RIE Power Density: 0.10 W/cm$^2$

    ICP Power Density: 0.20 W/cm$^2$

    Time: 600 s

13. **Anchor: Al etching**

    Process Conditions: similar to the previous Al etching step

    Etching Time: 120 s

14. **Dielectric Cantilever: $SiN_x$ Deposition**

    Pressure: 625 mTorr

    Deposition Temperature: 350 °C

    Gases and Flow Rates: $SiH_4$ 12 SCCM, $N_2$ 200 SCCM, and $NH_3$ 10 SCCM

    Plasma Source: 10 kHz

    Power Density: 0.23 W/cm$^2$

    Deposition Rate: 3.3 $\mathring{A}$/s

    Thickness: 500 nm

15. **Dielectric Cantilever: Metal 2 Adhesion Layer**

    Cr E-beam Evaporation:

    Base Pressure: $< 10^{-6}$ Torr

    Beam Voltage: 5 kV

    Deposition Rate: 3.0 $\AA$/s

    Thickness: 30 nm

16. **Dielectric Cantilever: Mask 3**

    AZ3330 Coating

    Process Conditions: similar to the previous AZ3330 patterning step

17. **Dielectric Cantilever: Cr Etching**

    Process Conditions: similar to the electroplating seed layer etching for metal 1

18. **Dielectric Cantilever: $SiN_x$ Etching**

    Pressure: 250 mTorr

    Gases and Flow Rates: $CF_4$ 30 SCCM

    RIE Power Density: 0.20 W/cm$^2$

    ICP Power Density: 0.20 W/cm$^2$

    Etching Time: 160 – 200 s

19. **Photoresist Removal**

    Solution: AZ KWIK Strip Remover at 60 °C

    Time: 30 min

20. **Dimple: PI RIE Etching**

    Pressure: 250 mTorr

    Gases and Flow Rates: $CF_4$ 30 SCCM

    RIE Power Density: 0.10 W/cm$^2$

ICP Power Density: 0.10 W/cm$^2$

Etching Time: 240 – 260 s

21. **Metal 2: Electroplating Seed Layer Deposition**

    Pressure: 3.5 mTorr

    Sputtering Gas: Ar

    Plasma Source: DC

    Power Density: 1.6 W/cm$^2$

    Deposition Rate: 5.0 $\mathring{A}$/s

    Thickness: 100 nm

22. **Metal 2: Mold Patterning (Mask 4)**

    Process Conditions: similar to the metal 1 mold pattering step

23. **Metal 2: Au Electroplating**

    Process Conditions: similar to the metal 1 Au electroplating step

    Thickness: 1.0 $\mu$m

24. **Metal 2: Cr E-beam Evaporation**

    Process Conditions: similar to the metal 1 Cr E-beam evaporation step

    Thickness: 30 nm

25. **Metal 2: Electroplating Mold Removal**

    Process Conditions: similar to the electroplating mold removal step for metal 1

26. **Metal 2: Electroplating Seed Layer Etching**

    Process Conditions: similar to the electroplating seed layer etching for metal 1

27. **Annealing**

    360 - 400 °C for 3hrs

28. **Release: PI RIE Etching**

    Pressure: 10 mTorr

    Gases and Flow Rates: $O_2$ 20 SCCM

    ICP Power Density: 0.58 W/cm$^2$

    Time: 2 – 3 hrs

# References


[1] G. Ehrenstein and H. Lecar, "The mechanism of signal transmission in nerve axons," *Ann. Rev. Biophys. Bioeng.*, vol. 1, pp. 347–366, Jun. 1972.

[2] A. L. Hodgkin and A. F. Huxley, "A quantitative description of membrane current and its application to conduction and excitation in nerve," *J. Physiol.*, vol. 117, no. 4, pp. 500–544, Aug. 1952.

[3] G. P. Moore, J. P. Segundo, D. H. Perkel, and H. Levitan, "Statistical signs of synaptic interaction in neurons," *Biophys. J.*, vol. 10, no. 9, pp. 876–900, Sep. 1970.

[4] D. R. Humphrey, E. M. Schmidt, and W. D. Thompson, "Predicting measures of motor performance from multiple cortical spike trains," *Science*, vol. 170, no. 3959, pp. 758–762, Nov. 1970.

[5] A. P. Georgopoulos, A. B. Schwartz, and R. E. Ketiner, "Neuronal population coding of movement direction," *Science*, vol. 233, no. 4771, pp. 1416–1419, Sep. 1986.

[6] A. B. Schwartz, "Direct cortical representation of drawing," *Science*, vol. 265, no. 5171, pp. 540–542, Jul. 1994.

[7] K. D. Wise, D. J. Anderson, J. F. Hetke, D. R. Kipke, and K. Najafi, "Wireless implantable microsystems: high-density electronic interfaces to the nervous system," *Proc. of IEEE*, vol. 92, no. 1, pp. 76–97, Jan. 2004.

[8] F. A. Spelman, "The past, present, and future of cochlear prostheses," *IEEE Eng. Med. Biol. Mag.*, vol. 18, no. 2, pp. 27–33, May 1999.

[9] E. M. Schmidt, M. J. Bak, F. T. Hambrecht, C. V. Kufta, D. K. O'Rourke, and P.Vallabhanath, "Feasibility of a visual prosthesis for the blind based on intracortical microstimulation of the visual cortex," *Brain*, vol. 119, no. 2, pp. 507–522, Apr. 1996.

[10] E. Margalit, M. Maia, J. D. Weiland, R. J. Greenberg, G. Y. Fujii, G. Torres, D. V. Piyathaisere, T. M. O'Hearn, W. Liu, G. Lazzi, G. Dagnelie, D. A. Scribner, E. de

Juan Jr., and M. S. Humayun, "Retinal prosthesis for the blind," *Surv. Ophthalmol.*, vol. 47, no. 4, pp. 335–356, Jul. 2002.

[11] K. Ashkan, B. Wallace, B. A. Bell, and A. L. Benabid, "Deep brain stimulation of the subthalamic nucleus in Parkinson's disease 1993-2003: where are we 10 years on?" *Br. J. Neurosurg.*, vol. 18, no. 1, pp. 19–34, Feb. 2004.

[12] H. Toda, C. Hamani, and A. Lozano, "Deep brain stimulation in the treatment of dyskinesia and dystonia," *Neurosurg. Focus.*, vol. 17, no. 1, pp. 9–13, Jul. 2004.

[13] B. J. Nuttin, L. A. Gabriëls, P. R. Cosyns, B. A. Meyerson, S. Andréewitch, S. G. Sunaert, A. F. Maes, P. J. Dupont, J. M. Gybels, F. Gielen, and H. G. Demeulemeester, "Long-term electrical capsular stimulation in patients with obsessive-compulsive disorder," *Neurosurgery*, vol. 52, no. 6, pp. 1263–1274, Jun. 2003.

[14] E. B. Montgomery Jr., "Deep brain stimulation for hyperkinetic disorders," *Neurosurg. Focus.*, vol. 17, no. 1, pp. 1–8, Jul. 2004.

[15] H. S. Mayberg, A. M. Lozano, V. Voon, H. E. McNeely, D. Seminowicz, C. Hamani, J. M. Schwalb, and S. H. Kennedy, "Deep brain stimulation for treatment-resistant depression," *Neuron.*, vol. 45, no. 5, pp. 651–660, Mar. 2005.

[16] M. Mojarradi, D. Binkley, B. Blalock, R. Andersen, N. Ulshoefer, T. Johnson, and L. del Castillo, "A miniaturized neuroprosthesis suitable for implantation into the brain," *IEEE Trans. Neural Syst. and Rehab. Eng.*, vol. 11, no. 1, pp. 38–42, Mar. 2003.

[17] W. R. Patterson, Y. K. Song, C. W. Bull, I. Ozden, A. P. Deangellis, C. Lay, J. L. McKay, A. V. Nurmikko, J. D. Donoghue, and B. W. Connors, "A microelectrode-microelectronic hybrid device for brain implantable neuroprosthesis applications," *IEEE Trans. Biomed. Eng.*, vol. 51, no. 10, pp. 1845–1853, Oct. 2004.

[18] E. C. Leuthardt, G. Schalk, J. R. Wolpaw, J. G. Ojemann, and D. W. Moran, "A brain-computer interface using electrocorticographic signals in humans," *J. Neural Eng.*, vol. 1, no. 2, pp. 63–71, Jun. 2004.

[19] U. G. Hofmann, A. Folkers, F. Mösch, T. Malina, K. M. L. Menne, G. Biella, P. Fagerstedt, E. De Schutter, W. Jensen, K. Yoshida, D. Hoehl, U. Thomas, M. G. Kindlundh, P. Norlin, and M. de Curtis, "A novel high channel-count system for acute multisite neuronal recordings," *IEEE Trans. Biomed. Eng.*, vol. 53, no. 8, pp. 1672–1677, Aug. 2006.

[20] H. K. Trieu, L. Ewe, W. Mokwa, M. Schwarz, and B. J. Hosticka, "Flexible silicon structures for a retina implant," in *Proc. IEEE MEMS*, Jan. 1998, pp. 515–519.

[21] D. C. Rodger, A. J. Fong, W. Li, H. Ameri, A. K. Ahuja, C. Gutierrez, I. Lavrov, H. Zhong, P. R. Menon, E. Meng, J. W. Burdick, R. R. Roy, V. R. Edgerton, J. D. Weiland, M. S. Humayun, and Y.-C. Tai, "Flexible parylene-based multielectrode array technology for high-density neural stimulation and recording," *Sensor Actuat. B*, vol. 132, no. 2, pp. 449–460, Jun. 2008.

[22] H. Takahashi, T. Ejiri, M. Nakao, N. Nakamura, K. Kaga, and T. Hervé, "Microelectrode array on folding polyimide ribbon for epidural mapping of functional evoked potentials," *IEEE Trans Biomed. Eng.*, vol. 50, no. 4, pp. 510–516, Apr. 2003.

[23] R. M. Dowben and J. E. Rose, "A metal filled microelectrode," *Science*, vol. 118, no. 3053, pp. 22–24, Jul. 1953.

[24] H. A. Baldwin, S. Frank, and J. Y. Lettvin, "Glasscoated tungsten microelectrodes," *Science*, vol. 148, no. 3676, pp. 1462–1463, Jun. 1965.

[25] D. A. Robinson, "The electrical properties of metal microelectrodes," *Proc. of IEEE*, vol. 56, no. 6, pp. 1065–1071, Jun. 1968.

[26] O. F. Schanne, M. Lavallée, R. Laprade, and S. Gagné, "Electrical properties of glass microelectrodes," *Proc. of IEEE*, vol. 56, no. 6, pp. 1072–1082, Jun. 1968.

[27] D. McCreery, A. Lossinsky, V. Pikov, and X. Liu, "Microelectrode array for chronic deep-brain microstimulation and recording," *IEEE Trans. Biomedical Eng.*, vol. 53, no. 4, pp. 726–737, Apr. 2006.

[28] J. Gimsa, B. Habel, U. Schreiber, U. Rienen, U. Strauss, and U. Gimsa, "Choosing electrodes for deep brain stimulation experimentselectrochemical considerations," *J. Neurosci. Meth.*, vol. 142, no. 2, pp. 251–265, Mar. 2005.

[29] G. E. Loeb, R. A. Peck, , and J. Martyniuk, "Toward the ultimate metal microelectrode," *J. Neurosci. Meth.*, vol. 63, no. 1–2, pp. 175–183, Dec. 1995.

[30] C. Xu, W. Lemon, and C. Liu, "Design and fabrication of a high-density metal microelectrode array for neural recording," *Sens. Actuators A*, vol. 96, no. 1, pp. 78–85, Jan. 2002.

[31] O. J. Prohaska, F. Olcaytug, P. Pfundner, and H. Dragaun, "Thin-film multiple electrode probes: possibilities and limitations," *IEEE Trans. Biomed. Eng.*, vol. BME-33, no. 2, pp. 223–229, Feb. 1986.

[32] C. M. Gray, P. Maldonado, M. Wilson, and B. McNaughton, "Tetrodes markedly improve the reliability and yield of multiple single-unit isolation from multiunit recordings in cat striate cortex," *J. Neurosci. Meth.*, vol. 63, no. 1–2, pp. 43–54, Dec. 1995.

[33] P. S. Motta and J. W. Judy, "Multielectrode microprobes for deep-brain stimulation fabricated with a customizable 3-D electroplating process," *IEEE Trans. Biomed. Eng.*, vol. 52, no. 5, pp. 923–933, May 2005.

[34] P. J. Rousche, D. S. Pellinen, D. P. Pivin Jr., J. C. Williams, R. J. Vetter, and D. R. Kipke, "Flexible polyimide-based intracortical electrode arrays with bioactive capability," *IEEE Trans. Biomed. Eng.*, vol. 48, no. 3, pp. 361–371, Mar. 2001.

[35] D. R. Kipke, D. S. Pellinen, and R. J. Vetter, "Advanced neural implants using thinfilm polymers," in *Proc. IEEE Int. Symp. Circuits Systems*, vol. 4, May 2002, pp. 173–176.

[36] G. Ensell, D. J. Banks, D. J. Ewins, W. Balachandran, and P. R. Richards, "Siliconbased microelectrodes for neurophysiology fabricated using a gold metallization/nitride passivation system," *J. Microelectromech. Syst.*, vol. 5, no. 2, pp. 117–121, Jun. 1996.

[37] D. J. Anderson, K. Najafi, S. J. Tanghe, D. A. Evans, K. L. Levy, J. F. Hetke, X. Xue, J. J. Zappia, and K. D. Wise, "Batch fabricated thin film electrodes for stimulation of the central auditory system," *IEEE Trans. Biomed. Eng.*, vol. 36, no. 7, pp. 693–705, Jul. 1989.

[38] G. T. A. Kovacs, C. W. Storment, and J. M. Rosen, "Regeneration microelectrode array for peripheral nerve recording and stimulation," *IEEE Trans. Biomed. Eng.*, vol. 39, no. 9, pp. 893–902, Sep. 1992.

[39] S. J. Tanghe and K. D. Wise, "A 16 channel CMOS neural stimulating array," *IEEE J. Solid-State Circuits*, vol. 27, no. 12, pp. 1819–1825, Dec. 1992.

[40] K. Changhyun and K. D. Wise, "64-site multishank CMOS low-profile neural stimulating probe," *IEEE J. Solid-State Circuits*, vol. 31, no. 9, pp. 1230–1238, Sep. 1996.

[41] M. Kuperstein and D. A. Whittington, "A practical 24-channel microelectrode for neural recording in-vivo," *IEEE Trans. Biomed. Eng.*, vol. BME-28, no. 3, pp. 288–293, Mar. 1981.

[42] A. B. Frazier, D. P. OBrien, and M. G. Allen, "Two dimensional metallic microelectrode arrays for extracellular stimulation and recording of neurons," in *Proc. IEEE MEMS*, Feb. 1993, pp. 195–200.

[43] N. A. Blum, B. G. Carkhuff, H. K. Charles, R. L. Edwards, and R. A. Meyer, "Multisite microprobes for neural recordings," *IEEE Trans. Biomed. Eng.*, vol. 38, no. 1, pp. 68–74, Jan. 1991.

[44] R. Dean, J. Weller, M. Bozack, B. Farrell, L. Jauniskis, J. Ting, D. Edell, and J. Hetke, "Novel biomedical implant interconnects utilizing micromachined LCP," in *Proc. SPIE*, vol. 5515, Aug. 2004, pp. 88–99.

[45] D. Papageorgiou, S. C. Bledsoe, M. Gulari, J. F. Hetke, D. J. Anderson, and K. D. Wise, "A shuttered probe with in-line flowmeters for chronic in-vivo drug delivery," in *Proc. IEEE MEMS*, 2001 Jan, pp. 212–215.

[46] J. K. Chen, K. D. Wise, J. F. Hetke, and S. C. Bledsoe Jr., "A multichannel neural probe for selective chemical delivery at the cellular level," *IEEE Trans. Biomed. Eng.*, vol. 44, no. 8, pp. 760–769, Aug. 1997.

[47] D. J. Edell, V. V. Toi, V. M. McNeil, and L. D. Clark, "Factors influencing the biocompatibility of insertable silicon microshafts in cerebral cortex," *IEEE Trans. Biomed. Eng.*, vol. 39, no. 6, pp. 635–643, Jun. 1992.

[48] Y. Yao, M. N. Gulari, B. Casey, J. A. Wiler, and K. D. Wise, "Silicon microelectrodes with flexible integrated cables for neural implant applications," in *Proc. IEEE EMBS Conf. Neural Eng.*, May 2007, pp. 398–401.

[49] S. Kisban, S. Herwik, K. Seidl, B. Rubehn, A. Jezzini, M. A. Umiltà, L. Fogassi, T. Stieglitz, O. Paul, and P. Ruther, "Microprobe array with low impedance electrodes and highly flexible polyimide cables for acute neural recording," in *Proc. Int. IEEE EMBS Conf.*, Aug. 2007, pp. 175–178.

[50] http://manuals.medtronic.com/en/neuromodulation/neurological-leads/index.htm.

[51] U. G. Hofmann, C. K. E. Moll, G. Engler, A. K. Engel, M. Bär, D. Höhl, U. Thomas, and P. Detemple, "Multisite microelectrodes for use in human deep brain stimulation," in *Proc. Int. Conf. Microtechnol. Med. Biol.*, May 2006, pp. 284–287.

[52] T. Gritsun, S. Vogt, G. Engler, C. K. E. Moll, A. K. Engel, S. Kondra, L. Ramrath, and U. G. Hofmann, "A simple microelectrode bundle for deep brain recordings," in *Proc. 3rd Int. IEEE EMBS Conf. Neural Eng.*, May 2007, pp. 114–117.

[53] G. M. Rebeiz and J. B. Muldavin, "RF MEMS switches and switch circuits," *IEEE Microwave Magazine*, vol. 2, no. 4, pp. 59–71, Dec. 2001.

[54] M. P. Lepselter, "Beam-lead technology," *Bell Syst. Tech. J.*, vol. 45, no. 2, pp. 233–254, Feb. 1966.

[55] K. D. Wise, J. B. Angell, and A. Starr, "An integrated circuit approach to extracellular microelectrodes," *IEEE Trans. Biomed. Eng.*, vol. BME-17, no. 7, pp. 238–247, Jul. 1970.

[56] K. D. Wise and J. B. Angell, "A low-capacitance multielectrode probe for use in extracellular neurophysiology," *IEEE Trans. Biomed. Eng.*, vol. BME-22, no. 5, pp. 212–219, May 1975.

[57] G. A. May, S. A. Shamma, and R. L. White, "A tantalum-on-sapphire microelectrode array," *IEEE Trans. Electron. Devices*, vol. ED-26, no. 12, pp. 1932–1939, Dec. 1979.

[58] A. Altuna, G. Gabriel, L. M. de la Prida, M. Tijero, A. Guimerá, J. Berganzo, R. Salido, R. Villa, and L. J. Fernández, "SU-8-based microneedles for in vitro neural applications," *J. Micromech. Microeng.*, vol. 20, no. 6, pp. 64 014 1–6, Jun. 2010.

[59] H.-Y. Chan, D. M. Aslam, J. A. Wiler, and B. Casey, "A novel diamond microprobe for neuro-chemical and -electrical recording in neural prosthesis," *J. Microelectromech. Sys.*, vol. 18, no. 3, pp. 511–521, Jun. 2009.

[60] J. D. Weiland and D. J. Anderson, "Chronic neural stimulation with thin-film, iridium oxide electrodes," *IEEE Trans. Biomed. Eng.*, vol. 47, no. 7, pp. 911–918, Jul. 2000.

[61] B. Ziaie, J. von Arx, and K. Najafi, "A micro-fabricated planar high-current $IrO_x$ stimulating microelectrode," in *Proc. IEEE EMBS*, Nov. 1996, pp. 270–271.

[62] W. L. C. Rutten, H. J. van Wier, and J. H. M. Put, "Sensitivity and selectivity of intraneural stimulation using a silicon electrode array," *IEEE Trans. Biomed. Eng.*, vol. 38, no. 2, pp. 192–198, Feb. 1991.

[63] X. Beebe and T. L. Rose, "Charge injection limits of activated iridium oxide electrode with 0.2 ms pulses in bicarbonate buffered saline," *IEEE Trans. Biomed. Eng.*, vol. 35, no. 6, pp. 494–496, Jun. 1988.

[64] J. Chen, K. D. Wise, J. F. Hetke, and S. C. Bledsoe, "A multichannel neural probe for selective chemical delivery at the cellular level," *IEEE Tran. Biomed. Eng.*, vol. 44, no. 8, pp. 760–769, Aug. 1997.

[65] B. Fischl and A. M. Dale, "Measuring the thickness of the human cerebral cortex from magnetic resonance images," *Proc. Nat. Academy Sciences USA*, vol. 97, no. 20, pp. 11 050–11 055, Sep. 2000.

[66] A. Bohg, "Ethylene diamine-pyrocatechol-water mixture shows etching anomaly in boron-doped silicon," *J . Electrocbem. Soc.*, vol. 118, no. 2, pp. 401–402, Feb. 1971.

[67] H. Seidel, L. Csepregi, A. Heuberger, and H. Baumgärtel, "Anisotropic etching of crystalline silicon in alkaline solutions," *J. Electrochem. Soc.*, vol. 137, no. 11, pp. 3626–3632, Nov. 1990.

[68] C. Huang and K. Najafi, "Fabrication of ultrathin $p^{++}$ silicon microstructures using ion implantation and boron etch-stop," *J. Microelectromech. Systems*, vol. 10, no. 4, pp. 532–537, Dec. 2001.

[69] Q. Bai, K. D. Wise, and D. J. Anderson, "A high-yield microassembly structure for three-dimensional microelectrode arrays," *IEEE Trans. Biomed. Eng.*, vol. 47, no. 3, pp. 281–289, Mar. 2000.

[70] J. F. Hetke, J. L. Lund, K. Najafi, K. D. Wise, and D. J. Anderson, "Silicon ribbon cables for chronically implantable microelectrode arrays," *IEEE Trans. Biomed. Eng.*, vol. 41, no. 4, pp. 314–321, Apr. 1994.

[71] P. Norlin, M. Kindlundh, A. Mouroux, K. Yoshida, and U. G. Hofmann, "A 32-site neural recording probe fabricated by DRIE of SOI substrates," *J. Micromech. Microeng.*, vol. 12, no. 4, pp. 414–419, Jul. 2002.

[72] K. C. Cheung, K. Djupsund, Y. Dan, and L. P. Lee, "Implantable multichannel electrode array based on SOI technology," *J. Microelectromech. Sys.*, vol. 12, no. 2, pp. 179–184, Apr. 2003.

[73] K. C. Cheung, L. Gun, K. Djupsund, D. Yang, and L. P. Lee, "A new neural probe using SOI wafers with topological interlocking mechanisms," in *Proc. IEEE EMBS Conf. Microtechnologies Medicine Biology*, Oct. 2000, pp. 507–511.

[74] S. Herwik, S. Kisban, A. A. A. Aarts, K. Seidl, G. Girardeau, K. Benchenane, M. B. Zugaro, S. I. Wiener, O. Paul, H. P. Neves, and P. Ruther, "Fabrication technology for silicon-based microprobe arrays used in acute and sub-chronic neural recording," *J. Micromech. Microeng.*, vol. 19, no. 7, pp. 74 008 1–11, Jul. 2009.

[75] K. Seidl, S. Spieth, S. Herwik, J. Steigert, R. Zengerle, O. Paul, and P. Ruther, "In-plane silicon probes for simultaneous neural recording and drug delivery," *J. Micromech. Microeng.*, vol. 20, no. 10, pp. 105 006 1–11, Oct. 2010.

[76] P. K. Campbell, K. E. Jones, R. J. Huber, K. W. Horch, and R. A. Normann, "A silicon-based, three-dimensional neural interface: manufacturing processes for an intracortical electrode array," *IEEE Trans. Biomed. Eng.*, vol. 38, no. 8, pp. 758–768, Aug. 1991.

[77] K. E. Jones, P. K. Campbell, and R. A. Normann, "A glass/silicon composite intracortical electrode array," *Ann. Biomed. Eng.*, vol. 20, no. 4, pp. 423–437, Jul. 1992.

[78] P. J. Rousche and R. A. Normann, "Chronic recording capability of the utah intracortical electrode array in cat sensory cortex," *J. Neurosci. Methods*, vol. 82, no. 1, pp. 1–15, Jul. 1998.

[79] J. C. Williams, R. L. Rennaker, and D. R. Kipke, "Long-term neural recording characteristics of wire microelectrode arrays implanted in cerebral cortex," *Brain Res. Protoc.*, vol. 4, no. 3, pp. 303–313, Dec. 1999.

[80] M. A. Nicolelis, A. A. Ghazanfar, B. M. Faggin, S. Votaw, and L. M. Oliveira, "Reconstructing the engram: simultaneous, multisite, many single neuron recordings," *Neuron*, vol. 18, no. 4, pp. 529–537, Apr. 1997.

[81] K. C. Cheung, P. Renaud, H. Tanila, and K. Djupsund, "Flexible polyimide microelectrode array for in vivo recordings and current source density analysis," *Biosens. Bioelectron.*, vol. 22, no. 8, pp. 1783–1790, Mar. 2007.

[82] J. C. Williams, M. M. Holecko II, S. P. Massia, P. Rousche, and D. R. Kipke, "Multisite incorporation of bioactive matrices into MEMS-based neural probes," *J. Neural Eng.*, vol. 2, no. 4, pp. L23–L28, Dec. 2005.

[83] S. Takeuchi, T. Suzuki, K. Mabuchi, and H. Fujita, "3D flexible multichannel neural probe array," *J. Micromech. Microeng.*, vol. 14, no. 1, pp. 104–107, Jan 2004.

[84] G. T. A. Kovacs, "Addressable biologic electrode array," U.S. Patent 6 682 936 B2, 2007.

[85] S. A. Nikles, D. S. Pellinen, J. Kitagawa, R. M. Bradley, D. R. Kipke, and K. Najafi, "Long term in vitro monitoring of polyimide microprobe electrical properties," in *Proc. IEEE EMBC*, Sep. 2003, pp. 3340–3343.

[86] K.-K. Lee, J. He, A. Singh, S. Massia, G. Ehteshami, B. Kim, and G. Raupp, "Polyimide-based intracortical neural implant with improved structural stiffness," *J. Micromech. Microeng.*, vol. 14, no. 1, pp. 32–37, Jan. 2004.

[87] S. S. Gill, "Brain electrode," U.S. Patent 0 015 130 A1, 2005.

[88] A. Maciossek, "Electrodeposition of 3-D microstructures without moulds," in *Proc. SPIE*, vol. 2879, Oct. 1996, pp. 275–279.

[89] L. Robblee, J. . Letko, and S. Bruininer, "Activated iridium: an electrode suitable for reversible charge injection into saline solutions," *J. Electrochem. Soc.*, vol. 130, no. 3, pp. 730–733, Mar. 1983.

[90] S. Gottesfeld and J. McIntyre, "Electrochromism in anodic iridium oxide films," *J. Electrochem. Soc.*, vol. 126, no. 5, pp. 742–750, May 1979.

[91] A. A. Fomani and R. R. Mansour, "Flexible neural microelectrode arrays reinforced with embedded metallic micro-needles," in *Proc. IEEE Sensors Conf.*, Nov. 2010, pp. 1601–1604.

[92] ——, "Fabrication and characterization of flexible neural microprobes with improved structural design," *Sensor Actuat. A*, in press 2011.

[93] W. C. Young, R. G. Budynas, and R. J. Roark, *Roark's formulas for stress and strain*, 7th ed. New York: McGraw-Hill, 2002, p. 723.

[94] J. A. Helsen and H. J. Breme, *Metals as Biomaterials*. New York: Wiley, 1984.

[95] C. W. Baek, Y. K. Kim, Y. Ahn, and Y. H. Kim, "Measurement of the mechanical properties of electroplated gold thin films using micromachined beam structures," *Sens. Actuators A Phys.*, vol. 117, no. 1, pp. 17–27, Jan. 2005.

[96] http://hdmicrosystems.com.

[97] K. Stokes, "Implantable pacing lead technology," *IEEE Trans. Biomed. Eng. Mag.*, vol. 9, no. 2, pp. 43–49, Jun. 1990.

[98] A. A. Fomani and R. R. Mansour, "Monolithically integrated multiport RF MEMS switch matrices," *IEEE Trans. Microw. Theory and Tech.*, vol. 57, no. 12, pp. 3434–3441, Dec. 2009.

[99] A. A. Sharp, A. M. Ortega, D. Restrepo, D. Curran-Everett, and K. Gall, "In vivo penetration mechanics and mechanical properties of mouse brain tissue at micrometer scales," *IEEE Trans. Biomed. Eng.*, vol. 56, no. 1, pp. 45–53, Jan. 2009.

[100] S. Snow, S. C. Jacobsen, D. L. Wells, and K. W. Horch, "Microfabricated cylindrical multielectrodes for neural stimulation," *IEEE Trans. Biomed. Eng.*, vol. 53, no. 2, pp. 320–326, Feb. 2006.

[101] X. Beebe and T. L. Rose, "Charge injection limits of activated iridium oxide electrodes with 0.2 ms pulses in bicarbonate buffered saline," *IEEE Trans. Biomed. Eng.*, vol. 35, no. 6, pp. 494–495, Jun. 1988.

[102] M. Derchansky, E. Shahar, R. A. Wennberg, M. Samoilova, S. S. Jahromi, P. A. Abdemalik, L. Zhang, and P. L. Carlen, "Model of frequent, recurrent and spontaneous seizures in the intact mouse hippocampus," *Hippocampus*, vol. 14, no. 8, pp. 935–947, Apr. 2004.

[103] I. S. Cooper, I. Amin, M. Riklan, J. M. Waltz, and T. P. Poon, "Chronic cerebellar stimulation in epilepsy. Clinical and anatomical studies." *Arch Neurol.*, vol. 33, no. 8, pp. 559–570, Aug. 1976.

[104] T. Loddenkemper, A. Pan, S. Neme, K. B. Baker, A. R. Rezai, D. S. Dinner, E. B. J. Montgomery, and H. O. Lüders, "Deep brain stimulation in epilepsy," *J. Clin. Neurophysiol.*, vol. 18, no. 6, pp. 514–532, Nov. 2001.

[105] O. Rascol, P. Payoux, F. Ory, J. J. Ferreira, C. Brefel-Courbon, and J. L. Montastruc, "Limitations of current Parkinson's disease therapy," *Ann. Neurol.*, vol. 53, no. S3, pp. S3–S15, Jan. 2003.

[106] J. Volkmann, "Deep brain stimulation for the treatment of Parkinson's disease," *J. Clin. Neurophysiol.*, vol. 21, no. 1, pp. 6–17, Feb. 2004.

[107] E. Moro, R. J. Esselink, J. Xie, M. Hommel, A. L. Benabid, and P. Pollak, "The impact on Parkinson's disease of electrical parameter settings in STN stimulation," *Neurology*, vol. 59, no. 5, pp. 706–713, Sep. 2002.

[108] C. C. McIntyre, M. Savasta, B. L. Walter, and J. L. Vitek, "How does deep brain stimulation work? Present understanding and future questions," *J. Clin. Neurophysiol.*, vol. 21, no. 1, pp. 40–50, Feb. 2004.

[109] C. C. McIntyre, W. M. Grill, D. L. Sherman, and N. V. Thakor, "Cellular effects of deep brain stimulation: model-based analysis of activation and inhibition," *J. Neurophysiol.*, vol. 91, no. 4, pp. 1457–1469, Apr. 2004.

[110] A. A. Fomani, M. Moradi, S. Assaf, and R. R. Mansour, "3D microprobes for deep brain stimulation and recording," in *Proc. IEEE EMBC*, Sep. 2010, pp. 1808–1811 **(North America representative in student paper competition, Geographical Finalist award)**.

[111] A. A. Fomani, R. R. Mansour, C. Florez-Quenguan, and P. L. Carlen, "Development and characterization of multisite 3D microprobes for deep brain stimulation and recording," *Submitted to J. Microelectromech. Syst.*, 2011.

[112] F. H. Reid, "Electrodeposition of the platinum group metals," *Metallurgical Rev.*, vol. 8, no. 45, pp. 167–211, 1963.

[113] M. Kogoma and G. Turban, "Mechanism of etching and of surface modification of polyimide in RF and LF $SF_6$–$O_2$ discharges," *Plasma Chem. Plasma P.*, vol. 6, no. 4, pp. 349–380, Dec. 1986.

[114] N. Hájos, T. J. Ellender, R. Zemankovics, E. O. Mann, R. Exley, S. J. Cragg, T. F. Freund, and O. Paulsen, "Maintaining network activity in submerged hippocampal slices: importance in oxygen supply," *Eur. J. Neurosci.*, vol. 29, no. 2, pp. 319–327, Jan. 2009.

[115] B. Smith, P. H. Peckham, M. W. Keith, and D. D. Roscoe, "An externally powered, multichannel, implantable stimulator for versatile control of paralyzed muscle," *IEEE Trans. Biomed. Eng.*, vol. BME–34, no. 7, pp. 499–508, Jul. 1987.

[116] H. McDermott, "An advanced multiple channel cochlear implant," *IEEE Trans. Biomed. Eng.*, vol. 36, no. 7, pp. 789–797, Jul. 1989.

[117] R. H. Olsson III, M. N. Gulari, and K. D. Wise, "Silicon neural recording arrays with on-chip electronics for in-vivo data acquisition," in *Proc. IEEE EMBC*, Aug. 2002, pp. 237–240.

[118] Y. Yao, M. N. Gulari, J. F. Hetke, and K. D. Wise, "A self-testing multiplexed CMOS stimulating probe for a 1024-site neural prosthesis," in *Proc. IEEE Transducers'03*, Aug. 2003, pp. 1213–1216.

[119] D. Hah, E. Yoon, and S. Hong, "A low-voltage actuated micromachined microwave switch using torsion springs and leverage," *IEEE Trans. Microw. Theory Tech.*, vol. 48, no. 12, pp. 2540–2545, Dec. 2000.

[120] V. Milanović, M. Maharbiz, and K. S. Pister, "Batch transfer integration of RF microrelays," *IEEE Microw. Guided Wave Lett.*, vol. 10, no. 8, pp. 313–315, Aug. 2000.

[121] Z. Li, D. Zhang, T. Li, W.Wang, and G.Wu, "Bulk micromachined relay with lateral contact," *J. Micromech. Microeng.*, vol. 10, no. 3, pp. 329–333, Sep. 2000.

[122] R. E. Mihailovich, M. Kim, J. B. Hacker, E. A. Sovero, J. Studer, J. A. Higgins, and J. F. de Natale, "MEM relay for reconfigurable RF circuits," *IEEE Microw. Wireless Compon. Lett.*, vol. 11, no. 2, pp. 53–55, Feb. 2001.

[123] S. Duffy, C. Bozler, S. Rabe, J. Knecht, L. Travis, P.Wyatt, C. Keast, and M. Gouker, "MEMS microswitches for reconfigurable microwave circuitry," *IEEE Microw. Wireless Compon. Lett.*, vol. 11, no. 3, pp. 106–108, Mar. 2001.

[124] L. Que, J. S. Park, and Y. B. Gianchandani, "Bent-beam electrothermal actuators-part I: single beam and cascaded devices," *J. Microelectromech. Syst.*, vol. 10, no. 2, pp. 247–254, Jun. 2001.

[125] J. H. Comtois, M. A. Michalicek, , and C. C. Barron, "Electrothermal actuators fabricated in four-level planarized surface micromachined polycrystalline silicon," *Sensors and Actuat. A*, vol. 70, no. 1, pp. 23–31, Oct. 1998.

[126] M. Daneshmand, W. Yan, and R. R. Mansour, "Thermally actuated multiport RF MEMS switches and their performance in a vacuumed environment," *IEEE Trans. Microw. Theory Tech.*, vol. 55, no. 6, pp. 1229–1236, Jun. 2007.

[127] Y. Wang, Z. Li, D. T. McCormick, and N. C. Tien, "Low-voltage lateral MEMS switch with high RF performance," *J. Microelectromech. Syst.*, vol. 13, no. 6, pp. 902–911, Dec. 2004.

[128] I. J. Cho, T. Song, S. H. Baek, and E. Yoon, "A low-voltage and low-power RF MEMS series and shunt switches actuated by combination of electromagnetic and electrostatic forces," *IEEE Trans. Microw. Theory Tech.*, vol. 53, no. 7, pp. 2450–2457, Jul. 2005.

[129] W. P. Taylor, O. Brand, and M. G. Allen, "Fully integrated magnetically actuated micromachined relays," *J. Microelectromech. Syst.*, vol. 7, no. 2, pp. 181–191, Jun. 1998.

[130] M. Ruan, J. Shen, and C. B. Wheeler, "Latching micromagnetic relays," *J. Microelectromech. Syst.*, vol. 10, no. 4, pp. 511–517, Dec. 2001.

[131] E. R. Brown, "RF-MEMS switches for reconfigurable integrated circuits," *IEEE Trans. Microw. Theory Tech.*, vol. 46, no. 11, pp. 1868–1880, Nov. 1998.

[132] G. M. Rebeiz, "RF MEMS switches: status of the technology," in *IEEE Transducers'03*, Jun. 2003, pp. 1726–1729.

[133] B. Yassini, S. Choi, A. Zybura, M. Yu, R. E. Mihailovich, and J. F. DeNatale, "A novel MEMS LTCC switch matrix," in *Proc. IEEE Int. Microw. Symp.*, Jun. 2004, pp. 721–724.

[134] M. Daneshmand and R. R. Mansour, "Monolithic RF MEMS switch matrix integration," in *Proc. IEEE Int. Microw. Symp.*, Jun. 2006, pp. 140–143.

[135] A. A. Fomani and R. R. Mansour, "Miniature RF MEMS switch matrices," in *Proc. IEEE Int. Microw. Symp.*, Jun. 2009, pp. 1221–1224 **(Student Paper Competition finalist, Honourable Mention Award)**.

[136] W. E. Spear, G. Willeke, and P. G. Le Comber, "Electronic properties of microcrystalline silicon prepared in the glow discharge plasma," *Physica B + C*, vol. 117–118, no. 3, pp. 908–913, Mar. 1983.

[137] S. C. Saha, A. K. Barus, and S. Ray, "The role of hydrogen dilution and radio frequency power in the formation of microcrystallinity of n-type si:h thin film," *J. Appl. Phys.*, vol. 74, no. 9, pp. 5561–5568, Nov. 1993.

[138] A. A. Fomani, S. Fouladi, and R. R. Mansour, "Magnetically-actuated dielectric cantilever RF MEMS switches," in *Proc. IEEE Int. Microw. Symp.*, May 2010, pp. 269–299.